Benchmarking a New Three-Dimensional Ultrasound System for Prostate Image Guided Radiation Therapy

by

Holly A. Johnston

BSc, University of British Columbia, 2005

A Thesis Submitted in Partial Fulfillment of the
Requirements for the Degree of

MASTER OF SCIENCE

in the Department of Physics and Astronomy

University of Victoria

Benchmarking a New Three-Dimensional Ultrasound System for Prostate Image Guided Radiation Therapy

by

Holly A. Johnston

BSc, University of British Columbia, 2005

Supervisory Committee

Dr. M. Hilts, Co-supervisor (Department of Physics and Astronomy,

BC Cancer Agency - Vancouver Island Centre)

Dr. A. Jirasek, Co-supervisor (Department of Physics and Astronomy)

Dr. W. Beckham, Member (Department of Physics and Astronomy,

BC Cancer Agency - Vancouver Island Centre)

Dr. D. Karlen, Member (Department of Physics and Astronomy)

Supervisory Committee

Dr. M. Hilts, Co-supervisor (Department of Physics and Astronomy, BC Cancer Agency - Vancouver Island Centre)

Dr. A. Jirasek, Co-supervisor (Department of Physics and Astronomy)

Dr. W. Beckham, Member (Department of Physics and Astronomy, BC Cancer Agency - Vancouver Island Centre)

Dr. D. Karlen, Member (Department of Physics and Astronomy)

Abstract

Image guided radiation therapy (IGRT) is a new type of radiotherapy used to deliver lethal doses of radiation to mobile tumors, while preventing surrounding healthy structures from receiving high doses of radiation. It relies on image guidance to track the tumor and ensure its prescribed position in the radiation beam. The main goal of this work was to determine if a new three-dimensional ultrasound (3D US) image guidance device, called the Restitu System, could safely replace (or be used interchangeably with) an existing method involving x-ray images of implanted fiducial markers (FMs) for prostate IGRT. Using comparison statistics called 95 % limits of agreement (LOA), it was found that the new 3D US system did not produce measurements that agreed sufficiently closely to those made using the FM technique, and therefore, could not safely replace FMs for prostate IGRT. Ultrasound image quality and user variability were determined to have a significant impact on the agreement between the two methods. It was further shown that using the Restitu System offered no significant clinical advantages over a conventional patient re-positioning technique.

Table of Contents

List of Tables

List of Figures

Chapter 1

Introduction

It is estimated that 22 300 new cases of prostate cancer were diagnosed in Canada in 2007 alone, making it the most common cancer site for Canadian men [5]. Prostate cancer is diagnosed using a series of tests, beginning with a digital rectal examination [6]. During this procedure, a trained physician inserts a gloved finger into the rectum and examines the surface of the prostate through the rectal wall. If abnormalities exist in the size, symmetry, or texture of the gland [7], prostate cancer is suspected, and a prostate specific antigen (PSA) test is performed. This test measures the amount of PSA in the body by extracting a blood sample. High levels of PSA indicate an enlarged prostate gland, which may be due to prostate cancer or other prostate problems [7]. If high PSA levels are detected, a transrectal ultrasound (TRUS) guided prostate biopsy is performed to confirm whether or not prostate cancer is present [6]. During this exam, a TRUS probe is inserted into the rectum, and ultrasound images of the prostate are used to guide a biopsy needle through the rectum or perineum into the prostate gland. Cells are removed from various locations of the gland and examined using a microscope to determine if they are cancerous [6, 7].

Following a positive diagnosis, the stage and grade of prostate cancer are assessed. There are four stages of prostate cancer, each differentiated by the size of the tumor and how far the cancer has spread from the prostate into the body. As stage number

increases from 1 to 4, the size of the tumor increases. Stages 1 and 2 indicate the tumor is confined to within the prostate gland, while stages 3 and 4 indicate the disease has extended into surrounding structures. Prostate cancer grade is a measure of how aggressively the tumor grows, and is commonly reported as a Gleason score between 2 and 10. A low Gleason score indicates slow growth while a high Gleason score indicates rapid growth. Prostate cancer stage and grade, as well as patient PSA level, must be known before a treatment modality can be chosen [6].

Several treatment options exist for prostate cancer patients. These include *watchful waiting*, continual monitoring of cancer stage and grade for patients with slow growing tumors and no symptoms, *radical prostatectomy*, a surgical procedure that completely removes the prostate gland from the body, *hormonal therapy*, adminstration of hormonal drugs or removal of the testicles to stop growth and shrink the tumor, *chemotherapy*, administration of drugs to kill cancer cells, *brachytherapy*, insertion of radioactive seeds into the prostate gland that irradiate and destroy cancer cells, and *external beam radiation therapy*, irradiation of cancer cells from outside the body using a linear accelerator [6]. The most common active treatment method for prostate cancer is radical prostatectomy, while external beam radiation therapy and brachytherapy are the second and third most popular treatments respectively [8].

This work focuses on external beam radiation therapy for prostate cancer. Using this technique, a treatment plan is formulated for each patient based on computed tomography (CT) images of the pelvic area. The plan is designed to provide a prescribed radiation dose to the disease while sparing surrounding normal tissues. However, the objectives of treatment are complicated by displacement of the prostate gland between time of treatment planning and treatment delivery.

Figure 1.1 shows a mid-sagittal (side) view of the male pelvic anatomy. Because the prostate is sandwiched between the bladder and rectum, regular filling and voiding of these structures causes three-dimensional (3D) motion of the gland [9–11]. Since

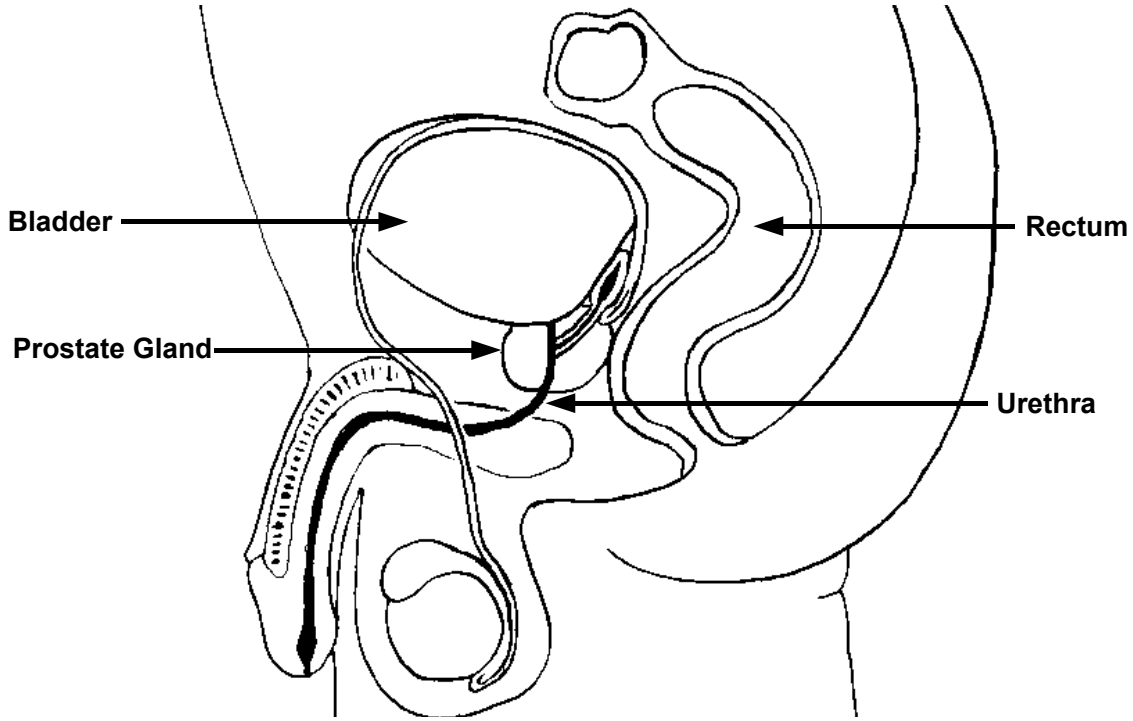

Figure 1.1: Mid-sagittal (side) view of the male pelvic anatomy showing the close proximity of the prostate gland to the bladder and rectum.

CT images used in treatment planning show only a "snapshot" of prostate position, the treatment plan does not incorporate this motion. If displacement of the prostate is not accounted for, the treatment may be ineffective at destroying the disease, and may also injure surrounding critical structures.

This has led to treatment of prostate cancer by a new type of radiation therapy, called image guided radiation therapy (IGRT). Image guided radiation therapy aims to pin point the position of the radiation target on each day of treatment, and realign it into the radiation beam using image guidance.

A common image guidance technique for prostate IGRT is to quantify prostate displacements through the use of x-ray opaque fiducial markers (FMs) inserted into the prostate gland. This method is commonly called FM prostate localization. X-ray images of the prostate and FMs are obtained at time of planning and just prior to each radiation treatment. The images are compared, and any displacement in

prostate position is accounted for by moving the patient so radiation beams line up with the target.

FM prostate localization is considered the "gold standard" image guidance technique for prostate IGRT because of its ability to measure prostate displacements with a precision of $\leq 2.0\ mm$ [12–14]. However, while safe and reliable [12–18], FM prostate localization requires an invasive procedure that presents a small risk of infection, bleeding, and discomfort to patients. To avoid these problems, a new type of image guidance was developed for prostate IGRT that uses ultrasound (US) to measure prostate displacements. This technique is commonly referred to as US prostate localization. Images of the prostate are acquired at time of treatment planning using either CT or US and again just before treatment delivery using US. Displacement of the prostate is determined by comparing treatment and planning images, and corrected for by moving the patient. In contrast to the FM method, US prostate localization is non-invasive and poses no associated risks to patients. A detailed overview of FM and US prostate localization is provided in the discussion of IGRT in section 2.2.

The main goal of this work is to determine if a new US prostate localization system, called the Restitu System (Resonant Medical, Montreal, QC), can replace FM prostate localization, or be used interchangeably, for prostate IGRT. A recent work suggests the Restitu System defines prostate displacement more accurately than an US prostate localization device commonly used for prostate IGRT [19]. However, comparison between the Restitu System and FM localization has not yet been reported, and therefore warrants detailed investigation. A study involving 8 patients was carried out at the BC Cancer Agency - Vancouver Island Center that produced over 150 measurements of prostate displacement using both the Restitu System and FMs. Ninety-five percent limits of agreement (LOA), described in section 4.3.2, were used to compare the two image guidance tools. An investigation into the possible

sources of discrepancy between US and FM measurements was also carried out. The variability associated with each technique was compared using an F-test, and the effects of US image quality on the LOA were evaluated. In addition, the intra- and inter-user variability associated with the new US system were quantified by calculating repeatability coefficients using analysis of variance. Lastly, the performance of the Restitu System was compared to that of a conventional patient re-positioning technique called bony anatomy matching (described in section 2.1.3). For this analysis, the planning target volume margins (outlined in section 2.1.2) required by each method were calculated and compared. The goal of this additional study was to evaluate the general clinical utility of the Restitu System.

Chapters 2 and 3 give basic overviews of radiation therapy and US respectively, while chapter 4 outlines the general methods and materials, including statistical analyses, used throughout this work. Chapters 5, 6, and 7 provide results and discussion on comparison of the Restitu System to FM prostate localization, possible sources of discrepancy between US and FM measurements, and the utility of the new US prostate localization system, respectively. Conclusions drawn from this work are given in chapter 8.

Chapter 2

Background I: Radiation Therapy

Radiation therapy (RT), or radiotherapy, involves the use of ionizing radiation to cure or relieve the symptoms of cancer. Radiation is used as a primary treatment for inoperable tumors, but may also be offered as an alternative to other more invasive modes of treatment like surgery or chemotherapy. In addition, radiation can be used as a compliment to surgery or chemotherapy, termed adjuvant radiation therapy.

The goal of RT is to deliver a lethal dose of radiation to a well-defined tumor volume while minimizing the dose, and hence damage, to surrounding healthy tissues [3]. Typically, the prescribed radiation dose is divided into equal "fractions" that are delivered daily over several weeks. This improves the outcome of treatment by allowing healthy cells time to repair and repopulate between exposures, and cancerous cells to proliferate to radiosensitive cell stages [3].

Common types of radiation used in RT are high energy electrons and x-ray or gamma-ray photons. Electrons, having low penetrating power, are used for superficial treatment of tumors that lie on or close to the surface of the skin. High energy (megavoltage) photons, on the other hand, have high penetrating power, and are used to treat deep seated tumors.

This chapter provides an overview of the principles and procedures used in photon RT treatments. Three dimensional conformal radiation therapy (3D CRT) is

discussed in section 2.1, followed by IGRT in section 2.2.

2.1 Three-Dimensional Conformal Radiation Therapy

Three-dimensional conformal radiation therapy is a highly advanced RT technique. Multiple radiation beams are shaped to match two-dimensional (2D) contours of the treatment target and delivered from different angles. This produces a 3D radiation dose distribution that conforms as closely as possible to the shape of the target volume [1]. The high degree of conformity associated with 3D CRT allows delivery of higher radiation doses compared to those used in conventional RT. Use of high radiation doses is commonly referred to as "dose escalation", and has been proven to increase the probability of curing the disease [3, 20, 21].

Figure 2.1 illustrates the steps involved in delivering a 3D CRT treatment. The process begins at CT simulation, where images of patient anatomy are acquired. These images are used during treatment planning to define target and critical structure volumes and create a radiation therapy treatment plan and digitally reconstructed radiographs. At each day of treatment, bony anatomy matching is performed and radiation is delivered.

In what follows, these processes are described in further detail. Section 2.1.1 describes CT simulation, followed by a discussion of treatment planning in section 2.1.2. Treatment delivery is described in section 2.1.3.

2.1.1 Computed Tomography Simulation

Computed tomography simulation is an essential component of 3D CRT. Images of patient anatomy are acquired with the patient positioned as they would be at treatment delivery. A radiotherapy treatment plan can then be created based on the information in these images without the patient present. In this way, CT simulation is a simulation of radiotherapy treatment [3].

A CT scan is composed of several adjacent x-ray images called "CT slices", or

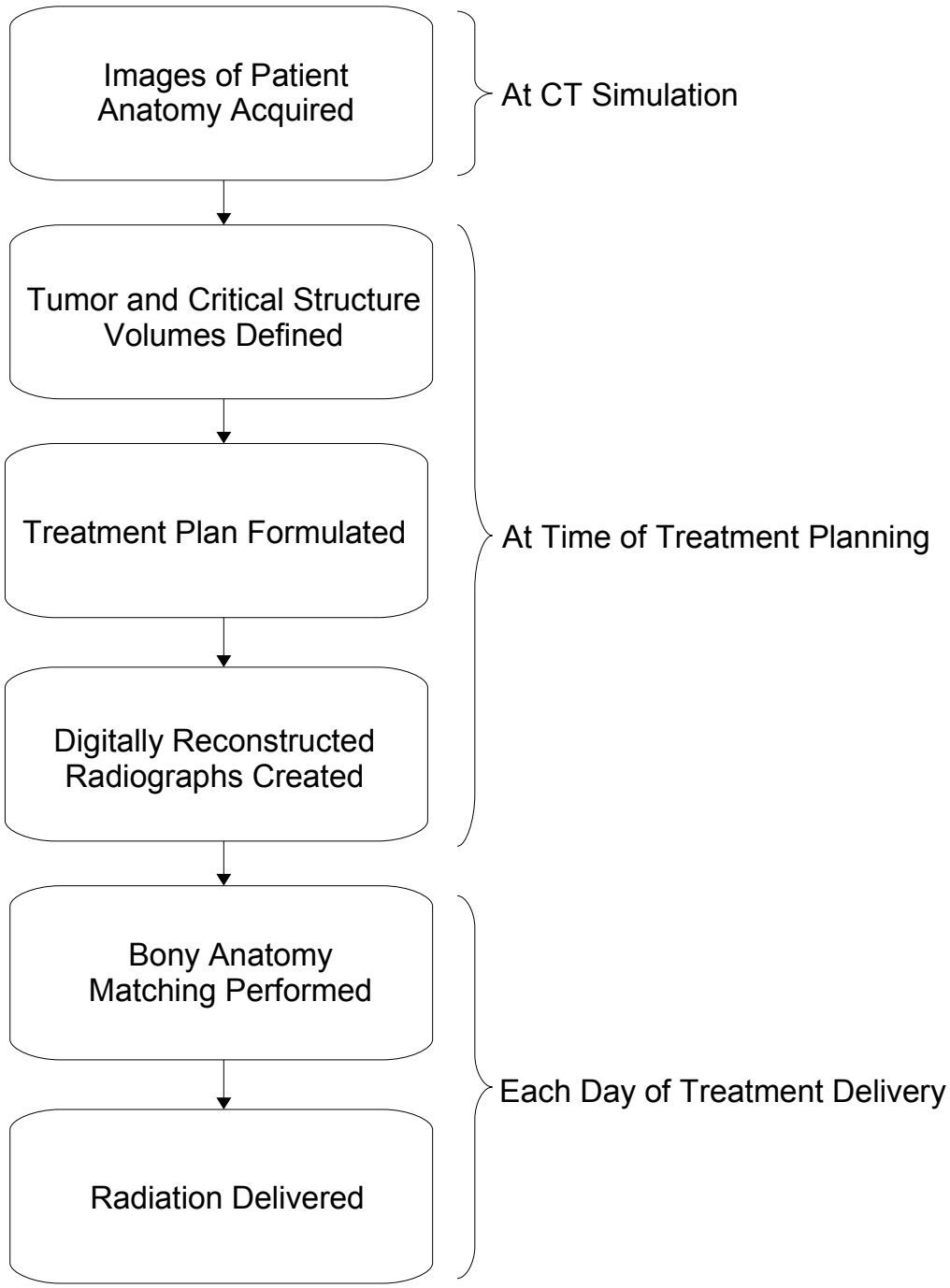

Figure 2.1: Steps involved in delivering a 3D CRT treatment: images of patient anatomy are acquired, tumor and critical structure volumes are defined, a radiation therapy treatment plan and digitally reconstructed radiographs are created, bony anatomy matching is performed, and radiation is delivered.

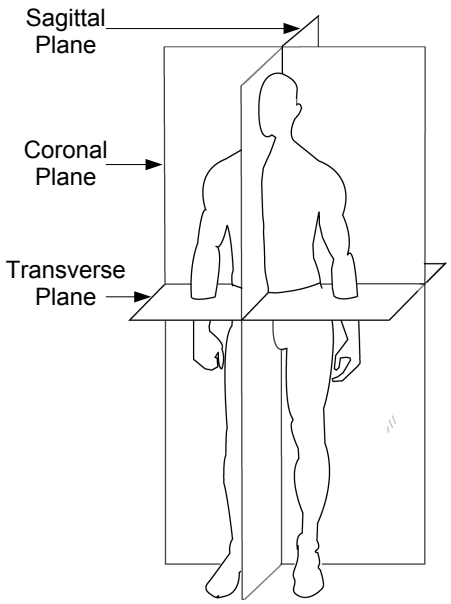

Figure 2.2: Perpendicular body planes: transverse, sagittal, and coronal.

simply "slices". Each slice is 1 - 10 mm thick [3], and shows a slab of patient anatomy in the transverse body plane. Figure 2.2 shows the three perpendicular body planes: transverse, sagittal, and coronal. The transverse plane divides the body into upper and lower portions, the sagittal plane divides the body into right and left portions, and the coronal plane divides the body into front and back portions. A typical slice showing the male pelvic anatomy is shown in Figure 2.3.

Figure 2.4 shows a typical CT simulator, consisting of a laser localization system, CT scanner, and computer graphics station [3]. The laser localization system defines the CT room coordinate system, and consists of three lasers that intersect at the CT room origin. This coordinate system is calibrated to match the treatment room coordinate system.

At the beginning of simulation, patients are positioned as they would be at treatment and radiopaque markers are affixed to where the lasers intersect their skin. These markers are visible on CT images and define patient position relative to the CT room and treatment room coordinate systems. When image acquisition is com-

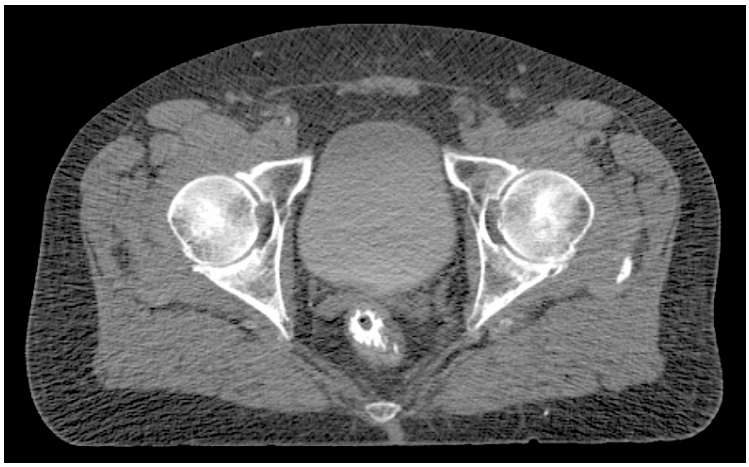

Figure 2.3: A typical CT slice showing the male pelvic anatomy.

plete, these markers are removed and replaced with permanent tattoos to be used for patient positioning at each day of treatment.

The CT scanner consists of a patient couch capable of horizontal and vertical translation and a hollow circular gantry. In a typical configuration, within the gantry, an x-ray tube is situated opposite an array of scintillation or gas-filled ionization x-ray detectors [2, 3]. As the scan proceeds, the couch and patient move into the gantry aperture at regular intervals. For each increment the couch advances, the x-ray tube rotates 360° while emitting a continuous fan beam of kilovoltage (kV) x-rays. As x-rays pass through the entire width of the patient, the detectors measure the intensity of the incident and transmitted beam at up to 1000 different angles [4]. Intensity measurements are then transferred to the computer graphics station for image processing.

Image processing proceeds automatically, and begins with conversion of intensity measurements into x-ray attenuation information. The intensity of attenuated x-rays transmitted through a uniform object, I_t, is related to the intensity of the incident beam, I_0, by Equation 2.1, where x and μ are the object's depth along the x-ray

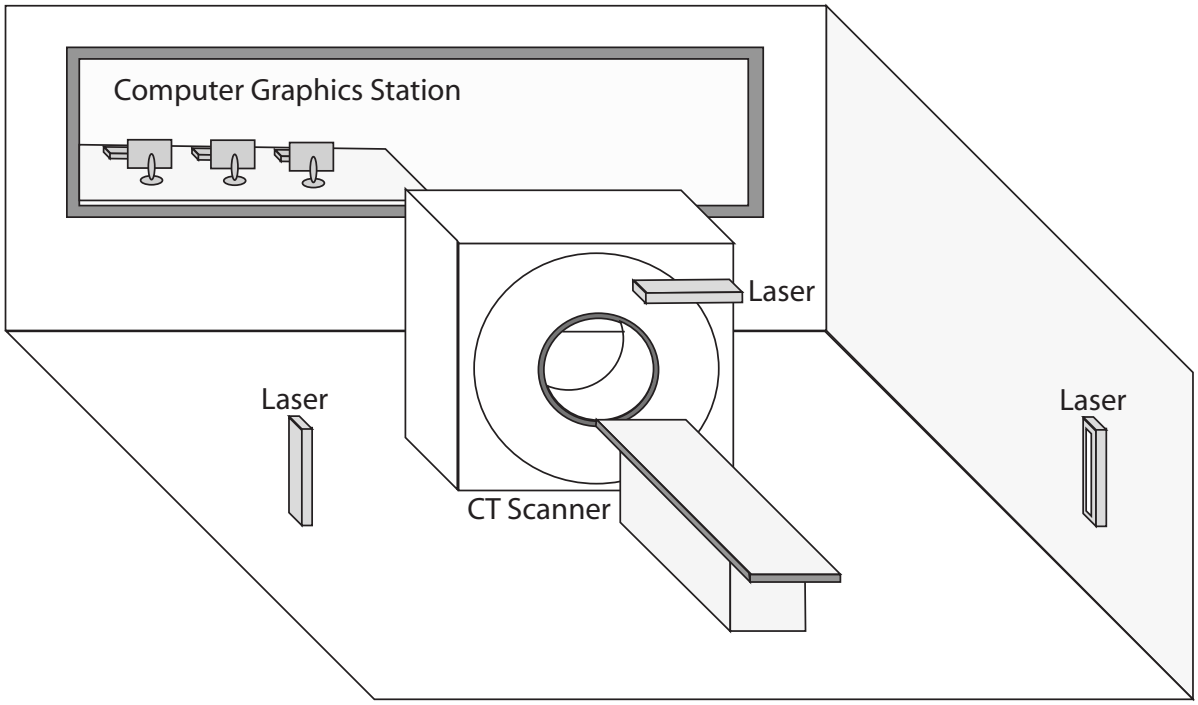

Figure 2.4: A typical CT simulator, consisting of a laser localization system, CT scanner, and computer graphics station.

beam path and linear attenuation coefficient respectively [3, 4].

$$I_t = I_0 e^{-\mu x} \tag{2.1}$$

Because the human body is made up of several different materials, each with its own linear attenuation coefficient, μ_i, each slab of patient anatomy imaged is divided into n square elements of thickness x_i along the path of x-ray transmission. The attenuation equation becomes:

$$I_t = I_0 e^{-(\mu_1 x_1 + \mu_2 x_2 + ... + \mu_n x_n)} \tag{2.2}$$

The linear attenuation coefficient for each element is determined by solving the system of attenuation equations generated by the multitude of intensity measurements [3].

The next stage of image processing is called filtered back-projection. Each μ_i is mathematically filtered using a Fourier transform to enhance image contrast, and backprojected onto a pixel in an image matrix [4]. Each pixel in the image matrix corresponds to a slab element, with 512 x 512 or 1024 x 1024 pixels per slice [3].

Filtered backprojection is followed by conversion of high-precision pixel data into integer CT numbers. Each CT number, $CT(x, y)$, represents a shade of gray in the image, and is calculated using Equation 2.3, where $\mu(x, y)$ is the filtered linear attenuation coefficient backprojected onto the pixel located at (x, y) in the image matrix, and μ_{water} is the linear attenuation coefficient for water [4].

$$CT(x, y) = 1000 \, \frac{\mu(x, y) - \mu_{water}}{\mu_{water}} \tag{2.3}$$

CT numbers determined using Equation 2.3 are expressed in Hounsfield units (H), where 1 H represents a change in linear attenuation of 0.1 % from that of water [1, 2]. CT numbers for various materials found within the body are summarized in Table 2.1. Thus, a gray-scale mapping of CT numbers produces anatomical images such as that shown in Figure 2.3.

Table 2.1: Computed tomography numbers for various materials within the body [1, 2].

Tissue	CT Number (H)
Water	0
Air	-1000
Bone	1000
Muscle	44 to 59
Blood	42 to 58
Fat	-20 to -100

2.1.2 Treatment Planning

Following CT simulation, a radiation therapy treatment plan is formulated. A treatment plan summarizes how a prescribed dose of radiation will be delivered to a cancer site using a medical linear accelerator. It is patient specific, and created using sophisticated software called a treatment planning system (TPS). The TPS allows users to generate virtual radiation beams and direct them at a patient who is represented in the software by images. The resultant dose distribution within the patient is then determined using a complex dose calculation algorithm.

Treatment plan formulation begins once images of patient anatomy are transferred from the CT computer to the TPS. Using special contouring tools, a radiation oncologist delineates treatment target and normal tissue volumes on each CT slice. This enables the oncologist to prescribe a lethal dose of radiation to a specific target volume and place limitations on the dose delivered to surrounding healthy structures.

Three target volumes are commonly defined: the gross tumor volume (GTV), clinical target volume (CTV), and planning target volume (PTV) [1]. The GTV is the gross visible extent and location of the tumor [22]. It is defined by the radiation oncologist based on information from imaging data and clinical examination of the affected area. The CTV contains the GTV and/or a margin to allow for microscopic disease that is invisible on CT images [22]. The size of the added margin is determined by the radiation oncologist, and often includes structures adjacent to the affected area that are at risk of containing the disease and require treatment. The PTV consists of the CTV plus a margin to account for uncertainties in CTV location [1]. These uncertainties result from patient movement, motion of internal organs that are part of or adjacent to the CTV, and mechanical uncertainties associated with radiation delivery devices (linear accelerator, field shaping devices, patient immobilization devices, etc.) [3]. The size of the added margin depends on the precision of the equipment used for treatment and the degree of anticipated CTV motion within

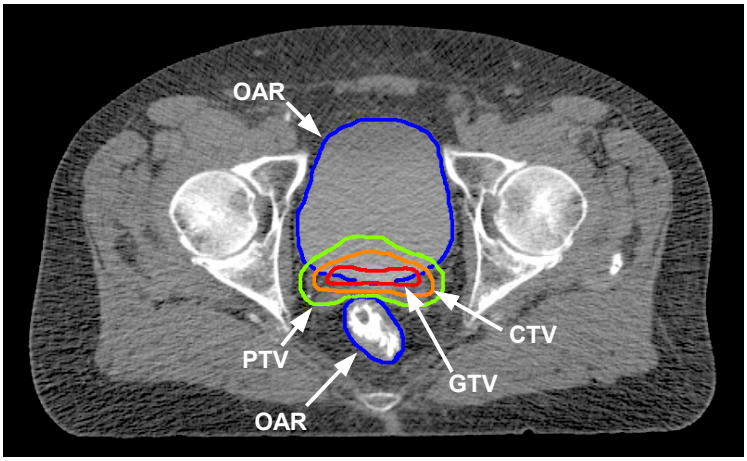

Figure 2.5: A typical CT slice showing the male pelvic anatomy with GTV, CTV, PTV, and OARs delineated.

the body. The PTV is the target volume used to define radiation beam characteristics in the treatment plan.

In addition to target volumes, the radiation oncologist must also define normal tissue, or organ at risk volumes (OARs). The OARs are the visible extent and location of healthy structures that appear in CT images and are located in close proximity to the PTV. The amount of radiation reaching OARs must be kept as low as possible to avoid injuring healthy structures. Figure 2.5 shows a typical CT image of the male pelvic anatomy with GTV, CTV, PTV, and OARs delineated.

Following volume definition, a radiation dosimetrist or medical physicist designs a radiation beam configuration that achieves, as closely as possible, the desired doses within the patient. Several parameters influence dose distribution, including the number of radiation beams, beam energy, the shape of each beam, and how each beam is directed at the patient. It is common to start with a standard beam configuration for a particular treatment site, and adjust each parameter until acceptable doses are delivered to each volume within the patient [1]. The result is an individualized patient treatment plan.

Several algorithms are available for dose calculation and are generally classified

as either correction-based or model-based [3]. Correction-based algorithms begin with a dose distribution measured in an all water absorber [1]. Correction factors that account for patient tissue inhomogeneities, irregular radiation field shapes, and distance from the radiation source to the treatment target are applied to this distribution to determine doses within the patient [1, 3]. While correction-based algorithms require little computation time, they possess limited accuracy, and are not common in modern TPSs.

Model-based algorithms use information about photon interactions with matter to simulate radiation transport through patient tissue and calculate the resulting dose deposited [1, 3]. Two model-based algorithms are of particular note: the convolution method, and the Monte Carlo method.

The convolution method calculates dose by separating the radiation beam into primary and scattered components. The dose, $D(\overrightarrow{r})$, at a point $\overrightarrow{r}$ is given by Equation 2.4, where $T(\overrightarrow{r}')$ is the total energy released per unit mass (TERMA) by primary photons and $K(\overrightarrow{r} - \overrightarrow{r}')$ is the scatter convolution kernel [1].

$$D(\overrightarrow{r}) = \int T(\overrightarrow{r}')\ K(\overrightarrow{r} - \overrightarrow{r}')\ d^3\overrightarrow{r}' \tag{2.4}$$

The scatter convolution kernel is a matrix that represents the dose distribution created by secondary photons and electrons that emerged from interaction of primary photons with tissue [1]. Convolving the TERMA and scatter convolution kernel over a particular volume gives the total dose [1]. The convolution method is popular in modern TPSs because it can calculate dose distributions with a high degree of accuracy in a reasonable amount of time [1].

The Monte Carlo method simulates radiation interactions within the patient based on probability distributions for photon and charged particle interactions with matter [1]. The dose distribution is determined by accumulating the energy deposited by

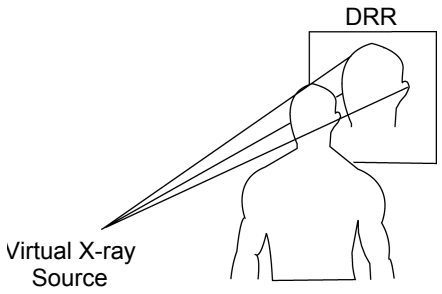

Figure 2.6: Virtual ray tracing for DRR construction.

these interactions in several 3D tissue boxes called "voxels" [1]. At present, long computation times prevent the Monte Carlo method from being used regularly in radiation therapy TPSs. However, it is expected that the Monte Carlo method will supersede convolution in the near future because it is the most accurate dose calculation algorithm available [1].

Once a treatment plan is designed that achieves the desired dose distribution within the patient, the TPS is used to create digitally reconstructed radiographs (DRRs). DRRs are computer generated, virtual x-ray images used to check that patients are positioned at the treatment unit as at CT simulation. They are constructed by tracing x-rays diverging from a virtual source through the patient, who is represented by the same set of adjacent CT images used for treatment plan creation. Figure 2.6 illustrates the virtual ray tracing process. Since the linear attenuation coefficient for each pixel of each CT slice is known, the intensity of rays traced through the patient can be calculated using Equation 2.2. The set of transmission values produced is mapped onto a 2D pixel array of its own to produce the DRR image [3]. Figure 2.7 shows a typical coronal DRR of the male pelvic anatomy.

Following DRR construction, the treatment plan and DRRs are transferred to the treatment unit to be used for treatment delivery.

Figure 2.7: A typical DRR showing a coronal view of the male pelvic anatomy.

2.1.3 Treatment Delivery

Three-dimensional conformal radiation therapy can be delivered to patients using a number of different treatment devices, including cobalt-60 teletherapy machines, gamma or cyber knife radiosurgery units, or tomotherapy machines, but the most commonly employed device is the medical linear accelerator (LINAC). Figure 2.8 shows a typical LINAC treatment unit, composed of a computer control station and treatment room, separated by protective shielding. The treatment room consists of a laser localization system, treatment couch, LINAC housed within a rotating gantry and stand, and electronic portal imaging device.

Linear accelerators produce megavoltage (MV) x-ray and megaelectron volt electron beams by accelerating electrons to high speeds using microwaves in an accelerating wave guide [1]. Figure 2.9 shows the components of a typical LINAC and their relationships to one another. A modulator cabinet converts facility power into high voltage pulses, and delivers them to an electron gun and microwave power source

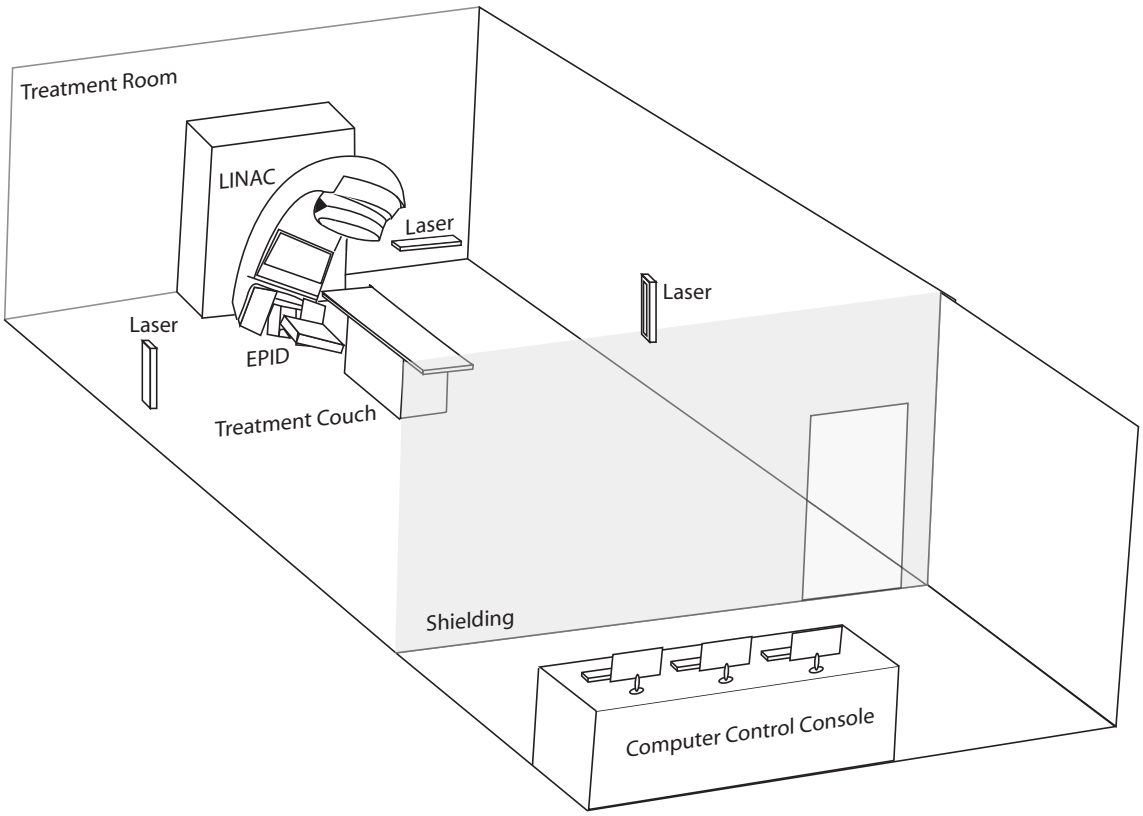

Figure 2.8: A typical LINAC treatment unit.

simultaneously. This triggers the electron gun to emit pulses of electrons at the same instant the microwave power source produces pulses of microwaves, which both enter the accelerating wave guide at the same instant [1, 3, 23]. The accelerating wave guide consists of an evacuated copper tube divided into sections by copper disks. As the microwaves propagate through the structure they transfer energy to the electrons, causing the electrons to accelerate to high speeds. The resulting narrow pencil beam of high energy electrons exits the accelerating wave guide and is directed to the treatment head by a bending magnet assembly [1, 3, 23].

For photon therapy, the electron beam enters the treatment head and strikes a material of high atomic number, like tungsten, producing a MV x-ray beam through bremsstrahlung interactions. The x-ray beam emerging from the target passes through

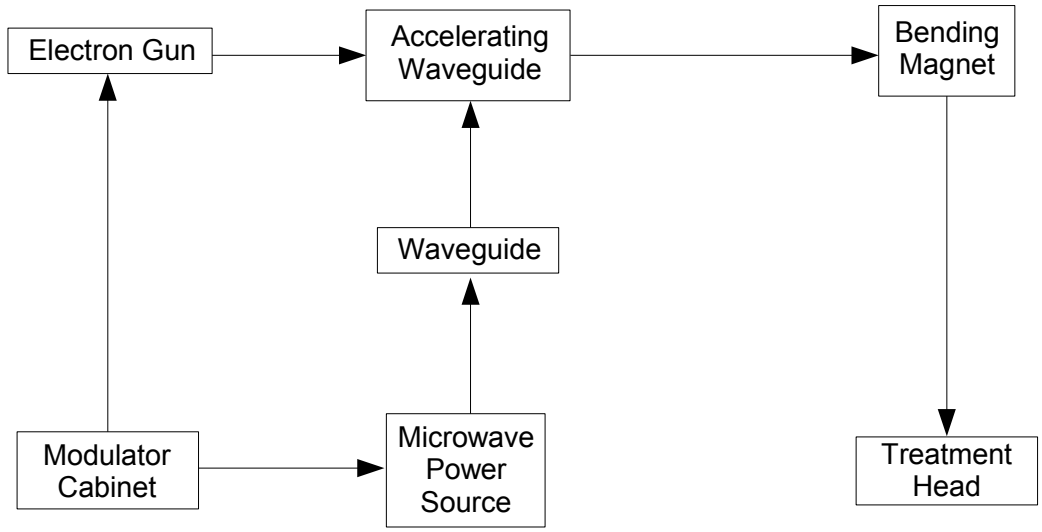

Figure 2.9: LINAC components and their relationships to one another.

a series of collimators and filters to produce a beam of desired shape and intensity. Beam shaping is often achieved using a multileaf collimator. Multileaf collimators consist of a large number of collimating leaves that can be moved independently of one another to achieve a radiation field of any shape [1]. Adjustment of leaf position is computer controlled, allowing rapid treatment using multiple beams of varying size and shape.

The other components of the treatment room serve to position the patient for treatment. The laser localization system defines the treatment room coordinate system, and consists of three or more lasers that intersect at the treatment room origin. The treatment couch can move in three mutually perpendicular directions. At each day of treatment, patients are positioned on the treatment couch as they were at CT simulation, by aligning their tattoos with the treatment room lasers. To ensure consistent patient positioning between CT simulation and treatment delivery, patient set-up errors are then measured and corrected using bony anatomy matching (BAM).

BAM begins by creating matching templates from the DRRs constructed at treat-

ment planning. Each template is an image that shows the position of patient bones with respect to the radiation beam indicated in the treatment plan. On the first day of treatment, a radiation therapist retrieves the DRR created at treatment planning and overlays the planned radiation field aperture onto the image. They then outline the important bony structures that appear. The radiation field aperture and bony anatomy contours constitute the matching template.

On the first and subsequent days of treatment delivery, an additional x-ray transmission image is acquired of the same area of patient anatomy that is shown in the DRR, with the patient in the treatment position. These images also show the radiation field aperture and patient bony anatomy, and are called electronic portal images (EPIs).

Electronic portal images are acquired using the electronic portal imaging device (EPID). The EPID is a flat panel detector array, mounted onto the rotating gantry opposite the treatment head [23]. Most modern EPIDs consist of a scintillator placed in direct contact with a layer of amorphous silicon deposited on a glass substrate [3]. Each pixel in the detector array is made up of a photodiode and thin film transistor implanted in the amorphous silicon [1, 3]. Megavoltage x-rays exiting the treatment head pass through the patient and are converted into visible photons by the scintillator. Light leaving the scintillator is converted into electric charge by the photodiodes and stored until exposure is complete. At readout, each thin film transistor acts as a switch that allows the charge to flow out of the photodiodes to the charge amplifier, row by row. The charge amplifier records the charge accumulated in each pixel, which is proportional to the number of photons reaching that pixel of the detector [3].

Figure 2.10 shows a typical EPI of the male pelvis. Patient anatomy appears dark and is bounded by the field aperture (thick black outline). The white lines within the dark region are pelvic bones. It is important to note that the dose delivered to

patients in acquiring EPIs is incorporated into the treatment plan, so no additional dose is delivered to patients.

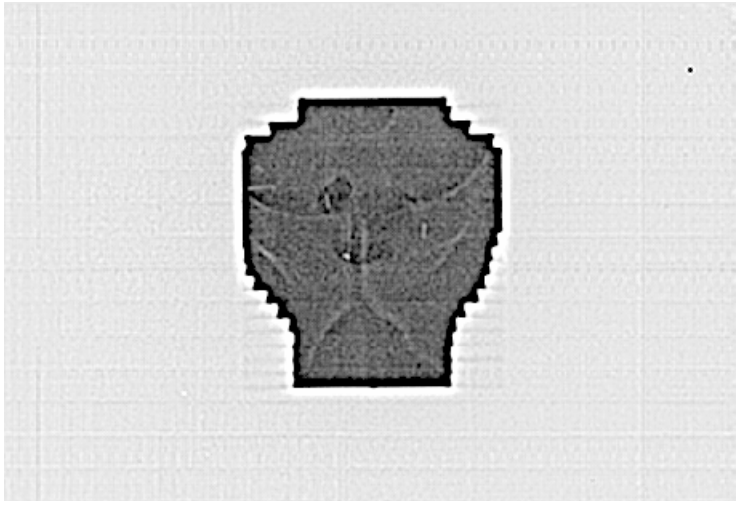

Figure 2.10: A typical EPI showing a coronal view of the male pelvic anatomy.

Following EPI acquisition, the BAM template discussed above is overlaid onto the EPI. The contours of patient bones that appear in the template are placed over the corresponding bones that appear in the EPI. If the patient is not positioned correctly, the radiation field aperture that appears in the template will not line up with the aperture in the EPI. Any displacement between template and EPI field apertures is measured and corrected by moving the treatment couch. This corrects any patient set-up errors before the prescribed radiation dose is delivered.

2.2 Image Guided Radiation Therapy

While 3D CRT is an effective radiation therapy technique for static tumors, it can be limiting when treating mobile disease sites. For some disease sites, the location of a tumor with respect to the radiation beam can change between time of treatment planning and treatment delivery. This is primarily caused by organ motion, motion of internal organs that are part of or adjacent to the tumor [24], and to a lesser extent, by patient set-up errors. If the tumor is displaced from its position at time

of treatment planning, the treatment may fail to eradicate the disease, and may also injure surrounding healthy tissue.

As discussed, 3D CRT aims to account for tumor displacement using BAM to correct patient set-up errors, and PTV margins are constructed large enough to encompass the anticipated range of tumor motion. Unfortunately, large PTV margins tend to include significant portions of normal tissue, resulting in overexposure of healthy structures - especially for treatments involving escalated doses. To avoid injuring critical structures while maintaining a high degree of target conformity, a new type of radiation therapy was introduced called IGRT. Image guided radiation therapy corrects patient set-up errors and organ motion on each day of treatment using image guidance to reposition the target.

Figure 2.11 shows the steps involved in delivering an IGRT treatment. Computed tomography simulation proceeds as outlined in Section 2.1.1. In addition, planning IGRT images of the treatment site are acquired with the patient still positioned at the CT simulator. Depending on the image guidance system used, these images can be the CT images themselves, or additional images acquired through another imaging modality. Planning IGRT images show the target in a coordinate system that is calibrated to match the coordinate system of the treatment room. They define the target "planned position", the position of the target when the treatment plan is created. Following CT simulation, tumor and critical structure volumes are defined on CT slices, and a treatment plan is formulated as outlined in section 2.1.2.

At each day of treatment, patients are positioned on the treatment couch as they were at CT simulation, by aligning their tattoos with the treatment room lasers. Treatment IGRT images are acquired that show the target in the treatment room coordinate system for that particular day of treatment. Any displacement in target position is measured by comparing the position of the target in treatment and planning IGRT images.

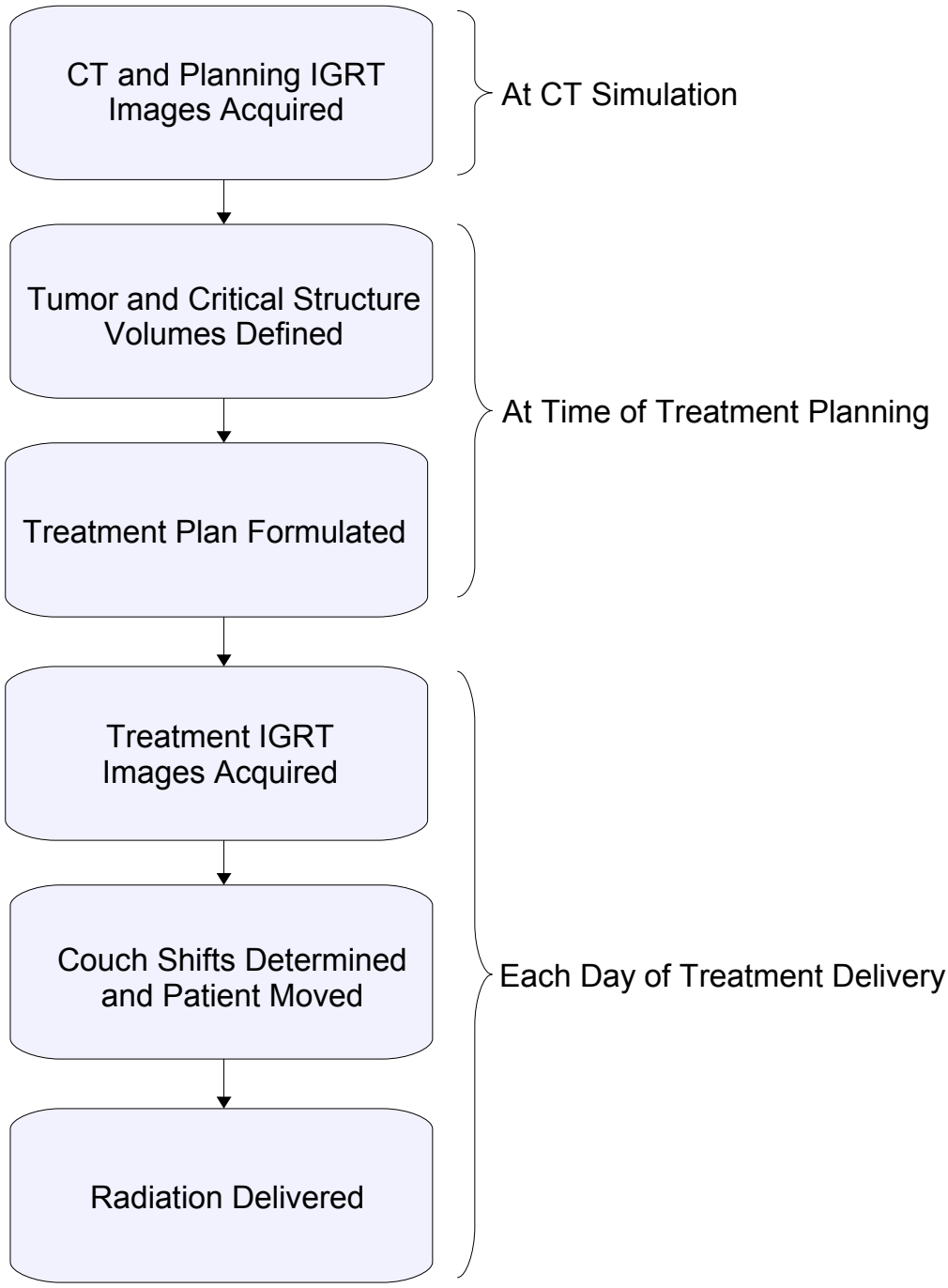

Figure 2.11: Steps involved in delivering an IGRT treatment.

The target is returned to the planned position by moving the treatment couch, and hence patient, by an amount equal to the target displacement, but in the opposite direction. These repositioning movements are called "couch shifts". Couch shifts are 3D vectors. The direction of each component is indicated using anatomical direction terms, which are illustrated in Figure 2.12. One couch shift component indicates whether to move the couch anterior, towards the front of the body, or posterior, towards the back of the body. Another component indicates whether to move the couch superior, towards the head, or inferior, towards the feet, and the last component indicates whether to move the couch towards the patient's right or their left. After the patient is repositioned, radiation is delivered.

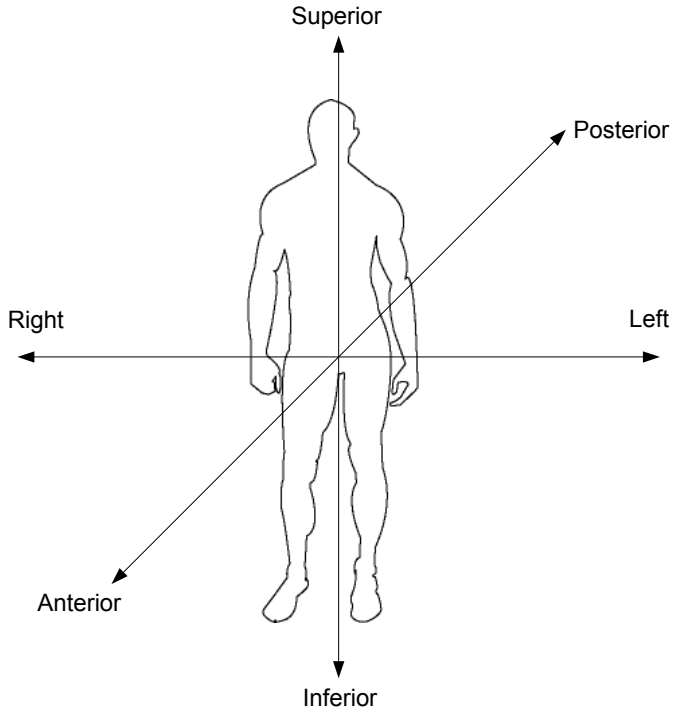

Figure 2.12: Anatomical directions: anterior and posterior, right and left, and superior and inferior.

Several image guidance techniques are available for IGRT, and are largely treatment site specific. As this work focuses primarily on IGRT for prostate cancer,

discussion of image guidance methods will be limited to those that correct prostate displacements. The reader is referred to the literature for a detailed discussion on image guidance systems for other mobile treatment sites.

The currently accepted image guidance technique for prostate cancer is FM prostate localization. Using this method, radiopaque FMs are inserted into the prostate before treatment planning. Images acquired at CT simulation show the FMs within the pelvic bony anatomy. FMs are outlined on each CT image slice, and these contours appear in the DRRs.

Typically, two perpendicular DRRs are created at treatment planning, one showing an anterior view of the patient, called the anterior DRR, and one showing a left lateral view, called a left lateral DRR. Anterior DRRs show patient anatomy in the coronal plane (see Figure 2.2), viewed from in front of the body, while left lateral DRRs show anatomy in the sagittal plane (see Figure 2.2) viewed from the patient's left.

On the first day of treatment, FM matching templates are created from DRRs. These templates are images that show the FMs and planned radiation field aperture. Following template creation, and on each subsequent day of treatment, EPIs are acquired of the pelvic area that show the FMs and the treatment field aperture. As with BAM, the dose delivered to patients in acquiring EPIs for FM prostate localization is incorporated into the treatment plan. The FM matching template is positioned over the EPI so that one FM in the template lines up with the corresponding FM in the EPI. If the prostate is displaced from its position at time of treatment planning, when the FMs coincide, the planned radiation field aperture in the template will not line up with the treatment field aperture in the EPI. The difference between the location of the planned and treatment field apertures provides a measure of the displacement of the particular FM between time of treatment planning and that day of treatment delivery. The process is repeated for the other FMs, and the displacements of all

FMs implanted (typically 3) are averaged to give the displacement of the center of mass of the prostate gland. This displacement is corrected by shifting the couch in amounts equal to the prostate displacement, but in the opposite direction.

While FM prostate localization is well established and reliable [12–18], it requires an invasive procedure and presents a small risk of infection, bleeding, and discomfort to the patient. For this reason, other methods of prostate localization have been introduced, including cone-beam CT (CBCT), stereoscopic x-ray, and US image guidance systems.

Cone-beam computed tomography image guidance systems acquire treatment IGRT images using a CBCT scanner mounted onto the LINAC gantry. A CBCT scanner consists of a kV x-ray source positioned opposite a kV EPID. The line formed between the CBCT x-ray source and kV EPID is perpendicular to the line formed between the LINAC treatment head and MV EPID. In contrast to conventional CT scanners, x-rays diverging from the CBCT x-ray source form a cone large enough to image the entire treatment site using only one rotation of the scanner. Treatment DRRs are constructed from the CBCT data and compared to planning DRRs to determine couch shifts required to return the target to its planned position. Couch shifts can be computed by aligning the soft tissue that appears in both images (similar to BAM except soft tissue is used instead of bones), or by aligning fiducial markers implanted into the prostate before treatment planning. While CBCT is a useful image guidance technique, it involves delivery of additional dose to patients during CBCT image acquisition, and, if used in conjunction with implanted FMs, poses a risk of infection and discomfort to patients.

Stereoscopic kV x-ray image guidance systems acquire treatment images using two kV x-ray units. Each unit consists of a kV x-ray source fixed to the treatment room floor, and a kV EPID mounted on the treatment room ceiling opposite the x-ray source. The x-ray units are installed in the treatment room such that x-ray

transmission images of the prostate and surrounding tissue are acquired from two different angles. These images are then used to create a stereoscopic x-ray image that shows a 3D view of the pelvic area. The stereoscopic image is compared to planning DRRs to determine prostate displacement, and the position of the treatment couch is automatically adjusted to re-align the target using specially designed robotics. Couch shifts are computed by comparing bony anatomy or fiducial markers. Similar to CBCT, this method introduces a small, but additional dose to the patient, and if FMs are used, poses a risk of infection and discomfort to patients.

In contrast, US localization systems do not require FM implantation, nor additional dose to be delivered to patients. US localization systems fall into two categories: inter- and intra-modality. Inter-modality US systems compare US images acquired each day at the treatment machine to target and critical structure volumes outlined on CT images at treatment planning. These contours are imported into the US localization system and positioned over the corresponding structures that appear in the US image. Any displacement in prostate position is measured and accounted for by adjusting the position of the treatment couch.

Intra-modality US localization systems, like the Restitu System examined in this work, compare two US images to determine prostate displacements. Immediately following CT simulation, an US scan of the pelvic area is acquired that shows the prostate gland and surrounding tissues using an US station located in the CT simulator room. At each day of treatment, an additional US scan is acquired that again shows the pelvic anatomy using an US station located in the treatment room. Prostate displacements are measured by comparing the position of the prostate in treatment and planning US images. Couch shifts to realign the prostate into the treatment field are then calculated and performed if necessary. Further details on the Restitu System are given in section 4.2.

Chapter 3

Background II: Medical Ultrasonography

Medical ultrasonography is a common method for visualizing internal structures within the body. It is based on the detection and display of high-frequency sound waves, called ultrasound, that have reflected off organ and tissue interfaces. By measuring the amplitude of each reflection, high-resolution, gray-scale images are produced [25].

Medical ultrasonography has become one of the leading imaging modalities available, with millions of US scans acquired each year worldwide. The popularity of US as an imaging tool stems from its low cost, safety, and diverse applicability [4, 25]. In obstetrics, US is used to provide information about the age of a growing fetus and to detect any fetal abnormalities that may be present [26]. Ultrasound images can be used to monitor the status of organ transplants as well as guide needle biopsies that provide important information about the presence and extent of certain cancers [25]. In radiation therapy, US images are used to determine the location of specific structures [25]. These are but a few examples of how medical ultrasonography is used today.

This chapter provides an overview of medical ultrasonography. Ultrasound waves and their interactions with matter are discussed in section 3.1. Section 3.2 details US image formation while section 3.3 describes the equipment used to produce 2D

US images and 3D US volumes. Ultrasound image quality is discussed in section 3.4

3.1 Characteristics of Ultrasound

Ultrasound signals are sound waves with frequencies greater than 20 kHz. Like all sound, US travels through a medium as a pressure wave. Individual US waves interact with each other through constructive and destructive interference, and with the medium through which they propagate by reflection, refraction, scattering, and absorption. In what follows, US waves and their interactions are described in further detail.

3.1.1 Ultrasound Waves

Ultrasound pressure waves result from the back and forth vibration of the molecules in the medium through which they travel. Vibration can occur perpendicular to the direction of propagation, as for transverse waves, but in tissue and fluids, vibration is parallel to the direction of wave advancement. Hence, US waves are longitudinal pressure waves [25].

To illustrate propagation of US through tissue, consider the 2D molecular lattice shown in Figure 3.1. At time $t = 0$, the lattice is in an equilibrium state, and the pressure is uniform throughout the volume. At time $t = 1$, a piston applies an external force to the lattice, causing the molecules in column 1 to advance and collide with the molecules in column 2. While the molecules are in contact, a region of higher density and pressure is created, called the "zone of compression" [4], and energy is transferred from molecules in column 1 to those in column 2.

At time $t = 2$, the piston returns to its original position. Molecules in column 2 advance and collide with molecules in column 3, causing the zone of compression to move forward. Meanwhile, molecules in column 1 travel backwards, beyond their equilibrium position, creating a region of reduced density and pressure immediately behind the zone of compression. This region is called the "zone of rarefaction" [4].

At time $t = 3$, molecules in column 3 move forward and collide with molecules in column 4, while the molecules in column 2 travel backwards. As a result, the zones of compression and rarefaction advance, and will continue to propagate through the lattice by the same mechanism.

The zones of compression and rarefaction create an isolated disturbance commonly referred to as a wave "pulse". In medical US imaging, each US pulse usually consists of 3 sets of compression and rarefaction zones, or three "cycles" [4], and can be described by a sinusoidal waveform similar to the one shown in Figure 3.2.

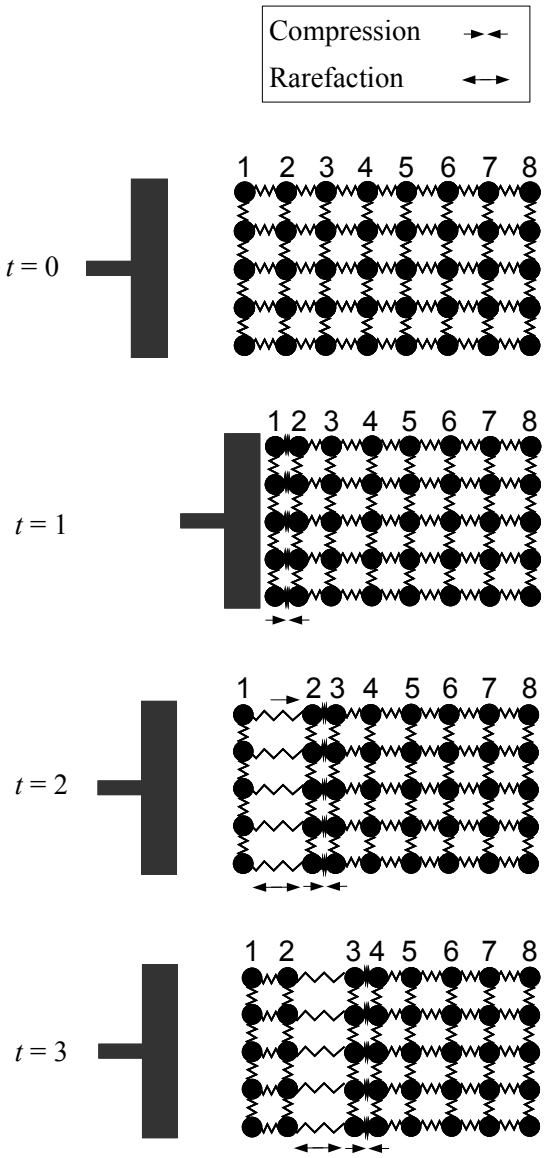

Figure 3.1: Propagation of a pressure wave through a 2D molecular lattice.

Sinusoidal waves are characterized by their wavelength, period or frequency, and speed. Sound waves with frequencies less than 15 Hz are known as infrasound, while those between 15 $Hz - 20$ kHz are called audible sound waves. As mentioned above, sound waves with frequencies that lie above the audible range are known as US. For medical applications, US frequencies lie between $2 - 15$ MHz, corresponding to wavelengths of $0.8 - 0.1$ mm [4, 25].

The speed of US propagation, c, is dependent on the physical properties of the medium through which the signal travels, and is given by Equation 3.1, where λ and

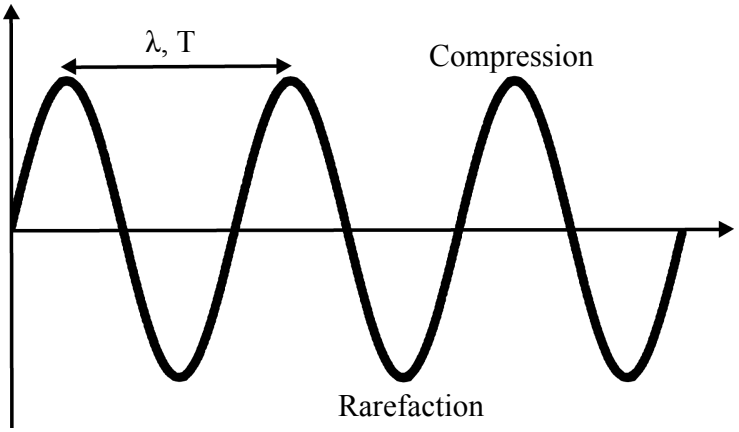

Figure 3.2: An example of a typical sinusoidal wave with 3 cycles.

ν are the wavelength and frequency of the US wave respectively (note that the speed of light in a vacuum is also represented by the symbol "c").

$$c = \lambda\nu \tag{3.1}$$

Ultrasound propagation speed increases with increasing medium stiffness, and decreases with increasing medium density. Most US devices assume an average propagation speed of 1540 m/s for soft tissue, while through water and dense bone, ultrasound travels at 1480 m/s and 4080 m/s respectively [25].

The speed of US can be used to determine the distance between the surface of the propagation medium and the interface where a reflection occurs. An US pulse is transmitted through the medium, and the time for the signal to reach a given interface and return is measured. Using this and the speed of US propagation in the medium, the distance traveled can easily be calculated. For example, if it takes 0.00015 s for an US pulse to travel from the surface of the body to an internal boundary and return, and the speed of US in tissue is approximately 1540 m/s, the distance traveled is:

$$d = \frac{(0.00015\ s \times 1540\ m/s)}{2} = 0.12\ m \tag{3.2}$$

where division by 2 accounts for travel to the interface and back again [25].

The speed of US propagation can also be used to determine the acoustic impedance of a given material. Acoustic impedance is a measure of how resistant a material is to sound propagation, and is analogous to resistance in electrical circuit theory. Equation 3.3 gives the formula for acoustic impedance, Z, where ρ is the density of the propagation medium.

$$Z = c\rho \tag{3.3}$$

Lastly, interactions between individual US waves are governed by the superposition principle. This states that the pressure amplitudes of two or more interfering US waves add to produce a composite wave. If the waves reinforce each other to produce a composite wave with a greater pressure amplitude, the interference is said to be "constructive". If the waves tend to cancel each other out, producing a composite wave with decreased pressure amplitude, the interference is said to be "destructive".

3.1.2 Interactions of Ultrasound with Matter

Ultrasound interacts with the medium through which it propagates by reflection, refraction, scattering, and absorption [4]. These processes are shown in Figure 3.3.

Reflection occurs when an US pulse strikes a specular reflector, an interface between two materials whose structural variations are much smaller than λ. The reflection is caused by differences in the acoustic impedance of the two materials, with larger differences resulting in a greater portion of the incident wave being reflected. The large difference between the acoustic impedances of air and skin cause 100 % reflection of US pulses at the interface between these materials. This makes imaging of internal anatomy impossible without acoustic coupling gel, used to eliminate air-skin interfaces in medical US imaging [4].

Figure 3.3a shows reflection of an US pulse that is normally incident on an interface between two materials with different Z. A fraction of the signal, called the

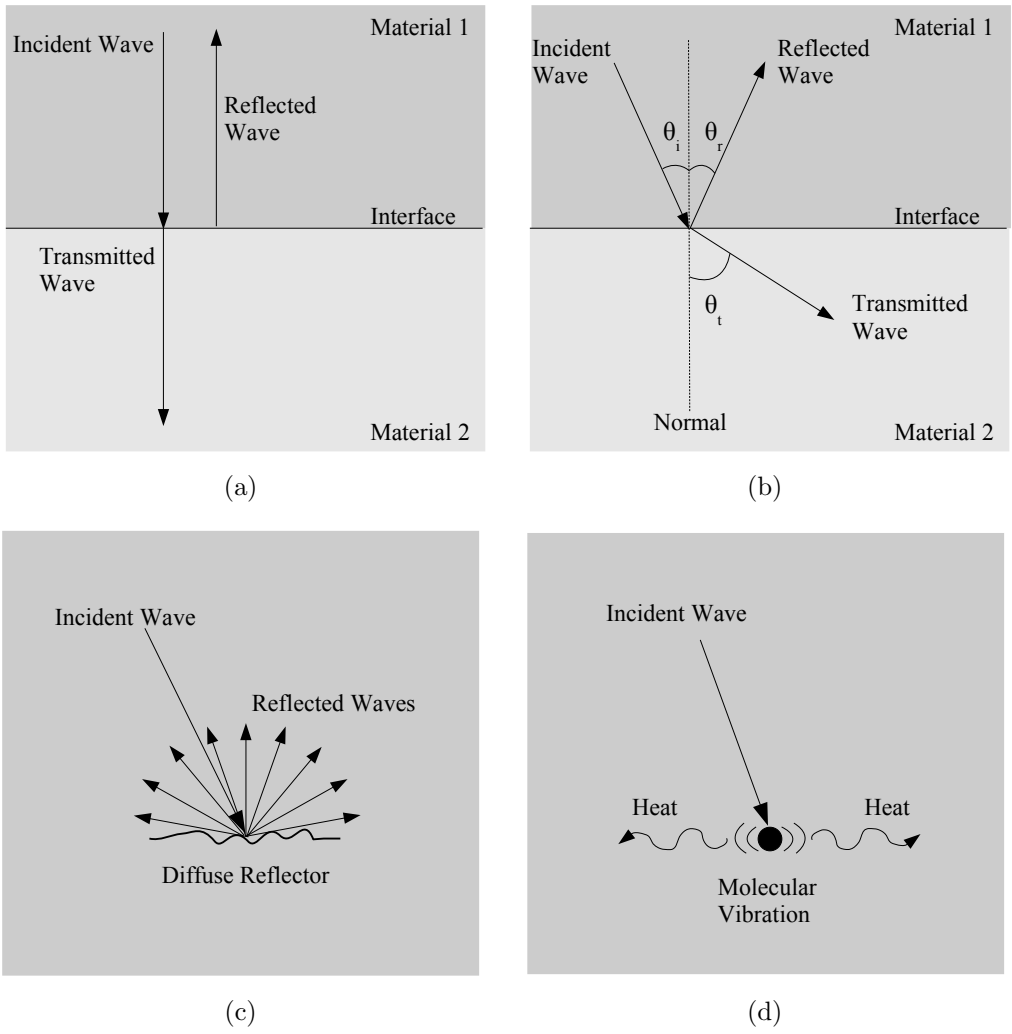

Figure 3.3: Interactions of US with matter: a) reflection and transmission at normal incidence, b) reflection and transmission at non-normal incident (refraction), c) scattering, and d) absorption.

"echo", is reflected 180° at the interface and travels along the same path as the incident wave but in the opposite direction. This process is critical for producing US images, as signals that return from organ and tissue interfaces along the same path as the incident US pulse are used to form the image. The remaining US signal is transmitted through the medium in the same direction as the incident signal.

Figure 3.3b illustrates reflection and refraction of an US pulse that strikes an interface at incident angle θ_i to the normal. The echo is reflected at angle θ_r from

the normal, equal to the incident angle, and continues to travel through the first material. The remaining signal is refracted through the interface, and propagates through the second material at a different angle [4]. This angle, θ_t, is related to θ_i by Snell's law [2] :

$$\frac{\sin\theta_t}{\sin\theta_i} = \frac{Z_2\rho_1}{Z_1\rho_2} = \frac{c_2}{c_1} \tag{3.4}$$

where Z_1 and ρ_1 are the acoustic impedance and density of the first material, and Z_2 and ρ_2 are the acoustic impedance and density of the second material respectively.

In addition to reflection and refraction, the US pulse is exponentially attenuated as it passes through a medium via scattering and absorption [4]. Scattering occurs when US waves strike non-specular, or diffuse, reflectors, and is shown in Figure 3.3c. Diffuse reflectors are interfaces with surface variations close to or smaller than λ. Ultrasound waves "see" diffuse reflectors as rough surfaces, and are reflected off them in all directions. These reflectors cause the characteristic grainy appearance [4, 25] present in most US images.

Figure 3.3d shows absorption of acoustic energy by the propagation medium. When molecules in the medium collide during a compression, most of the incident molecule's energy is transferred to another molecule. The fraction of energy that remains with the incident molecule is considered absorbed by the medium. This energy is converted into heat [4] through damped oscillation of the incident molecule.

3.2 Ultrasound Image Formation

Ultrasound images are formed using the "pulse-echo" technique, and can be viewed using either A-mode, B-mode, or M-mode display. A-mode and B-mode display provide spatial information about the anatomy being imaged while M-mode provides motion or velocity information. Detailed discussions on the pulse-echo technique and A-mode and B-mode display are provided below. As this work focuses primarily on the spatial information provided by US imaging, the reader is referred to the

literature for a detailed discussion on M-mode US display.

3.2.1 Pulse-Echo Technique

Using the pulse-echo technique, a transducer, detailed in section 3.3.1, transmits a series of US pulses into the body, where they reflect off tissue and/or organ interfaces, producing echoes which return to and are detected by the same transducer. Pulses are typically transmitted at a rate of 1000 pulses per second [2], with the transducer "listening" for the returning echoes between delivery of each pulse. Echoes that return along the same path as the incident US signal strike the transducer, producing a measurable potential difference, whose amplitude is proportional to the amplitude of the reflected echo [4]. By measuring the time interval between transmission of the initial US pulse and detection of a returning echo, the depth of the echo-producing interface is determined as in section 3.1.1. The resulting US image is then constructed based on echo amplitude and reflector position [4, 25].

3.2.2 Modes of Display

A-mode, or "amplitude"-mode, display makes use of an oscilloscope to illustrate echo amplitude as a function of time. Simultaneous to the transducer sending an US pulse into the body, the trace of the oscilloscope begins a uniform sweep across the horizontal time axis of the screen. The potential difference produced across the transducer by each returning echo is displayed as a spike on the vertical voltage axis. The oscilloscope is calibrated so the horizontal position of each spike represents the distance between the reflective interface and the surface of the skin. The scope produces one horizontal sweep for each US pulse transmitted, providing echo information for anatomy along one line of site of the transducer, or one *scan line*. If multiple voltage spikes appear along the x-axis of the oscilloscope during a single trace sweep, multiple reflecting interfaces are present along the scan line in question [2, 4, 27]. A typical A-mode US image is shown in Figure 3.4

Figure 3.4: An example of a typical A-mode US image.

A-mode was the first US display configuration used for medical applications [2], and is still employed in ophthalmology to measure precise distances in the eye, and in echoenephalography to measure displacement of the midline of the brain [2, 4]. However, due to its inability to provide 2D representations of anatomy, A-mode has been replaced by B-mode display for most medical applications.

B-mode, or "brightness"-mode, display provides 2D, gray-scale images of anatomy in real-time [2, 4, 25]. B-mode images are constructed using echo information from an array of scan lines that are produced by sweeping US pulses across the area being imaged from one side to the other. This process is illustrated in Figure 3.5. The first B-mode scanners swept US pulses across the body by manually adjusting the position of the transducer. Due to advancements in signal processing and transducer design, this technique is no longer employed, as modern B-mode scanners can adjust the transmission location of each US pulse electronically without moving the transducer.

Regardless of how pulses are moved, B-mode US signals are transmitted and detected one scan line at a time, and the amplitude of each potential difference produced by a returning echo is mapped onto a pixel in a 2D image matrix. Modern US image matrices consist of 512 x 512 or 512 x 640 pixels, with each pixel capable of

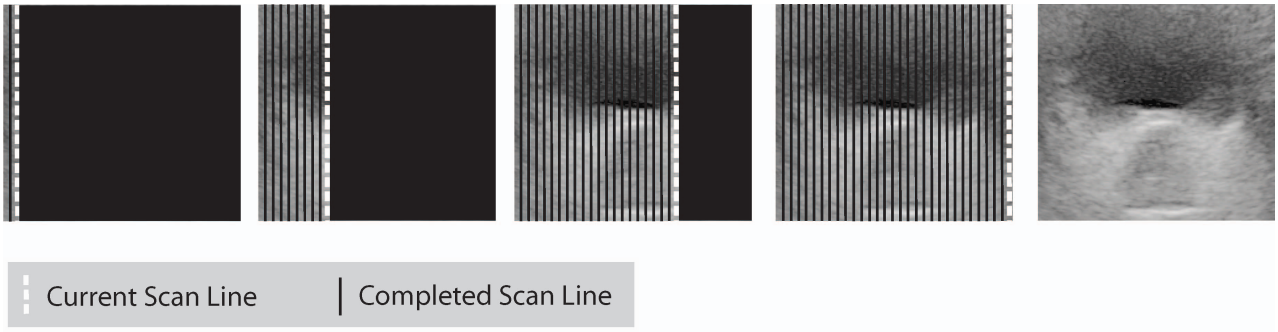

Figure 3.5: Construction of a B-mode image using a series of parallel scan lines.

displaying 256 different shades of gray. Variations in echo amplitude are represented by this gray-scale. Against a black background, echoes with the greatest amplitude appear white, absence of a reflected signal appears black, and echoes with amplitudes in between these two extremes are represented by various shades of gray [25]. In addition, the position of every pixel in the image matrix corresponds to a specific location within the patient. By measuring the position of each echo-producing interface, the amplitude of each potential difference is mapped onto the pixel whose location coincides with the location of the interface that produced the echo [2, 4, 25]. Thus, a gray-scale mapping of echo amplitudes produces 2D US images, or "frames", such as that shown in Figure 3.6.

Figure 3.6: A typical B-mode US image showing the male pelvic anatomy in the transverse plane.

B-mode US scans are composed of several adjacent 2D US frames that are acquired while the transducer is translated over the area being imaged. Multiple US images are acquired at 15 - 60 frames per second. Because echo information is obtained and displayed for a given frame within a fraction of a second, images are considered to show anatomy in real-time [25].

3.3 Instrumentation

Ultrasound images are acquired using an US system. Despite their complexity, all modern US systems consist of six basic components: a transducer, limiter, transmitter, beam former, receiver, and display [2, 4, 25]. These components, and their relationships to one another, are shown in Figure 3.7. In addition, an image tracking system can be added to generate 3D US volumes. In what follows, each component is described in greater detail.

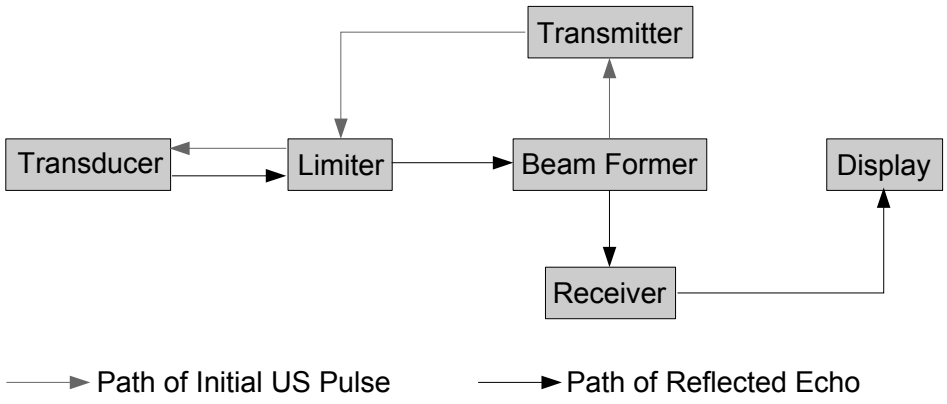

Figure 3.7: Basic components of a modern US system.

3.3.1 Transducer

The transducer is the main functional component of the US system. Figure 3.8 shows a schematic of a simple transducer consisting of a single piezoelectric element, sensor electrodes, backing block, acoustic insulator, matching layer, and plastic housing [4].

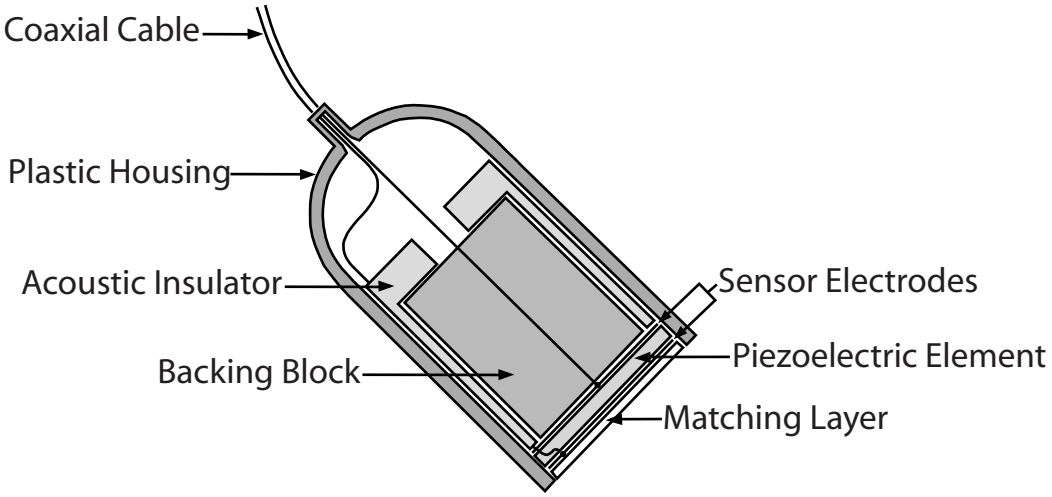

Figure 3.8: An example of a simple transducer with one piezoelectric element [2].

The transducer uses the piezoelectric effect to convert electrical energy into mechanical energy to produce US, and mechanical energy into electrical energy to detect returning echoes [4, 25]. The transducer piezoelectric element is sandwiched between two sensor electrodes, and consists of a well-defined molecular arrangement of electrical dipoles. When the electrodes apply a potential difference across the element, the dipoles become misaligned, creating a net positive charge on one side of the material and a net negative charge on the other. This causes physical deformation of the piezoelectric element - it expands or contracts depending on the polarity of the applied voltage. When the polarity is reversed, the deformation reverses. Applying an alternating potential difference across the element creates repeated compression and rarefaction, causing the transducer to vibrate. By placing the piezoelectric element in contact with the surface of a medium, US waves are transmitted into that medium [4, 25]. The reverse process is also possible. Pressure waves incident on the piezoelectric material cause it to compress and rarefy, creating a potential difference across the piezoelectric element that can be measured using the sensor electrodes [4].

The transducer acoustic insulator and backing block absorb US waves generated

by the piezoelectric element that travel away from the patient. The backing block also supports the piezoelectric element and dampens its vibrations so that each US pulse transmitted into the patient contains 3 cycles of sound [25]. This ensures echoes returning to the transducer from shallow depths within the patient can be detected before the next pulse is sent, and that good image resolution is obtained along the beam axis (see section 3.4.1 for a discussion on image spatial resolution). In addition, the backing block is made out of a material with the same acoustic impedance as the piezoelectric element to eliminate reflections between the two components [2, 4].

The transducer matching layer reduces the dramatic difference in acoustic impedance between the piezoelectric element and patient skin. This is achieved by introducing a layer of material whose acoustic impedance is the average of the two materials. However, even with a matching layer, acoustic coupling gel must still be applied between the transducer and patient skin to eliminate air pockets [2, 4].

Ultrasound pulses produced by a simple transducer can be focused using a curved piezoelectric element or a curved acoustic lens. According to Huygens' Principle, the surface of the piezoelectric element can be considered to consist of an infinite number of US point sources that each transmit spherical US waves into the propagation medium. These waves interact via constructive and destructive interference, producing an US beam with a characteristic beam profile, similar to the one shown in Figure 3.9 [2, 4, 25]. Near the transducer face, the beam is tightly collimated, and referred to as the "near field" or 'Fresnel zone". Beyond this region, the beam begins to diverge, creating the "far field" or "Fraunhofer zone". The near field converges until the boundary between the near and far fields occurs. The distance between the transducer face and the field boundary is called the "focal length". The "focal zone" exists on either side of the field boundary, and extends over the region where the width of the beam is less than twice the width at the field boundary. Ideally, the focal length should be chosen so that the focal zone coincides with the area being

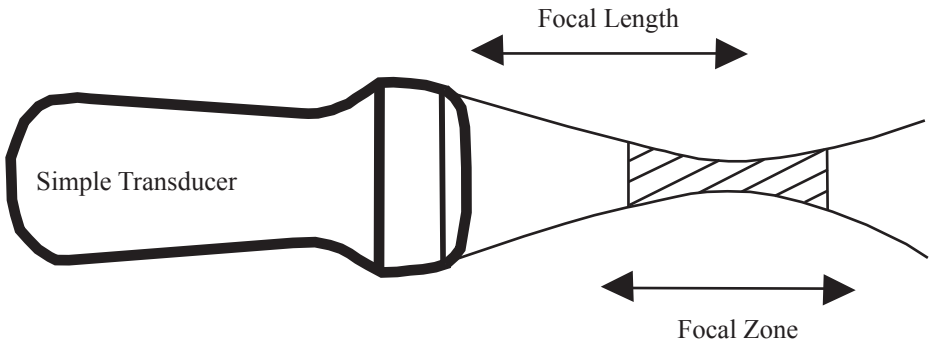

Figure 3.9: A typical US beam profile.

imaged [4, 25]. For abdominal imaging, focal lengths of 12 - 15 *cm* can be considered typical [25].

Most transducers used today consist of a 1D array of rectangular piezoelectric elements and focus the US beam by activating certain elements, or groups of elements, according to a specific sequence. Each piezoelectric element has its own set of electrodes to supply and measure potential differences, and is typically less than 1 *mm* wide and several millimeters tall [4].

Transduce arrays are categorized as either "linear/curvilinear" or "phased", depending on how they produce US beams and the shape of the resulting image field of view (FOV) [4]. Linear and curvilinear array transducers consist of 256 - 512 adjacent elements and are approximately 6 - 8 *cm* wide. Elements arranged in a linear fashion produce an image with a rectangular FOV, while those arranged in a curvilinear fashion produce an image with a trapezoidal FOV [4]. Phased array transducers consist of 64 - 256 elements making them only 3 - 5 *cm* wide. Elements can by arranged in a linear or curvilinear fashion, and produce a sector FOV.

Figure 3.10a demonstrates 2D image acquisition using a linear array transducer. A short duration, alternating potential difference is simultaneously applied to each

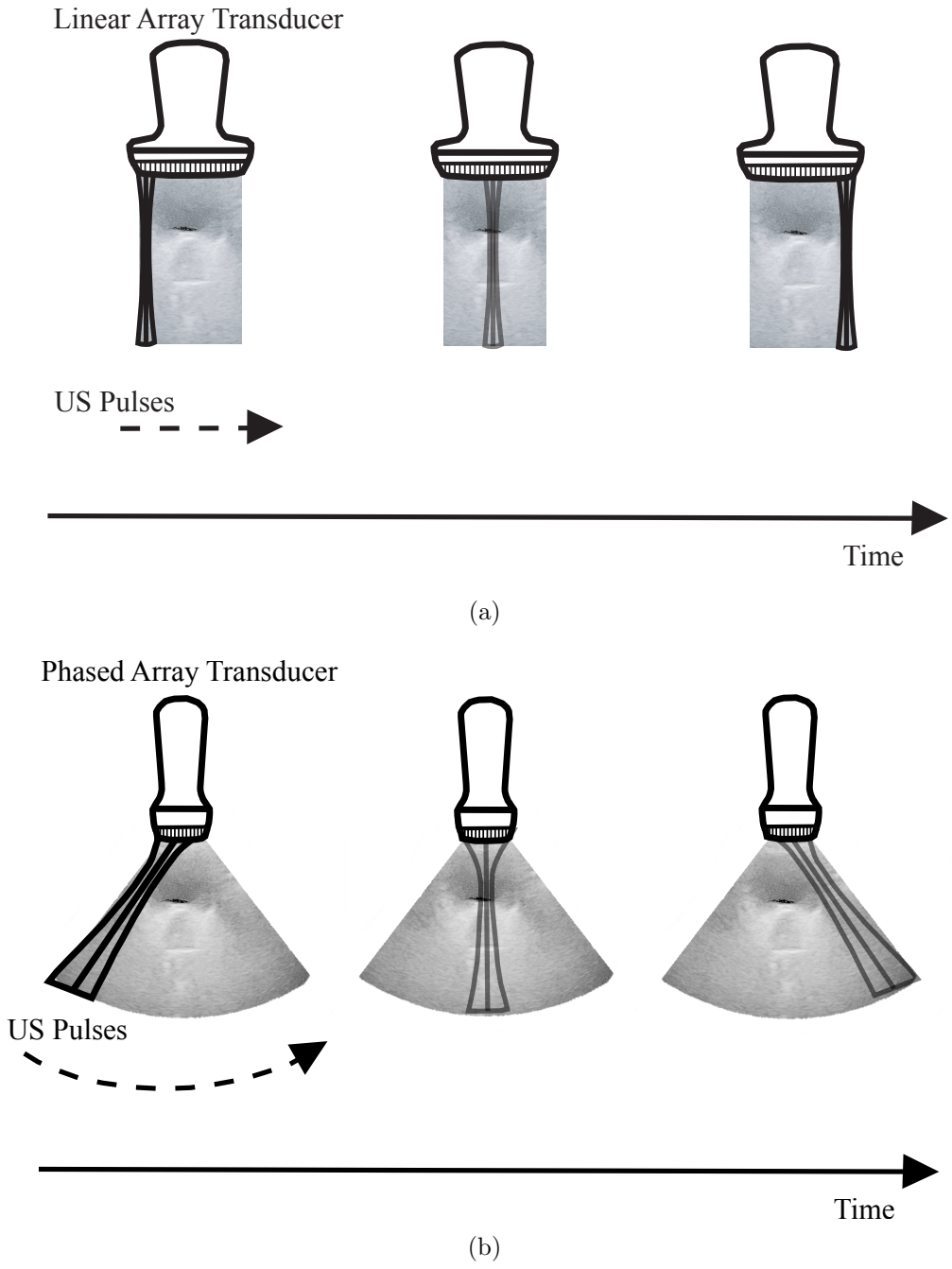

Figure 3.10: Two-dimensional US image acquisition using a) a linear array transducer and b) a phased array transducer.

of $\sim$ 15 - 20 adjacent elements. The resulting US beam produced by the subset of elements has the same beam profile as the simple focused transducer discussed above [2, 4]. Following detection of the echoes produced by this first pulse, another US pulse

is sent by a second group of elements displaced from the first by 1 or 2 elements. This process repeats as the US beam is swept across the area being imaged, and echoes produced by all the pulses combine to form the resulting image [4, 25].

Figure 3.10b illustrates how a 2D image is acquired using a phased array transducer. An US pulse is transmitted through the body at a certain angle by applying a brief alternating potential difference to each element in the array at almost, but not exactly, the same instant. The US pulse travels through the body generating an US beam with the same profile as a simple transducer [2, 4] and produces echoes which return to the elements and are detected. Another US pulse is then transmitted at a slightly different angle by adjusting the delay between the activation of each element. This process repeats and the US beam is swept through various angles of the area being imaged, forming an arch or sector. The echoes produced by all the pulses combine to form the resulting image [4, 25].

3.3.2 Transmitter, Limiter, and Beam Former

During US pulse transmission, the transmitter generates the high voltage pulses ($\sim$ 150 V) used to energize the transducer piezoelectric elements. It is connected to the limiter, which prevents the high voltage signals from reaching the sensitive receiver, but allows passage of the weak potential differences ($\sim$ 2 μV - 1 V) generated by returning echoes.

The beam former delivers electronic delays to the transmitter so that potential differences are applied to certain elements, or groups of elements, according to a specific sequence. The delay sequence controls focusing of the US beam at specific depths from the surface for both linear/curvilinear and phased array transducers. In addition to beam focusing, these delays are also used to steer the US beam for phased array transducers [4, 25]. The beam former is also responsible for recording the amplitude of each potential difference generated across the transducer by a returning echo and the position of the interface that produced the echo [25, 26].

3.3.3 Receiver

The receiver accepts information about echo amplitude and the location of echo production from the beam former, and prepares it for display. This preparation involves optimizing echo signals and converting echo information into pixel data.

Echo information must be optimized to account for attenuation of the US signal as it travels through the body. This phenomenon was described in section 3.1.2. The amplitude of each echo that returns to the transducer is very small compared to the amplitude of the initial US pulse, and the amplitudes of the strongest and weakest echoes can vary by factors as much as 10^{12}. While the receiver is capable of reading such a large range of voltages, the display can only assign $\sim$ 250 shades of gray to differing echo amplitudes. To compensate, the receiver amplifies each echo and compresses the range of echo amplitudes. In addition, echo information is filtered to remove unwanted noise by preventing echoes with amplitudes below a specific threshold from being displayed [4, 25]. This threshold, or "noise rejection level", as well as the degree of echo amplification, can be controlled by the US system user.

Following optimization, echo information is converted into pixel data and displayed as described in section 3.2.2.

3.3.4 Image Tracking System

Image tracking systems are used to generate 3D US volumes from 2D US scanning. As the transducer is translated over the area of interest, the image tracking system measures and records the position and orientation of each 2D US frame acquired. Each frame is then placed in its correct position within a 3D voxel-based volume, as illustrated in Figure 3.11. If data for a given voxel is missing, the information is "filled in" by interpolating between appropriate frames. By accounting for this missing information, 2D images can be constructed in any of three mutually perpendicular planes [3, 28–30] using a virtual ray tracing process similar to that described in section

2.1.2 for DRRs [28].

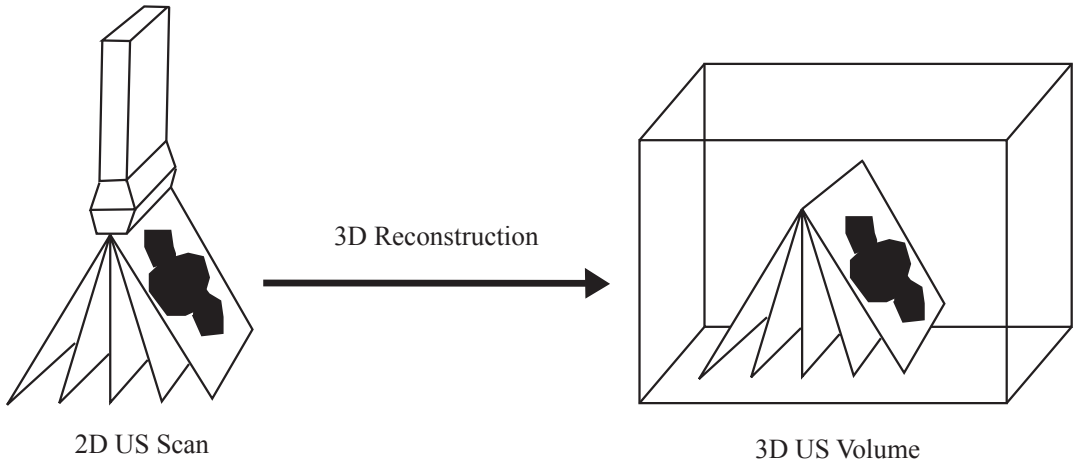

Figure 3.11: Acquisition of a 3D US volume from 2D US scanning [3].

Two types of tracking systems are of particular note for RT use [3]: camera based systems and mechanical systems. Using a camera based system, an attachment on the transducer sends information to a camera that tracks and records the position and orientation of the transducer, and by extension, each 2D US frame. With a mechanical system, the transducer is attached to a robotic arm that displaces the transducer over the area being imaged at regular, predefined intervals. The arm is equipped with position sensors that measure and record the position and orientation of the transducer, and therefore, each 2D US image [3, 28–30].

3.4 Image Quality

Ultrasound image quality is vitally important when interpreting B-mode US images, and is determined by image spatial resolution, image contrast resolution and noise, and the presence or absence of image artifacts [4]. Each of these factors are described in further detail below.

3.4.1 Spatial Resolution

Spatial resolution is a measure of the ability to distinguish two closely spaced objects as distinct structures. In US, spatial resolution is separated into three components: axial, lateral, and elevational resolution (slice thickness), as illustrated in Figure 3.12 [4, 25].

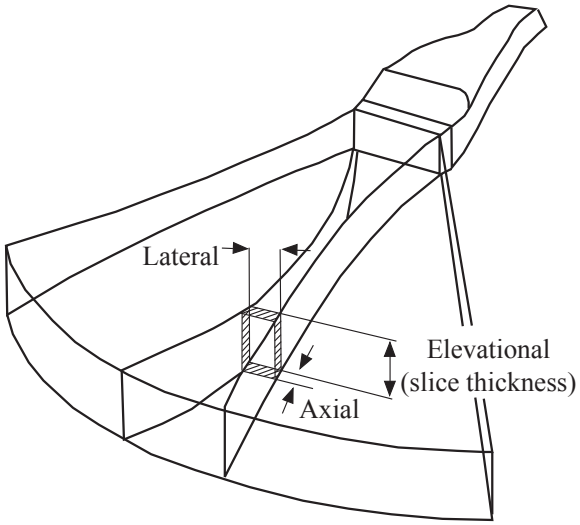

Figure 3.12: US image spatial resolution: axial, lateral, and elevational resolution (slice thickness). [4].

Axial resolution indicates the degree of discernability along the direction of US beam propagation, and is defined by Equation 3.5, where λ and n are the wavelength and number of cycles per pulse of US respectively [3, 4].

$$Axial\ Resolution = \frac{n\lambda}{2} \tag{3.5}$$

Good axial resolution is achieved by adjusting λ and n so that echoes produced by reflectors situated at different depths along the same beam path do not overlap before they return to the transducer. As mentioned in section 3.1.1, most medical US imaging systems transmit 3 cycles of sound per pulse, so typically, only the US

beam frequency is adjusted to obtain the best axial resolution [4, 25]. For abdominal imaging, the frequency of the US beam is typically 3.5 - 5.0 MHz [4, 25], which provides an axial resolution of approximately 0.5 - 0.7 mm.

Lateral resolution defines the visibility of structures perpendicular to the direction of US signal propagation and in the plane of the image. It is determined by the width of the US beam, and is therefore dependent on depth and transducer design. The best lateral resolution is achieved in the narrowest region of the beam, or focal zone [4, 25], discussed in section 3.3.1. For medical applications, lateral resolution can be of the order of a few millimeters for a focused beam [2].

Elevational resolution, or slice thickness, indicates the discernability of structures perpendicular to the US beam axis and the image plane. It depends on the height of the transducer piezoelectric elements, which are typically of the order of 1 cm tall [2], and generally cannot be controlled by the user [4, 25].

3.4.2 Contrast Resolution and Noise

Contrast resolution refers to the ability to discern two structures with different acoustic impedances as distinct objects based on gray-scale differences. It is determined by the ability of the US system to detect and display weak echoes, and depends on the image contrast-to-noise ratio [4]. Image noise is produced by a number of different sources, including scattered US signals (discussed in section 3.1.2), US system electronics - particularly receiver echo amplifiers, malfunctioning system components such as dead or poorly functioning transducer elements, and environmental sources like electrical power fluctuations [4]. Image noise, and therefore, the contrast-to-noise ratio, can be controlled by the user (to a certain extent) to provide optimal contrast resolution by adjusting the US system noise rejection level discussed in section 3.3.3 [2, 4].

3.4.3 Image Artifacts

Image artifacts are errors that obscure information about the anatomy being imaged and can be caused by several different mechanisms [4, 25]. Depending on the clinical application, some image artifacts are more problematic than others.

Many artifacts, including reverberation, refraction, and side and grating lobe artifacts, are structures that appear in the image that are not actually present in the anatomy. Reverberation artifacts occur when an US signal reflects off two closely spaced, strong reflectors, multiple times, producing a series of echoes. Reverberation echoes are often caused by refections between the transducer and metallic objects, or air or liquid pockets, and appear as multiple, equally spaced white lines with decreasing intensity in the image [4, 25]. As a result, the echo-producing structure is mapped multiple times to the image, making any assessment about the location of the structure very subjective. These types of artifacts can cause problems when US is used to define the position of an organ during image guided radiation therapy or organ biopsy.

Refraction of the US pulse causes part of the signal to travel through the medium at a different angle than that of the incident beam, as described in section 3.1.2. This in turn causes structures outside the main US beam to reflect echoes that return to the transducer and appear in the image [4, 25]. A similar phenomenon occurs as a result of side and grating lobes. Side lobes are US waves that propagate outside the main US beam, and result from expansion and contraction of transducer elements perpendicular to main beam propagation. Echoes that return from reflectors exposed to side lobes appear in the image and misrepresent the anatomy. Similar artifacts are caused by grating lobes, US waves that propagate at a large angle from the main beam due to the large number of piezoelectric elements in transducer arrays [4, 25]. These types of artifacts can cause problems in screening for disease and can lead to incorrect diagnoses.

Artifacts can also alter the size, shape, or position of structures, or remove information from an image, as with shadowing artifacts, which result from attenuation of reflected echoes by superficial structures in the beam path. An echo that would otherwise appear very intense (white line) shows up with little intensity or none at all [4, 25] in the resulting image. Similar to refraction and side and grating lobe artifacts, shadowing artifacts can cause misdiagnoses.

Other artifacts result from operator errors. Inappropriate choice of instrument variables (i.e. noise rejection level and the amount of echo amplification) can prevent valuable information from being displayed. Poor scanning technique, including inappropriate transducer angle, speed of transducer translation in 3D imaging, or lack of complete contact between the transducer and the skin/coupling gel can also cause unwanted image artifacts.

Chapter 4

Methods and Materials

This chapter discusses the general methods and materials used throughout this work. Detailed descriptions of the procedures and equipment used to collect FM and US measured couch shifts are given in sections 4.1 and 4.2 respectively. Section 4.3 provides details about the statistical procedures used to analyze couch shift data. Procedural details specific to each study are given in chapters 5 - 7.

4.1 Fiducial Marker Prostate Localization

Figure 4.1 illustrates the steps used to collect FM measured couch shifts. These procedures were performed during part of a larger study that investigated several aspects of FM prostate localization. Fiducial markers were inserted into the prostate gland. This was followed by CT simulation of the pelvic area and construction of anterior and left lateral DRRs. Fiducial marker matching templates were created from the DRRs and EPIs were acquired. Fiducial marker matching was then performed and any necessary couch shifts made.

The following sections provide details of these procedures as they apply to this work. Fiducial marker implantation and CT simulation are outlined in sections 4.1.1 and 4.1.2 respectively. Procedures for DRR construction and FM template creation are discussed in section 4.1.3. Further procedural details for EPI acquisition and FM matching are described in sections 4.1.4 and 4.1.5 respectively.

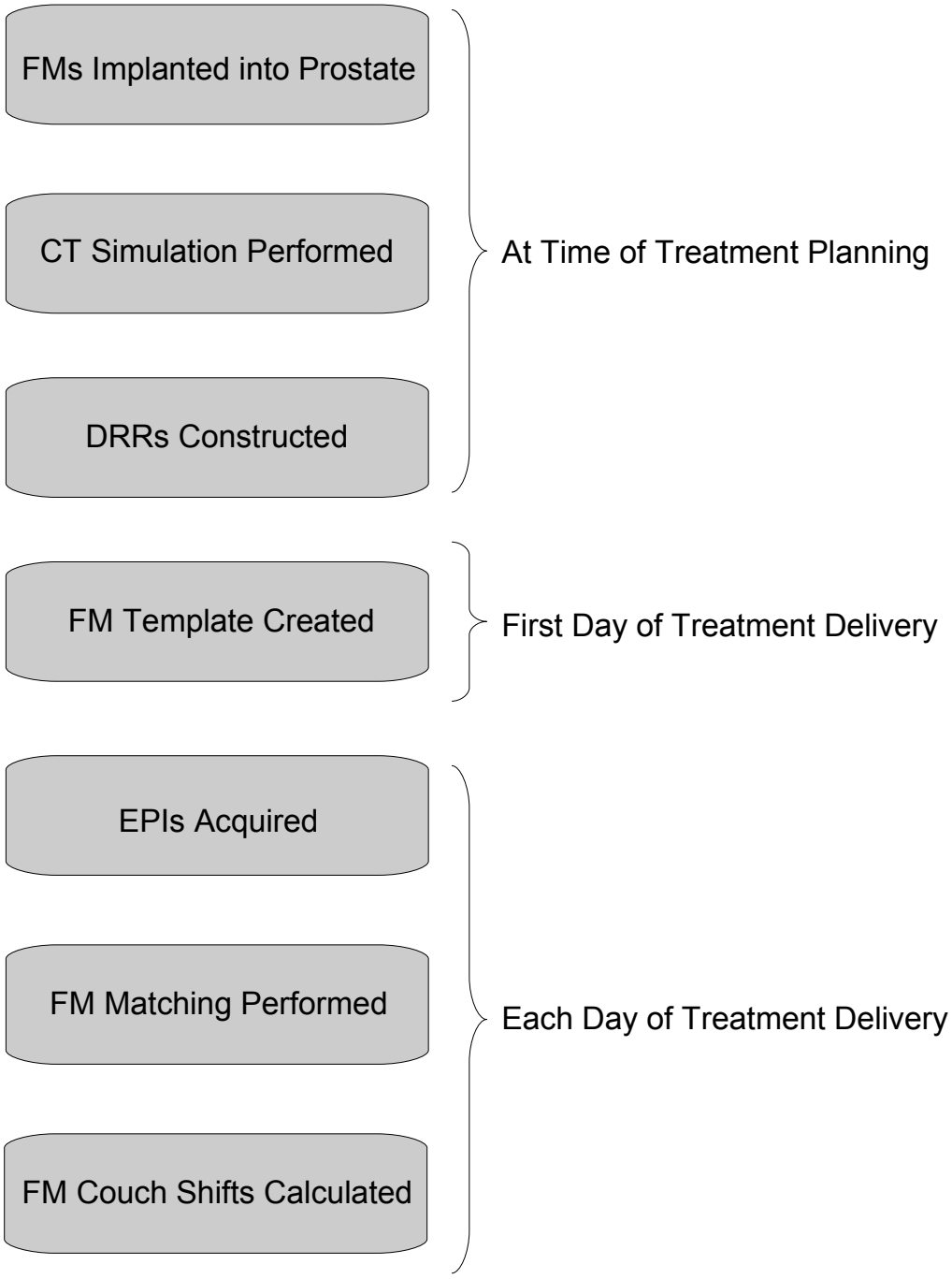

Figure 4.1: Steps involved in collecting FM couch shifts: FMs were implanted into the prostate, CT simulation was performed, DRRs were constructed, FM templates were created, EPIs were acquired, FM matching was performed, and FM couch shifts were calculated.

4.1.1 Fiducial Marker Implantation

All FMs (Best Medical International Inc., Springfield, VA) used in this study were cylindrical gold seeds, 2 mm in diameter and 5 mm in length. Figure 4.2 shows a FM of the type used.

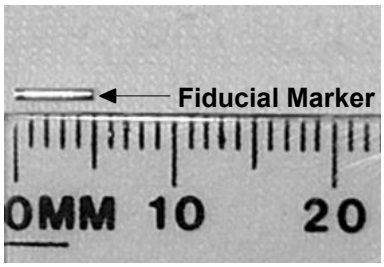

Figure 4.2: A FM of the type and brand used in this study.

Three FMs were implanted into the prostate at the right base, right apex, and left midline before CT simulation and treatment planning, as shown in Figure 4.3. The procedure was performed under TRUS guidance by a trained radiologist. The position of FMs within the prostate is known to be very stable over time [14, 16, 31], however as a precaution, a second CT scan was performed mid-way through treatment (i.e. after $\sim 15-20$ treatment fractions were complete) to check for FM migration.

4.1.2 Computed Tomography Simulation

At CT simulation, patients were positioned on the CT couch face up, with head toward the CT gantry. Their legs were immobilized using a special foam device placed under their feet. Instructions were given for patients to arrive with a comfortably full bladder, and urethrograms (injection of radiopaque die into the urethra) were performed to enhance bladder visibility on CT images, but no bowel preparation was employed. External radiopaque markers were affixed to patients where CT lasers intersected their skin, and instructions were given to remain still throughout the scanning procedure. When image acquisition was complete, the radiopaque markers were replaced with permanent tattoos to be used for patient set-up at each day of treatment.

All patients were CT scanned from the base of the spine (S1 vertebrae of the sacrum) to 7 cm below the tip of the urethra using 2 mm thick slices, on a HiSpeed

FX/i CT simulator (GE Medical Systems, Milwaukee, WI). Transverse images were acquired and reconstructed as described in section 2.1.1.

4.1.3 Digitally Reconstructed Radiograph and Fiducial Marker Template Creation

Following CT simulation, a trained radiation therapist contoured the FMs and pelvic anatomy on transverse CT image slices. A trained radiation oncologist then defined the target and normal tissue volumes as described in section 2.1.2. Contoured CT slices with target and normal tissue volumes were used to create a radiotherapy treatment plan on an Eclipse treatment planning system (Varian Medical Systems, Palo Alto, CA). The treatment plan and FM contoured CT slices were then used to construct DRRs as outline in section 2.1.2. Digitally reconstructed radiographs showed anterior and left lateral views of the pelvic bony anatomy including FM contours, and were transferred to the treatment unit, along with the radiotherapy treatment plan.

On the first day of treatment, anterior and left lateral FM templates were created using the DRRs constructed at treatment planning. Each template consisted of FM contours, the planned radiation field aperture, and outlines of the pelvic bony anatomy. Figure 4.3 shows how an anterior FM template was created. Using Varis treatment software (Varian Medical Systems, Palo Alto, CA), a trained radiation therapist opened the DRR with FM contours at the treatment unit console and applied the planned radiation field aperture. They then outlined the pelvic bony anatomy to aid in placing the template during FM matching and saved the resulting template for use at each day of treatment. The same procedure was used to create left lateral templates.

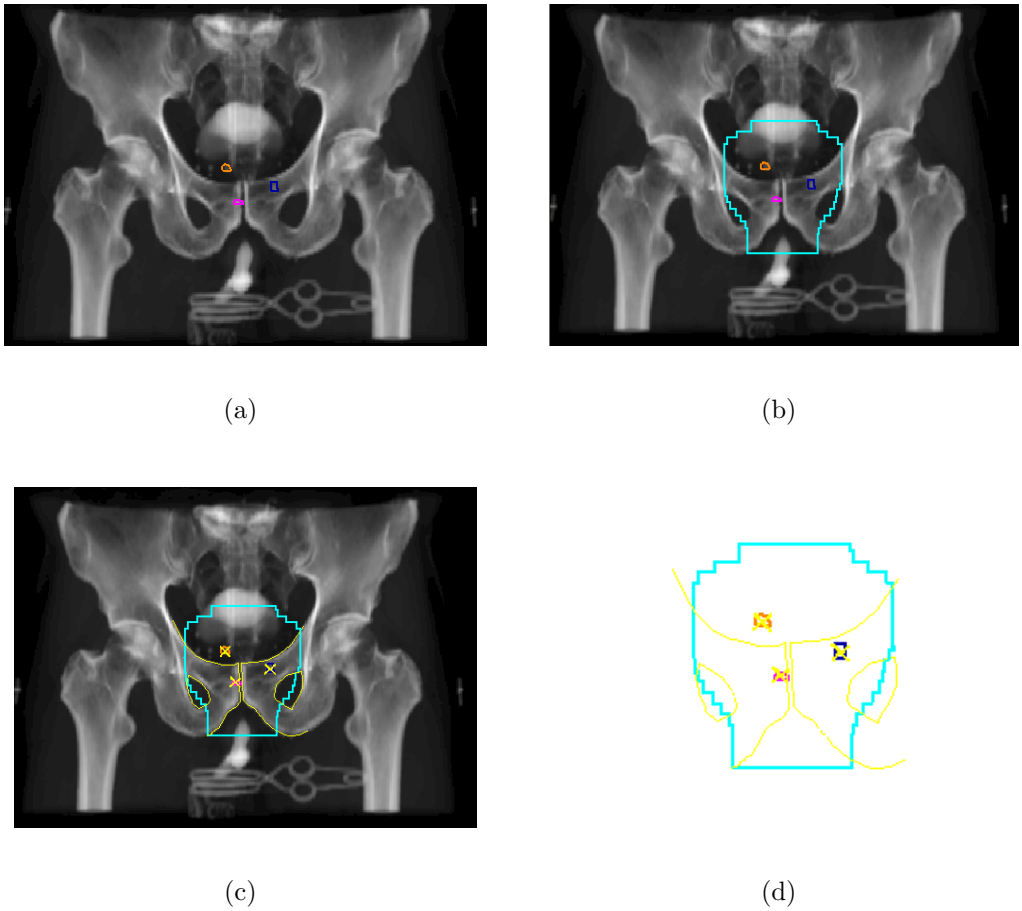

(a) (b)

(c) (d)

Figure 4.3: Anterior FM template creation: a) the anterior DRR with FM contours was opened on the treatment unit console, b) the planned radiation field aperture was overlaid onto the DRR, and c) pelvic bony anatomy was outlined to produce the anterior FM matching template (enlarged for clarity) shown in d).

4.1.4 Electronic Portal Image Acquisition

At the treatment unit (Clinac 21EX Linear Accelerator, Varian Medical Systems), patients were set-up as at CT simulation by aligning their tattoos with the treatment room lasers. Electronic portal images were acquired of the anterior and left lateral treatment fields using an amorphous silicon EPID as described in section 2.1.3. Doses delivered during EPI acquisition were accounted for in the treatment plan.

4.1.5 Fiducial Marker Matching and Patient Treatment

After anterior and left lateral EPIs were acquired, FM matching was performed by a trained radiation therapist. Figure 4.4 shows how anterior FM matching proceeded. The EPI and DRR were viewed side-by-side on the Varis software. The treatment field edge was automatically detected on the EPI (shown in peach) and the FM template overlaid. The contour of one FM in the FM template was then aligned with the corresponding FM in the EPI. When this was done, the field aperture shown in the EPI did not necessarily line up with the field aperture shown in the FM template. Any difference between the locations of the field apertures on the template and EPI gave the displacement of that particular FM between time of treatment planning and that day of treatment delivery. The process was repeated for the other FMs, and the displacements of all three were averaged to give the displacement of the prostate gland.

Anterior FM matching provided prostate displacements in the right-left and superior-inferior directions. The process was repeated using left-lateral EPIs to determine displacements in the anterior-posterior direction and an additional measure of displacement in the superior-inferior direction. Since anterior EPIs require x-rays to travel through less tissue than left-lateral EPIs, they provide a clearer image for FM matching. Thus, displacements in the superior-inferior direction measured using anterior FM matching were used for analysis.

Displacements were entered into an in-house database designed using Visual Basic (Microsoft Corporation, Redmond, WA). If displacements exceeded 3 mm in any direction, a predefined clinical tolerance for prostate cancer patients, the database instructed the radiation therapist to perform a couch shift equal to the displacement but in the opposite direction.

After FM matching, US measurements were acquired (as described below, section 4.2), and any required patients realignments were performed using FM measurements.

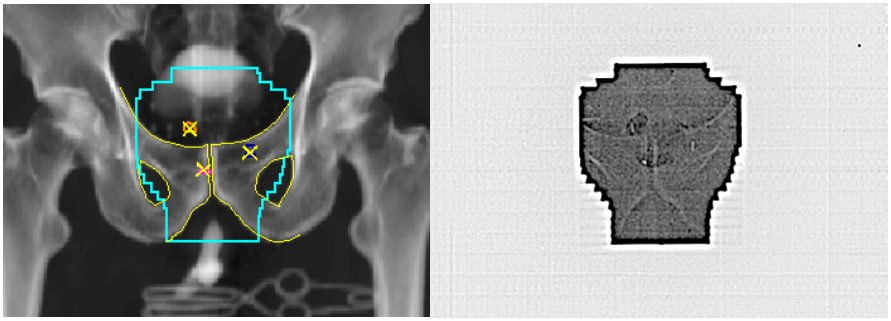

(a)

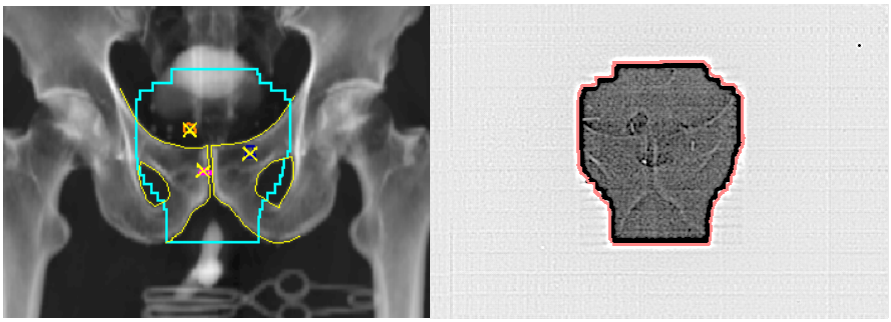

(b)

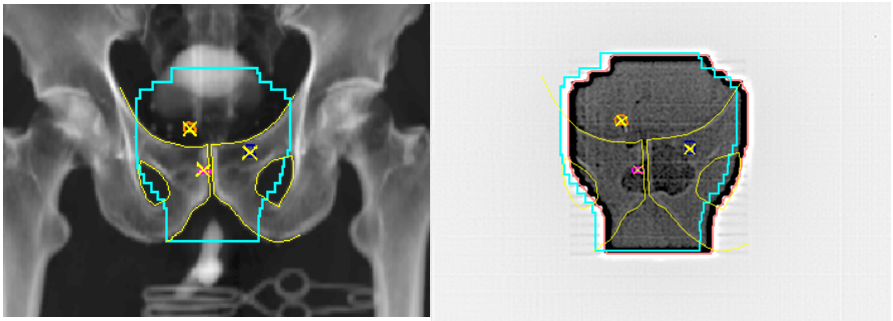

(c)

Figure 4.4: FM matching using anterior DRR and EPI: a) the DRR and EPI were viewed side by side, note the visible FMs in the EPI image, b) the treatment field edge was detected on the EPI and shown in peach, c) the FM template was overlaid on the EPI and one FM at a time was matched.

Treatment was then administered. For most patients, doses between 70 - 74 Gy were delivered using five 18 MV photon beams over the course of 38 fractions. Following completion of $\sim 15 - 20$ treatment fractions, a check for FM migration was carried out as described in section 4.1.1.

4.2 Ultrasound Prostate Localization using the Restitu System

The Restitu System is an intra-modality US image guidance system used to reposition the prostate into the radiation beam at each day of treatment. It includes two US stations, one located in the CT simulator room and one in the LINAC treatment room, that are connected through a workstation/server located at an independent location on site [32].

Each US station consists of a curved, phased array US transducer (Ultrasonix Medical Corporation, Richmond, BC) operated in B-mode and equipped with infrared (IR) emitters, a ceiling mounted IR tracking camera (Northern Digital Incorporated, Waterloo, ON) and a ceiling mounted computer console. Figure 4.5 shows an example of a Restitu US station used in this study.

As the US transducer is fanned over the pelvic area, the tracking camera records the position of the transducer with 6 degrees of freedom. Two-dimensional US frames generated by the transducer are matched to transducer position and orientation information and used to reconstruct a 3D US volume of the scanned area [32]. The US stations are calibrated to match the coordinate systems of the CT and treatment rooms respectively such that real-time tracking of transducer position provides 2D US images correctly positioned within each 3D coordinate frame. Quality assurance checks confirm system calibration each day of use.

Figure 4.6 provides an overview of how couch shifts are measured using the Restitu System. A planning US scan is acquired at CT simulation and the resulting US vol-

Figure 4.5: A Restitu US station: a) US probe with IR emitters, b) IR tracking camera, and c) Restitu software console.

ume is transferred to a workstation. There, the CT and US image sets are fused to ensure accurate patient positioning, and a contour of the prostate is generated, called the positioning reference volume (PRV). The position of this contour represents the position of the prostate at time of treatment planning, and is saved on the workstation for future use. At each day of treatment, patients receive an additional US scan, and the positioning guidance volume (PGV) is defined using either assisted or manual prostate segmentation. The position of the PGV represents the position of the prostate for that day of treatment. The PRV is retrieved from the workstation and its position is compared to that of the PGV. Any couch shifts required to realign the prostate into the planned treatment position are reported to the radiation therapist.

Details of the individual components and procedures used in this work to measure couch shifts with the Restitu System are described below. Section 4.2.1 details use of the planning US station at CT simulation. Section 4.2.2 discusses how the Restitu workstation was used, and section 4.2.3 describes use of the treatment US station at each day of radiation delivery.

4.2.1 Planning Ultrasound Station

Planning US scans were performed by one of 5 trained radiation therapists immediately after CT scans. Patients remained in the same position as confirmed by the intersection of CT lasers with external radiopaque markers. A 3D US volume was constructed from 2D US frames as described above and transferred to the Restitu workstation.

4.2.2 Restitu Workstation

For this work, both CT and US image sets were transferred to the Restitu workstation immediately after image acquisition. The coordinates of CT image slices were matched (or registered) with those of the US image frames. In this way, both images could be viewed simultaneously, overlaid on top of one another. This provided

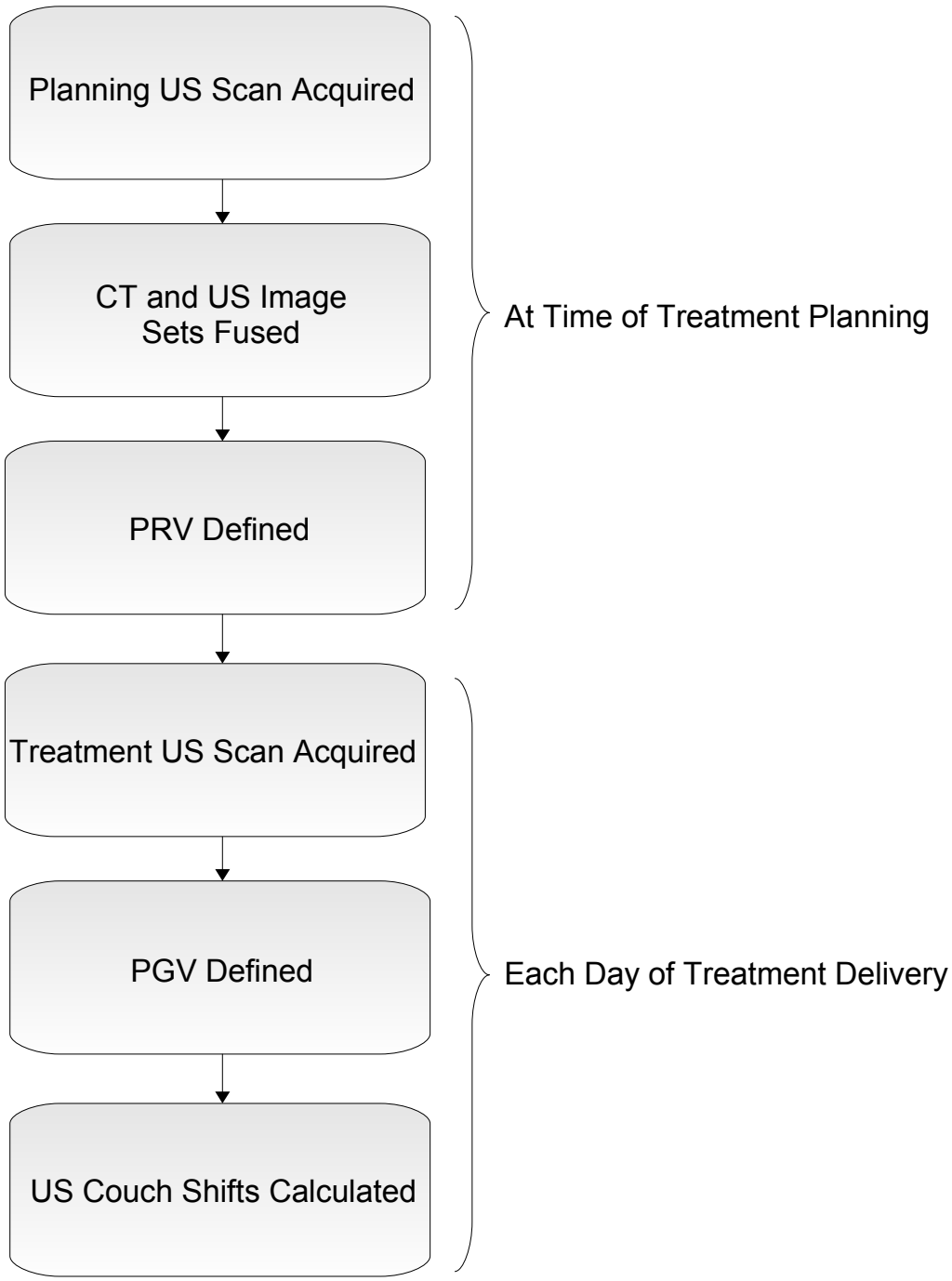

Figure 4.6: Procedure for measuring couch shifts using the Restitu System: the planning US scan is acquired, CT and US image sets are fused, the PRV is defined, a treatment US scan is acquired, the PGV is defined (using assisted or manual segmentation), and US couch shifts are calculated.

a visual check that the position of anatomical structures in each image coincided, and patient positioning was consistent between CT and US scans. For all patients included in this study, the image registration was very good, as structures in both the CT and US image sets coincided.

The workstation was then used to create the PRV. The prostate was contoured on the reconstructed planning US volume and its position with respect to the CT simulator room coordinates was determined. This contour defined the PRV and indicated prostate position at time of planning. The PRV was approved by the study's leading radiation oncologist and placed on the Restitu server for access at the treatment unit.

4.2.3 Treatment Ultrasound Station

Treatment US scans were acquired immediately after EPI acquisition by a trained radiation therapist, with the patient remaining in the treatment position. The prostate was contoured using assisted segmentation, following procedures defined by the system manufacturer. Figure 4.7 illustrates this process.

The radiation therapist located the transverse US frame where the prostate appeared largest and the prostate borders appeared clearest. They placed four "hint points" symmetrically on the anterior, lateral, and posterior prostate borders. Using these points, the shape of the PRV, and characteristics of prostate gland anatomy as guides, the US system automatically generated the PGV using a 3D edge-recognition and surface-mapping algorithm [33, 34]. Couch shifts required to relocate the prostate to its planned position were then automatically calculated using a weighted surface matching algorithm. This algorithm compares the location of the PRV to the location of the PGV. If a portion of the surface of the PGV coincides with the edge of the PRV, the location of that surface is weighted heavily. If, on the other hand, a portion of the PGV does not coincide with the edge of the PRV, the location of that portion is given zero weighting. The displacement required to minimize the distance

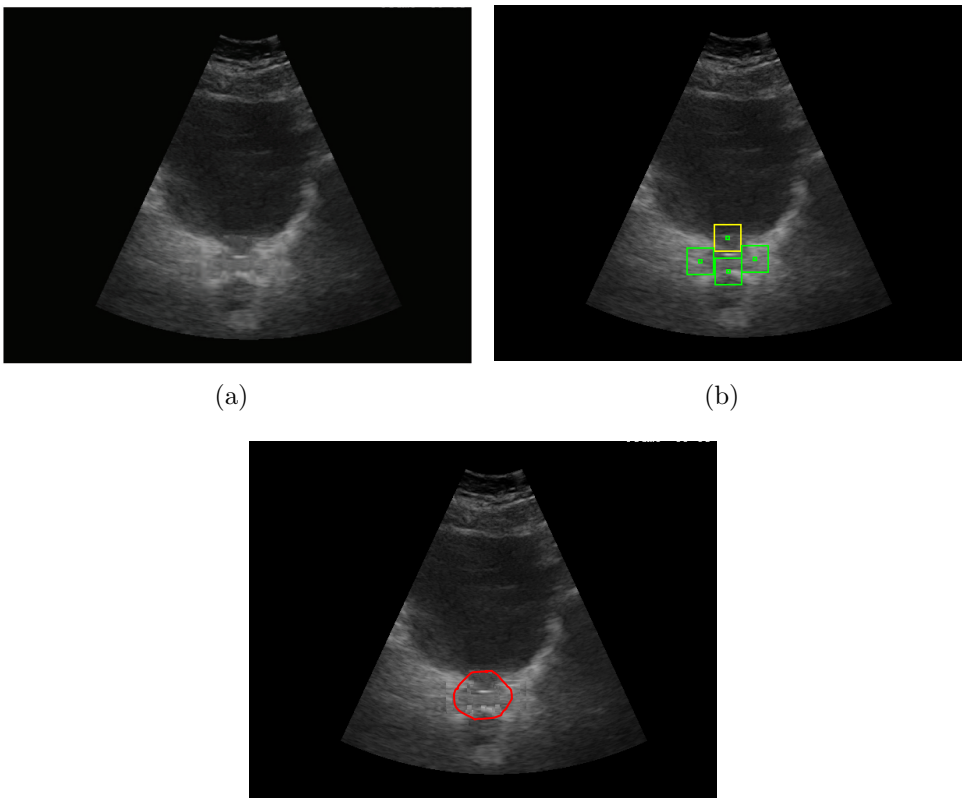

(a) (b)

(c)

Figure 4.7: Example showing how assisted segmentation couch shifts were determined: a) the transverse US frame where the prostate appeared largest and the prostate boundaries appeared clearest was located, b) hint points were placed on the prostate borders, and c) the PGV was generated and compared to the PRV to determine the required couch shifts.

between the PRV and PGV weighted surfaces, or couch shift, is then computed. Patients were not moved using the Restitu System, but data was saved on the US workstation/server.

Alternatively, the prostate can be contoured using manual segmentation. This technique was not used at the treatment unit for this work. Instead, a retrospective analysis was carried out on the Restitu workstation by a single user (HJ) using software that exactly simulated the US image guidance process in the treatment room. The user received one-on-one training from an expert from Resonant Medical prior to this data collection.

Figure 4.8 uses sagittal US images to illustrate the procedure used to determine

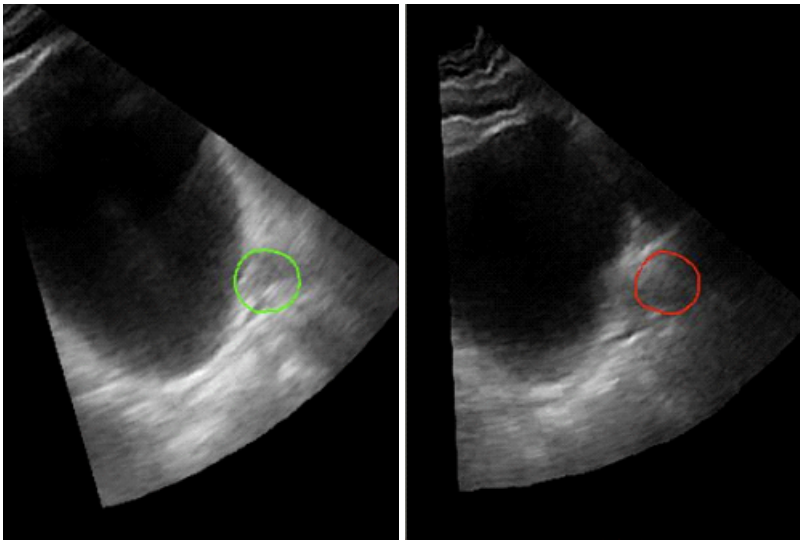

(a)

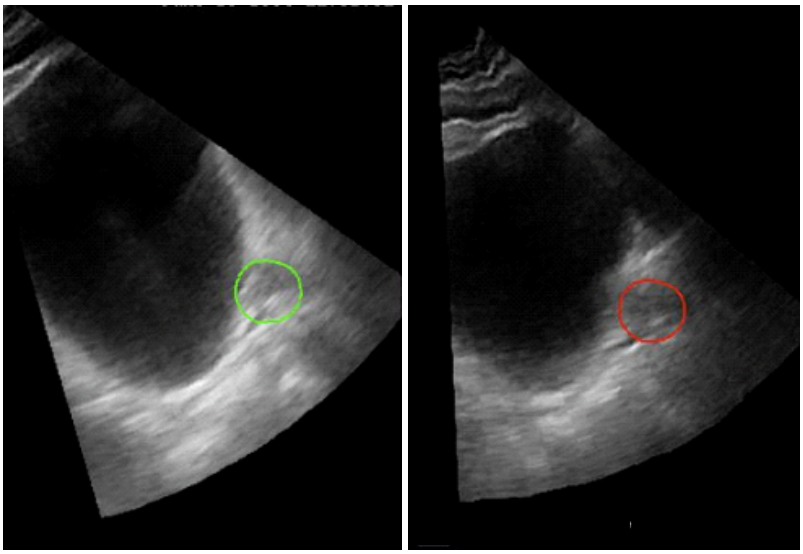

(b)

Figure 4.8: Example showing how couch shifts were calculated using manual segmentation: a) the planning US scan shown on the left, with PRV in green, was viewed beside the treatment US scan shown on the right, with PGV in red. b) The position of the PGV was manually adjusted over the treatment image until its position with respect to the prostate visually match that of the PRV in the planning image. Difference between the positions of the two contours were then computed to determine required couch shifts.

manual segmentation couch shifts using the workstation software. Similar to assisted segmentation, the transverse US frame in which the prostate appeared largest and the prostate borders were clearest was selected. A copy of the PRV generated at planning was then manually positioned on this frame, *becoming* the PGV. Through iterative examination of transverse and sagittal US frames, the position of the PGV in the treatment frame (shown in red in Figure 4.8) was fine-tuned to match that of the PRV in the original planning US frame (shown in green in Figure 4.8). When satisfied with the position of the PGV, any couch shifts required to realign the prostate to its planned position were automatically calculated by the US system. Since in this case the PGV is a copy of the PRV, no surface matching algorithm was required.

4.3 Statistical Analysis

This section describes the statistical techniques used throughout this work. As mentioned in section 2.2, couch shift measurements are 3D vectors, consisting of three mutually perpendicular components: an anterior-posterior (AP) component, right-left (RL) component, and superior-inferior (SI) component. As such, three independent couch shift distributions were constructed - one distribution for each couch shift component - by pooling measurements from all patients. Since the analyzes described below were applied to each component distribution separately, in what follows, scaler notation will be used.

Descriptive statistics and 95 % limits of agreement (LOA) are outlined in sections 4.3.1 and 4.3.2 respectively. Section 4.3.3 explains the F-Test used to compare US and FM couch shift distribution variances, and section 4.3.4 details repeatability coefficients calculated using analysis of variance.

4.3.1 Descriptive Statistics

Descriptive statistics were used to describe, compare, and summarize couch shift distributions. Both histograms and numerical statistics were employed.

Couch shift distributions were illustrated using relative frequency histograms. These plots graphically demonstrate the distribution of values in a data set. The horizontal measurement axis is divided into bins of equal width, and a vertical bar is drawn over each bin to represent the relative frequency for that bin. Relative frequency is computed using Equation 4.1 [35].

$$\text{Relative Frequency} = \frac{\text{number of observations in a bin}}{\text{total number of observations}} \times 100\% \tag{4.1}$$

Further information was extracted from the data by computing numerical statistics. The arithmetic mean, or mean, and median were computed to determine the central location of each distribution. The mean, $\overline{x}$, provides the best estimate of a typical observation [36], and is found by taking the sum of the values, x_i, and dividing by their total number, n, as in Equation 4.2.

$$\overline{x} = \frac{\sum_{i=1}^{n} x_i}{n} \tag{4.2}$$

The median, $\tilde{x}$, is calculated by ordering observations from smallest to largest, and finding the middle value using Equation 4.3, where n is the total number of observations [35].

$$\tilde{x} = \begin{cases} (\frac{n+1}{2})^{th} \text{ ordered value} & \text{if n is odd} \\ \text{average of } (\frac{n}{2})^{th} \text{ and } (\frac{n}{2}+1)^{th} \text{ ordered values} & \text{if n is even} \end{cases} \tag{4.3}$$

The variability of each distribution was measured by the range and standard deviation. The range, given by Equation 4.4, is defined by the minimum, x_{Min}, and maximum, x_{Max}, values, and indicates the extent of the data and the most extreme values present [36].

$$Range = (x_{Min},\ x_{Max}) \tag{4.4}$$

The standard deviation, s, provides an estimate of the spread in values, x_i, about the mean, $\overline{x}$, and is computed using Equation 4.5.

$$s = \sqrt{\frac{\sum_{i=1}^{n}(x_i - \overline{x})^2}{n-1}} \tag{4.5}$$

The standard deviation is also used to calculate a 95 % confidence interval for the mean, $CI(\overline{x})$. The $CI(\overline{x})$ provides an estimate of the precision associated with the mean, and is based on the standard error on the mean, SE, and the t-critical value for the given distribution. The standard error on the mean is determined as:

$$SE = \frac{s}{\sqrt{n}} \tag{4.6}$$

where n is the total number of measurements, and s is the standard deviation [35].

A t-critical value, $t_{\frac{\alpha}{2},\ n-1}$, is derived from a student's t-distribution with the same number of degrees of freedom, $n-1$, as the given distribution of measurements. It is the value on the measurement axis of the corresponding t-distribution curve for which $\frac{\alpha}{2}$ of the area under the curve lies to its right in the upper-tail, and to its left in the lower tail [35]. For a 95 % confidence interval, 2.5 % of the area under the curve lies on either side of the t-critical value. Summary tables of t-critical values are available, and for this work, were determined using Matlab's tables (The MathWorks Inc., Natick, MA).

Equation 4.7 defines $CI(\overline{x})$, where $\overline{x} + (t_{0.025,\ n-1} \times SE)$ is the upper confidence limit and $\overline{x} - (t_{0.025,\ n-1} \times SE)$ is the lower confidence limit [35, 37].

$$CI(\overline{x}) = \overline{x} \pm (t_{0.025,\ n-1} \times SE) \tag{4.7}$$

4.3.2 Ninety-Five Percent Limits of Agreement

To compare US and FM data, several additional statistical methods were employed. To visually assess the relationship between US and FM paired measurements, scatter plots were constructed [36]. Scatter plots display paired values measured using two different methods plotted against one another and the line of equality, $y = x$. If two methods of measurement return values that are in perfect agreement, all points in the plot lie along the line of equality.

Further quantitative analysis was based on the differences, d, between paired FM, x_{FM}, and US, x_{US}, measured couch shifts:

$$d = x_{FM} - x_{US} \tag{4.8}$$

These were used to calculate the LOA using Equation 4.9, where $\overline{d}$ is the mean difference and s_d is the standard deviation of differences. The LOA are similar to a 95 % confidence interval, but use the distribution standard deviation instead of the standard error on the mean. In this way, the LOA define the range over which 95 % of differences between two methods of measurement lie [38, 39].

$$LOA = \overline{d} \pm (1.96 \times s_d) \tag{4.9}$$

The utility of the LOA analysis is in providing a basis for a quantitative clinical decision on the agreement of two independent methods of performing a given task. Provided the LOA are less than or equal to a clinically significant tolerance, one method can be used interchangeably with the other [38, 39].

The LOA are determined based on two assumptions [40]. First, differences must follow an approximately normal distribution. This assumption is valid according to the central limit theorem, as each difference data set consists of the sum of two

independent measurement distributions, and can be verified using relative frequency histograms [36]. Second, the mean and standard deviation of differences must remain reasonably constant throughout the range of measurements. This assumption can be checked by plotting each difference against the true value of the required couch shift. In addition, by adding the LOA and mean difference to the plot, a clear visualization of the agreement between methods is shown [39]. To quantitatively assess the relationship between the differences and true couch shift values, Spearman's rank correlation coefficients were computed [39, 40]. Using this technique, both data sets are ranked by assigning an integer to each value. The smallest value in a given set is assigned a rank of 1, the second smallest value is assigned a rank of 2, and so on, with the largest value assigned rank N, corresponding to the total number of observations in both data sets. If a tie occurs between two values, the average rank is assigned to both. Spearman's rank correlation coefficient, ρ, is then calculated using Equation 4.10, where r is the difference between paired ranks [41].

$$\rho = 1 - \frac{6\sum_{i=1}^{N} r_i^2}{N^3 - N} \tag{4.10}$$

The value of ρ indicates the strength of the relationship between the two variables being compared, and will always lie between ± 1. A perfect relationship is indicated if $\rho = \pm 1$. As ρ approaches zero, the strength of the correlation between the two variables diminishes.

The precision of the LOA was determined using 95 % confidence intervals, $CI(LOA)$. Similar to the $CI(\overline{x})$, these intervals were calculated using the standard error on the LOA, $SE(LOA)$, and the t-critical values discussed in section 4.3.1 for the given difference distribution. Assuming differences are normally distributed, $SE(LOA)$ is determined as [39]:

$$SE(LOA) = s_d \times \sqrt{\frac{(1 + \frac{1.96^2}{2})}{n}} \tag{4.11}$$

where n is the total number of differences and s_d is their standard deviation. Equation 4.12 gives the formula for $CI(LOA)$ [39], where $LOA+(t_{0.025,\ n-1} \times SE(LOA))$ is the upper confidence limit and $LOA-(t_{0.025,\ n-1} \times SE(LOA))$ is the lower confidence limit.

$$CI(LOA) = LOA \pm (t_{0.025,\ n-1} \times SE(LOA)) \tag{4.12}$$

4.3.3 F-Test For Equality of Variances

To compare the variability of US and FM couch shift distributions, an upper-tailed F-test was performed. This test of hypothesis determines if two populations have equal variances using sample data from each.

The null hypothesis, H_0, that the variance, σ_1^2, of population 1 is equal to the variance, σ_2^2, of population 2 is tested against the alternative hypothesis, H_a, that population 1 has greater variability than population 2:

$$\begin{aligned} H_0 &: \quad \sigma_1^2 = \sigma_2^2 \\ H_a &: \quad \sigma_1^2 > \sigma_2^2 \end{aligned} \tag{4.13}$$

Equation 4.14 defines the test statistic, f, where s_1^2 is the variance of sample data from population 1, with $m-1$ degrees of freedom, and s_2^2 is the variance of sample data from population 2, with $n-1$ degrees of freedom.

$$f = s_1^2/s_2^2 \tag{4.14}$$

At significance level α, the null hypothesis will be rejected if:

$$f \geq F_{\alpha,m-1,n-1} \tag{4.15}$$

where $F_{\alpha,m-1,n-1}$ is the F-critical value. The F-critical value follows an F-distribution with $m-1$ numerator degrees of freedom and $n-1$ denominator degrees of freedom.

It is the value the test statistic would have if the null hypothesis were true. F-critical values can be found in summary tables by locating the appropriate α, $m-1$, and $n-1$ [35].

Alternatively, the decision to accept or reject H_0 can be made based on the test "$p-value$". For an F-test, the $p-value$ is the probability that f will be at least as extreme as the value observed given that the null hypothesis is true [35]. It is determined by locating the appropriate f, $m-1$, and $n-1$ in the F-critical value summary table. If the $p-value$ is less than or equal to α, the null hypothesis is rejected at significance level α [35]. For this work, both F and $p-values$ were determined using Matlab's tables.

As an example of an F-test, consider the situation described by Equation 4.16:

$$\begin{array}{lll} Sample\ 1: & s_1 = 7.5 & m = 100 \\ Sample\ 2: & s_2 = 8.4 & n = 100 \\ H_0: & \sigma_1^2 = \sigma_2^2 & \\ H_a: & \sigma_1^2 > \sigma_2^2 & \end{array} \tag{4.16}$$

The f-statistics is:

$$f = (7.5)^2/(8.4)^2 = 0.8 \tag{4.17}$$

and the F-critical value with 99 numerator degrees of freedom and 99 denominator degrees of freedom for significance level 0.05 is:

$$F_{0.05,99,99} = 1.4 \tag{4.18}$$

Since:

$$0.8 < 1.4 \tag{4.19}$$

the null hypothesis cannot be rejected, and the probability that f is at least as

extreme as the value observed is:

$$p = 0.9 \tag{4.20}$$

4.3.4 Ninety-Five Percent Repeatability Coefficients

To assess the effects of US user variability on the agreement between US and FM measured couch shifts, 95 % repeatability coefficients were calculated. When considering intra-user variability, these coefficients indicate the maximum difference likely between 2 measurements made by the same user, while for inter-user variability, repeatability coefficients indicate the maximum difference likely between 2 measurements made by 2 different users. If repeatability coefficients are comparable to the LOA, user variability is a significant source of disagreement between two methods of measurement [39].

Intra-user 95 % repeatability coefficients, R_{intra}, are calculated from repeated measurements taken on several subjects by one user. The standard deviation of these repeated measurements, s_{intra}, is determined using one-way analysis of variance (ANOVA), and for this study, one-way ANOVA was performed using Matlab's built-in ANOVA functions. R_{intra} was then calculated from s_{intra} using Equation 4.21 [42].

$$R_{intra} = \pm 1.96 \times \sqrt{2} \times s_{intra} \tag{4.21}$$

Inter-user 95 % repeatability coefficients, R_{inter} are calculated from measurements made by several users on the same set of subjects. The standard deviation of such measurements, s_{inter}, is determined using two-way ANOVA, and again, for this study, was calculated using Matlab. R_{inter} was then determined from s_{inter} using Equation 4.22 [42].

$$R_{inter} = \pm 1.96 \times \sqrt{2} \times s_{inter} \tag{4.22}$$

Chapter 5

Results and Discussion I: Benchmarking the Restitu System for Ultrasound Image Guided Radiation Therapy

This chapter explores the results obtained by comparing the Restitu System to FMs for prostate localization. Specific experimental procedures used in collection of US and FM couch shifts are described in detail in section 5.1. Section 5.2 provides results for the comparison between FMs and assisted and manual segmentation US, and a discussion of these results is given in section 5.3.

5.1 Experimental Procedure

Eleven patients undergoing 3D CRT for prostate cancer provided written informed consent to participate in the evaluation of prostate localization using FMs and US. All patients underwent daily prostate localization using both techniques, but any required couch shifts were performed based on FM measurements, and Restitu derived couch shifts were collected for comparison purposes only.

The experimental procedure used to collect US and FM couch shift measurements is shown in Figure 5.1. All patients had 3 gold FMs inserted into their prostate gland. A CT scan was then obtained of their pelvic area, immediately followed by acquisition

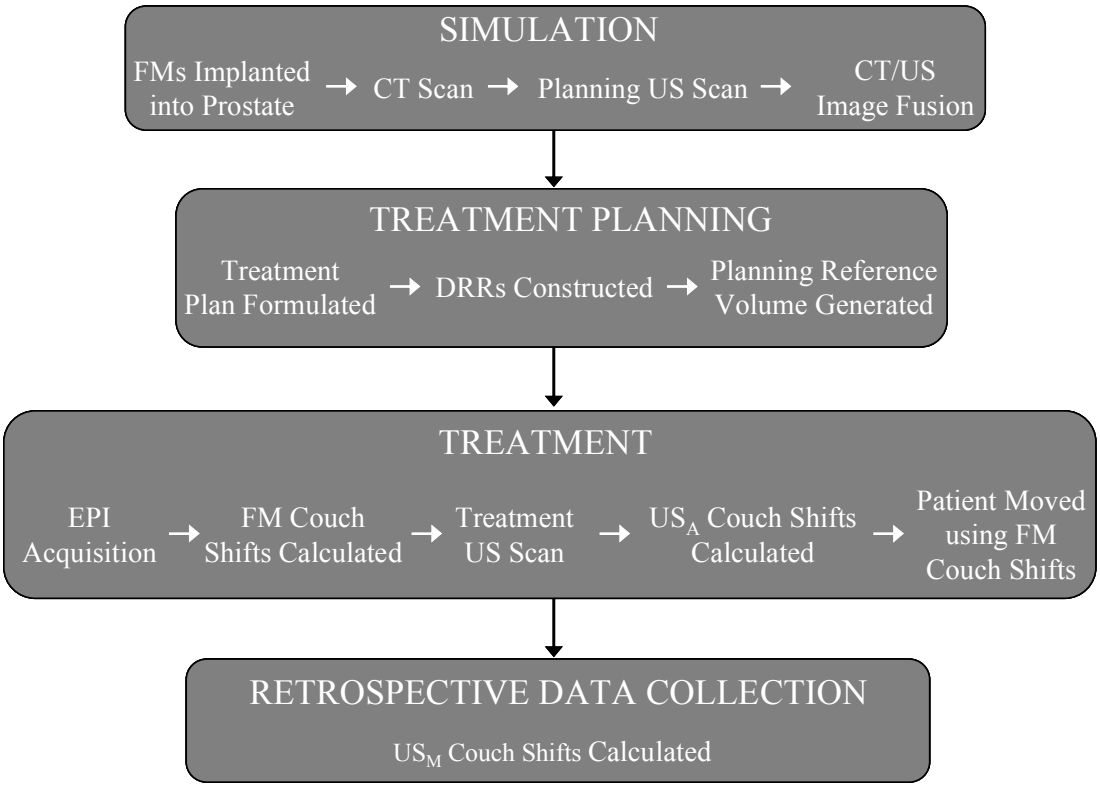

Figure 5.1: Procedure for collecting couch shift measurements using FMs and the Restitu System.

of the planning US scan. The CT and US image sets were then transferred to the Restitu workstation and fused to ensure accurate patient positioning between the two scans. This was followed by formulation of a treatment plan, construction of DRRs, and generation of a PRV for US prostate localization. At each day of treatment, patients were positioned on the treatment couch, and EPIs were acquired. While FM couch shifts were being calculated, a treatment US scan was acquired and assisted segmentation couch shifts were measured. Patients were then moved based on FM couch shifts if necessary. After completion of all patient treatments, the retrospective data collection was performed. Details of these general procedures were discussed in chapter 4.

Following data collection, LOA were calculated based on differences between FM and assisted and manual segmentation US couch shift measurements. A clinical tol-

erance of $\pm 3\ mm$ was chosen. Differences greater than $\pm 3\ mm$ were considered clinically unacceptable, and thus LOA larger than $\pm 3\ mm$ indicate US cannot safely replace FMs for prostate localization. This value was chosen based on the precision of FM prostate localization reported in the literature ($\leq 2.0\ mm$) [12–14], and the size of the PTV margins used for the patients in this study ($7 - 10\ mm$). If US measurements agree with FM measurements to within $\pm 3\ mm$, the prostate will be within the boundaries of the radiation field aperture (defined by the PTV) after repositioning using US. For example, in a worst case scenario, where FMs measurements are inaccurate by $2\ mm$, and US measurements are different from FM measurements by $3\ mm$, the position of the prostate after realignment using US will differ from the planned position by a maximum of $5\ mm$. Thus, the prostate will remain within the radiation field boundaries after repositioning using US if the $\pm 3\ mm$ criterion for agreement is met.

5.2 Results

Of the 11 study patients, the first two were excluded from analysis to allow US operators to gain experience using the Restitu System. A third patient was excluded from analysis due to FM migration, but the remaining patients showed no indication of FM movement within the prostate gland. Finally, one additional patient was excluded from the retrospective analysis due to data restoration failure. Consequently, 8 patients were included in the comparison of assisted segmentation US to FMs, and 7 patients in the retrospective analysis comparing manual segmentation US to FMs. This provided a total of 278 daily FM couch shifts in each direction: AP, RL, and SI. Of these, 255 corresponding couch shift measurements were made in each direction using assisted segmentation US, and 181 shifts were retrospectively re-calculated using manual segmentation US.

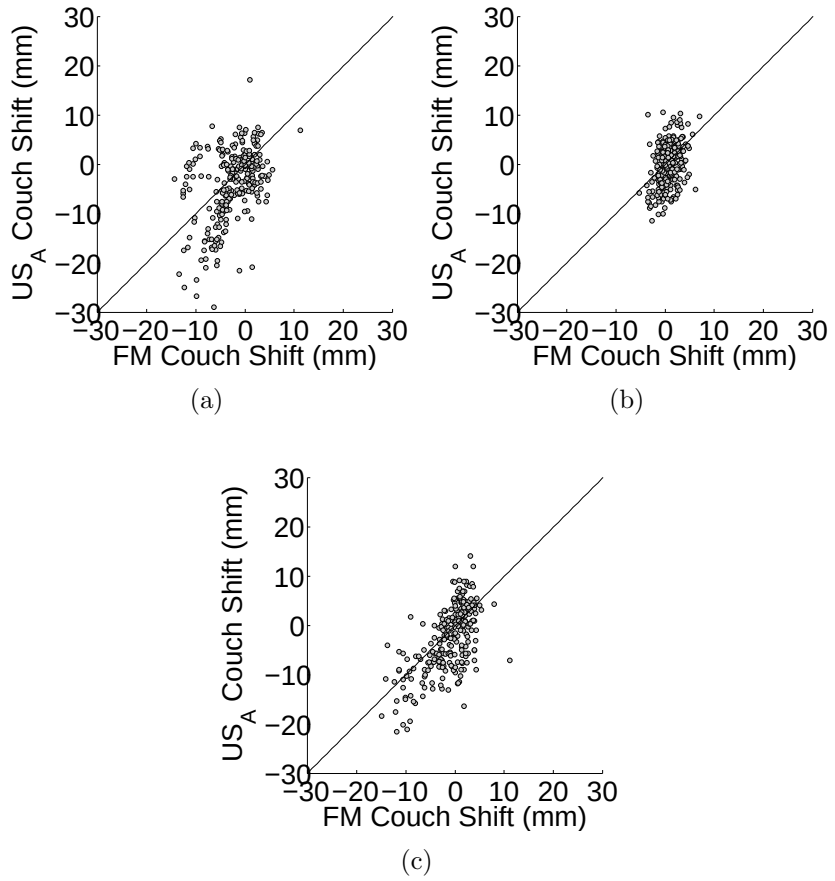

Figure 5.2: Scatter plots comparing FM measured couch shifts with those measured using assisted segmentation ultrasound in the a) AP, b) RL, and c) SI directions.

5.2.1 Assisted Segmentation Ultrasound vs. Fiducial Markers

A total of 255 FM and assisted segmentation US paired couch shift measurements were compared in each of the AP, RL, and SI directions. Scatter plots showing the assisted segmentation US (US_A) and FM measurements are presented in Figure 5.2, where positive couch shifts are posterior, left, and inferior (see diagram of anatomical directions, section 2.2). These plots show that all three distributions encompass the line of agreement. However, the spread of data points is large, particularly for the US measurements, which exceed the spread in FM measurements for all three directions. The tightest distribution occurs in the RL scatter plot, suggesting that agreement

between assisted segmentation US and FMs is best for this direction.

Table 5.1: Mean, 95 % confidence interval for the mean (CI), standard deviation (SD), median, and minimum and maximum (Min/Max) couch shift measurements made using FMs and assisted segmentation ultrasound. Positive values represent couch shifts towards posterior, left, and inferior.

	FM			US_A		
	AP	RL	SI	AP	RL	SI
Mean (mm)	-2.7	0.8	-1.3	-3.9	-0.2	-2.6
CI for the Mean (mm)	(-3.2, -2.1)	(0.5, 1.0)	(-1.8, -0.8)	(-4.8, -3.0)	(-0.7, 0.4)	(-3.4, -1.8)
SD (mm)	4.4	2.0	4.3	7.3	4.4	6.7
Median (mm)	-2.4	0.6	-0.2	-2.5	0.2	-2.0
Min/Max (mm)	-14.3/11.3	-5.2/7.0	-14.9/11.2	-29.0/17.2	-11.4/10.6	-21.6/14.2

The mean, standard deviation, median, and minimum and maximum values for the FM and assisted segmentation US couch shift distributions are summarized in Table 5.1, and confirm the scatter plot observations. For all couch shift directions, the mean US and FM shifts agree within their standard deviations. In addition, the standard deviation and the range of measured couch shifts (Min/Max) is greater in the US measurements than in FM measurements for all directions.

Differences between FM and assisted segmentation US paired couch shifts were also calculated ($FM - US$), and used to compute the LOA. As discussed in section 4.3.2, LOA are determined assuming differences follow an approximately normal distribution, and that the mean and standard deviation of differences are reasonably constant throughout the range of measurements [40]. For this work, the assumption of normality is valid according to the central limit theorem. Moreover, the relative frequency histograms shown in Figure 5.3 qualitatively demonstrate the differences (D_{FM-US_A}) follow an approximately normal distribution in each direction. In addition, these plots visually demonstrate that in all directions, clinically significant lack

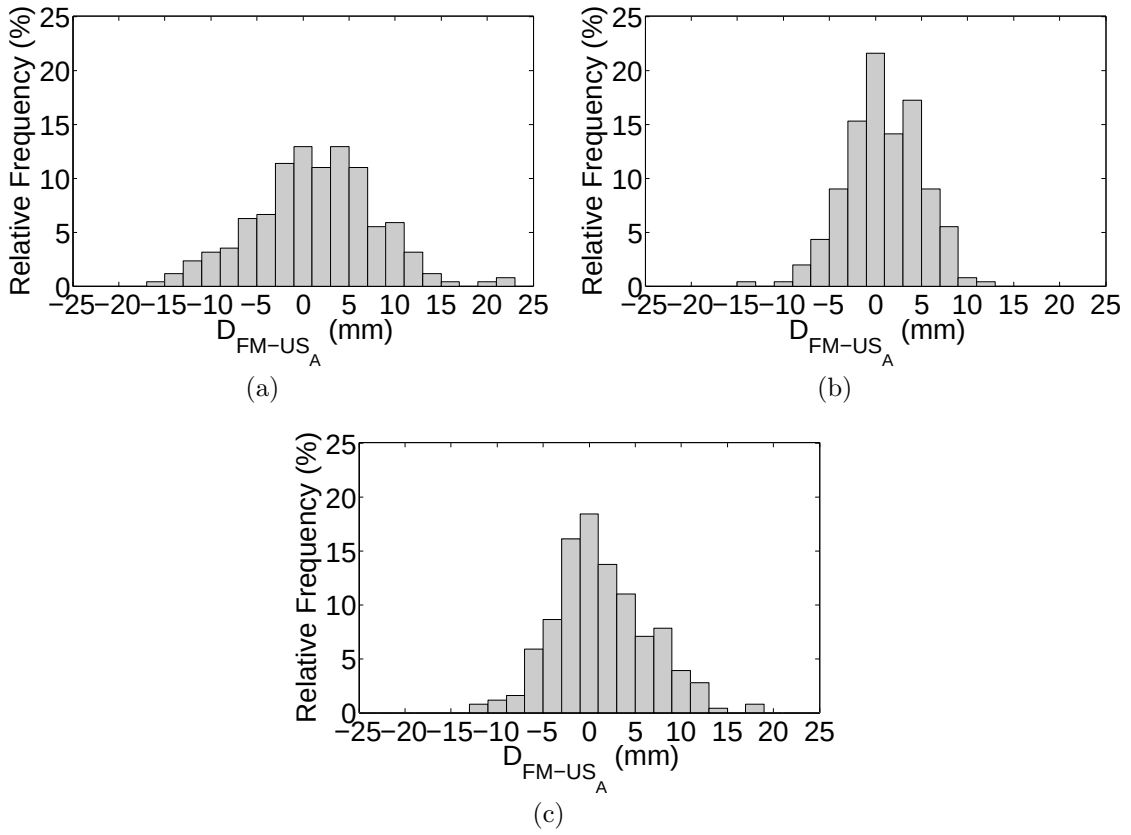

Figure 5.3: Relative frequency histograms of computed differences between FM and assisted segmentation ultrasound measured couch shifts in the a) AP, b) RL, and c) SI directions.

of agreement ($> 3\ mm$) is frequent, and severe disagreement ($\geq 10\ mm$), although rare, occurs in all directions.

The second assumption was checked by plotting each difference against the true value of the couch shift being measured, and calculating Spearman's rank correlation coefficient. Due to the proven accuracy and precision of FM measurements [12–18], for this work, FM couch shifts were used as the best estimate of the true value of a given couch shift. Figure 5.4 shows plots of the differences between FM and assisted segmentation US couch shifts vs. the corresponding FM measurement for each direction. These plots qualitatively indicate the mean and standard deviation of the differences are reasonably constant throughout the range of measurements for each di-

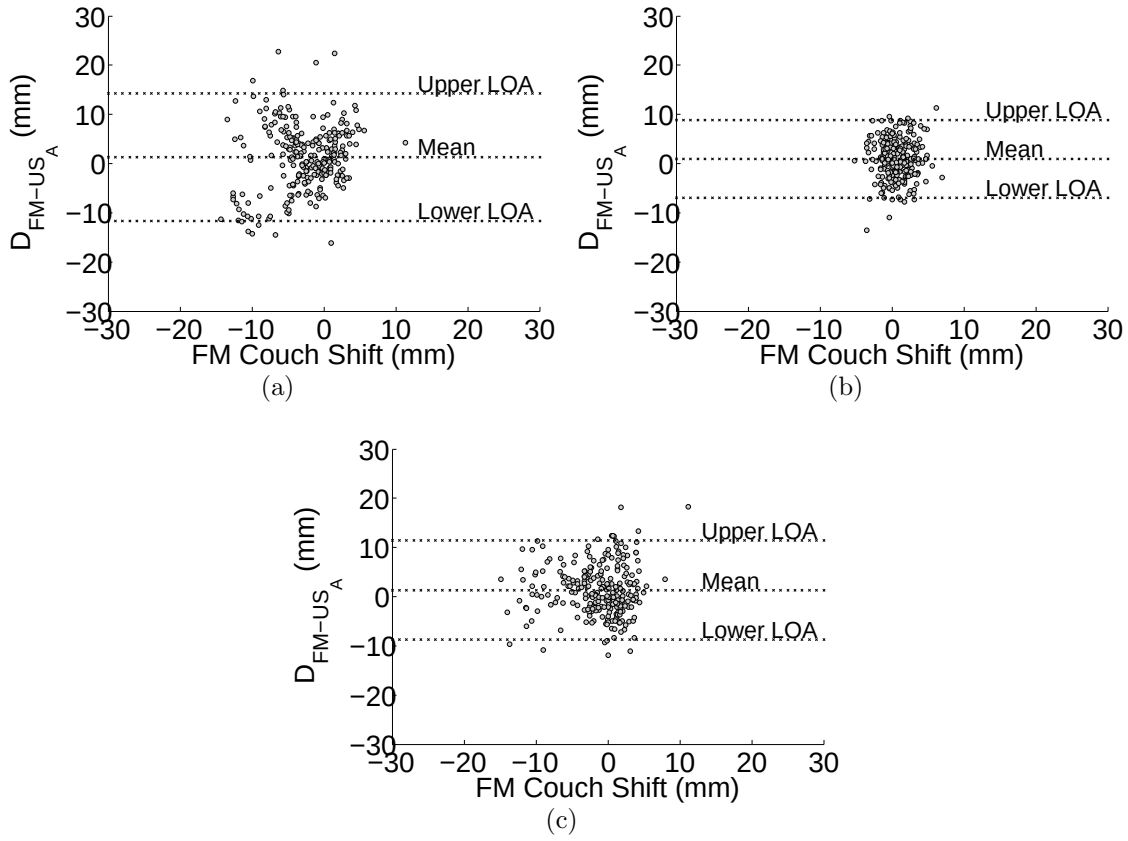

Figure 5.4: Differences between FM and assisted segmentation ultrasound couch shift measurements vs. the corresponding FM measurements in the a) AP, b) RL, and c) SI directions.

rection. The corresponding Spearman rank correlation coefficients (defined in section 4.3.2) were 0.1, 0.0, and −0.1 in the AP, RL, and SI directions respectively, confirming the plot observations. In addition, by including the LOA and mean difference, these plots provide a clear picture of the agreement between the two methods.

The mean difference, LOA, and percentage of differences that fell between ±1, ±2, ±3, ±5, and ±10 *mm* are summarized in Table 5.2. As mentioned above, differences greater than ±3 *mm* were considered unacceptable, and thus LOA larger than ±3 *mm* indicate assisted segmentation US cannot safely replace FMs for prostate localization.

The LOA were −11.7 *mm* to 14.3 *mm*, −7.0 *mm* to 8.8 *mm*, and −8.8 *mm* to 11.4 *mm* in the AP, RL, and SI directions respectively, clearly exceeding the ±3 *mm*

Table 5.2: Differences between paired FM and assisted segmentation ultrasound couch shift measurements, and the corresponding LOA in the AP, RL, and SI directions. Positive values represent couch shifts towards posterior, left, and inferior.

	D_{FM-US_A}		
	AP	RL	SI
Mean (mm)	1.3	0.9	1.3
CI for the Mean (mm)	(0.5, 2.1)	(0.4, 1.4)	(0.7, 1.9)
Standard Deviation (mm)	6.6	4.0	5.1
Lower LOA (mm)	-11.7	-7.0	-8.8
CI for Lower LOA (mm)	(-13.1, -10.3)	(-7.8, -6.1)	(-9.9, -7.7)
Upper LOA (mm)	14.3	8.8	11.4
CI for Upper LOA (mm)	(12.9, 15.7)	(7.9, 9.6)	(10.3, 12.5)
-1 $\leq D_{FM-US_A} \leq$ 1 (%)	12.9	21.6	18.4
-2 $\leq D_{FM-US_A} \leq$ 2 (%)	23.5	38.4	31.4
-3 $\leq D_{FM-US_A} \leq$ 3 (%)	35.3	51.0	48.2
-5 $\leq D_{FM-US_A} \leq$ 5 (%)	54.9	77.3	67.8
-10 $\leq D_{FM-US_A} \leq$ 10 (%)	85.9	98.8	92.9

criterion for agreement. The corresponding percentage of differences that did fall within ± 3 mm were 35.3 %, 51.0 %, and 48.2 %. Overall, assisted segmentation US agrees best with FM in the RL direction and most poorly in the AP direction.

5.2.2 Manual Segmentation Ultrasound vs. Fiducial Markers

A retrospective comparison of FMs and manual segmentation US was carried out for 181 paired couch shift measurements. Scatter plots comparing the manual segmentation US (US_M) and FM shifts are shown in Figure 5.5, where sign conventions remain positive for posterior, left, and inferior couch shifts. As for assisted segmentation US, all three distributions encompass the line of agreement but display significant scatter, particularly for the US measurements, which contain greater dispersion than

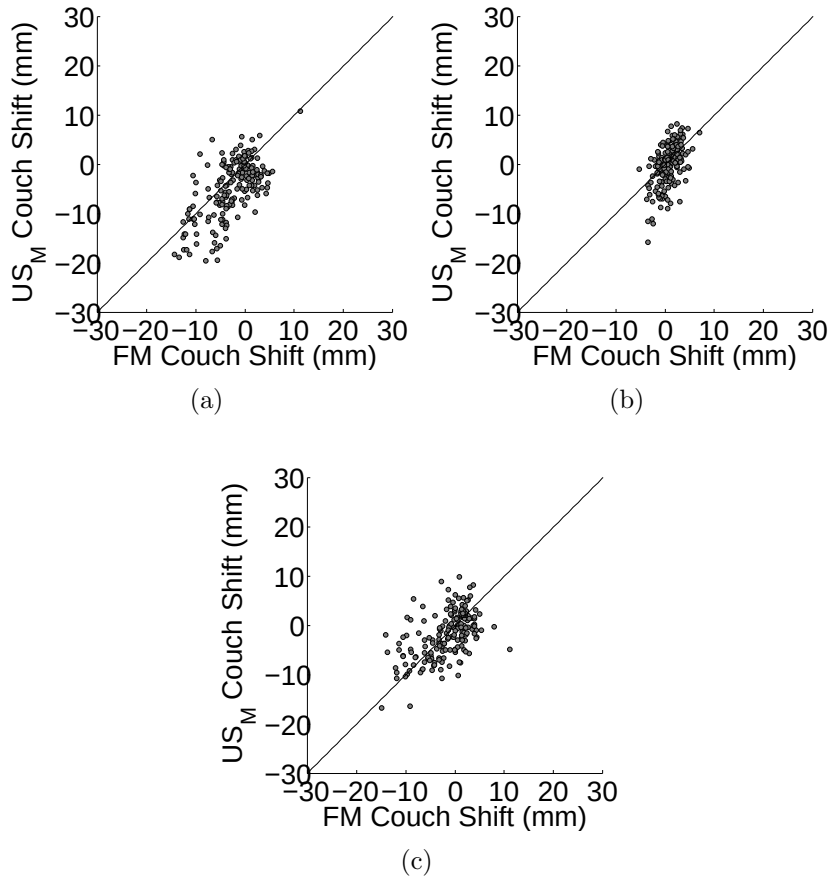

Figure 5.5: Scatter plots comparing FM and manual segmentation ultrasound measured couch shifts in the a) AP, b) RL, and c) SI directions.

the FM measurements for all three directions. Nevertheless, manual segmentation distributions appear slightly less scattered compared to the assisted segmentation measurements (Figure 5.2). The tightest distribution occurs in the RL scatter plot, suggesting again that agreement between US and FM is best for this direction.

Table 5.3 summarizes the mean, standard deviation, median, and minimum and maximum couch shift values for both the FM and manual segmentation US distributions. Note that the FM values differ very slightly from those in Table 5.1 due to the subset of FM data used for the retrospective analysis. Again, the numerical statistics confirm the scatter plot observations. For all couch shift directions, the mean US and FM shifts agree within their standard deviations. Moreover, for all measurements,

Table 5.3: Mean, 95 % confidence interval for the mean (CI), standard deviation (SD), median, and minimum and maximum (Min/Max) couch shift measurements made using FMs and manual segmentation ultrasound. Positive values represent couch shifts towards posterior, left, and inferior.

	FM			US_M		
	AP	RL	SI	AP	RL	SI
Mean (mm)	-2.7	0.7	-1.7	-4.8	-0.1	-1.8
CI for the Mean (mm)	(-3.3, -2.0)	(0.4, 1.0)	(-2.4, -1.0)	(-5.6, -3.9)	(-0.7, 0.5)	(-2.5, -1.1)
SD (mm)	4.6	2.0	4.6	5.9	4.1	4.7
Median (mm)	-2.5	0.6	-0.4	-3.5	0.3	-1.5
Min/Max (mm)	-14.3/11.3	-5.2/7.0	-14.9/11.2	-19.6/10.9	-15.8/8.2	-16.7/9.9

the standard deviation and the range of measured couch shifts (Min/Max) is greater for the manual segmentation US measurements than the FM measurements.

Further analysis was based on the differences between paired FM and manual segmentation US couch shift measurements (D_{FM-US_M}), which were used to calculate the LOA. As for assisted segmentation, the assumptions underlying the LOA were verified using the central limit theorem and Figures 5.6 and 5.7. The corresponding Spearman rank correlation coefficients for the plots shown in Figure 5.7 were 0.2, 0.0, and 0.4 in the AP, RL, and SI directions respectively.

Table 5.4 summarizes the mean difference, LOA, and percentage of differences that fell between ± 1, ± 2, ± 3, ± 5, and ± 10 mm, where again, differences greater than ± 3 mm were considered unacceptable. LOA were found to be -6.8 mm to 11.1 mm, -6.0 mm to 7.7 mm, and -8.7 mm to 9.0 mm in the AP, RL, and SI directions respectively. These values clearly exceed the ± 3 mm criterion for agreement in all directions, with the corresponding percentage of differences lying within ± 3 mm being 45.3 %, 64.1 %, and 55.2 %. However, these results do show better agreement with FM is achieved with manual rather than assisted segmentation US regardless of

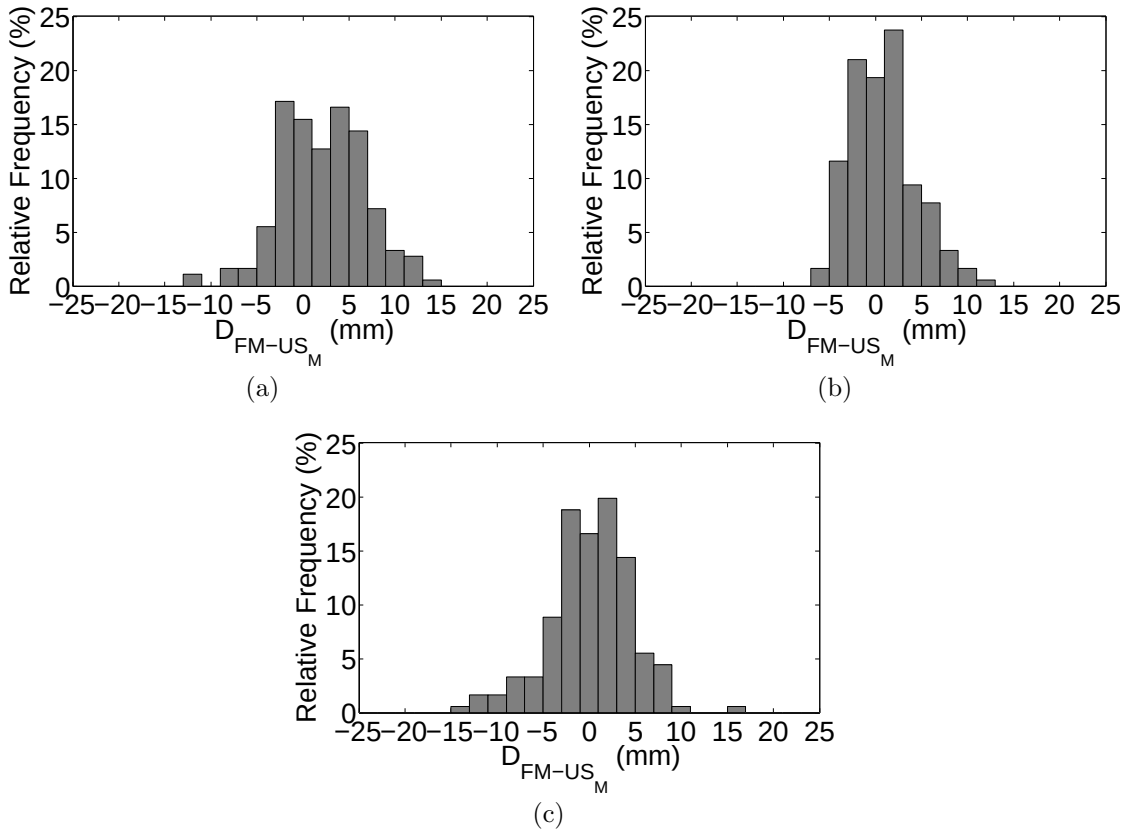

Figure 5.6: Relative frequency histograms for differences between FM and manual segmentation ultrasound measured couch shifts in the a) AP, b) RL, and c) SI.

couch shift direction. Overall, manual segmentation US agrees better with FMs in the RL direction and most poorly in the AP direction.

5.3 Discussion

Daily couch shifts measured using the Restitu System were compared with those measured using FMs to determine if the less invasive US technique could replace FMs for daily patient positioning in prostate cancer IGRT. Although descriptive statistics indicate that mean US and FM couch shifts agree within their standard deviations, a more detailed analysis of paired differences between the two techniques showed a clinically unacceptable level of agreement. In this work, differences between US and FM measured couch shifts greater than 3 *mm* were deemed clinically significant. To

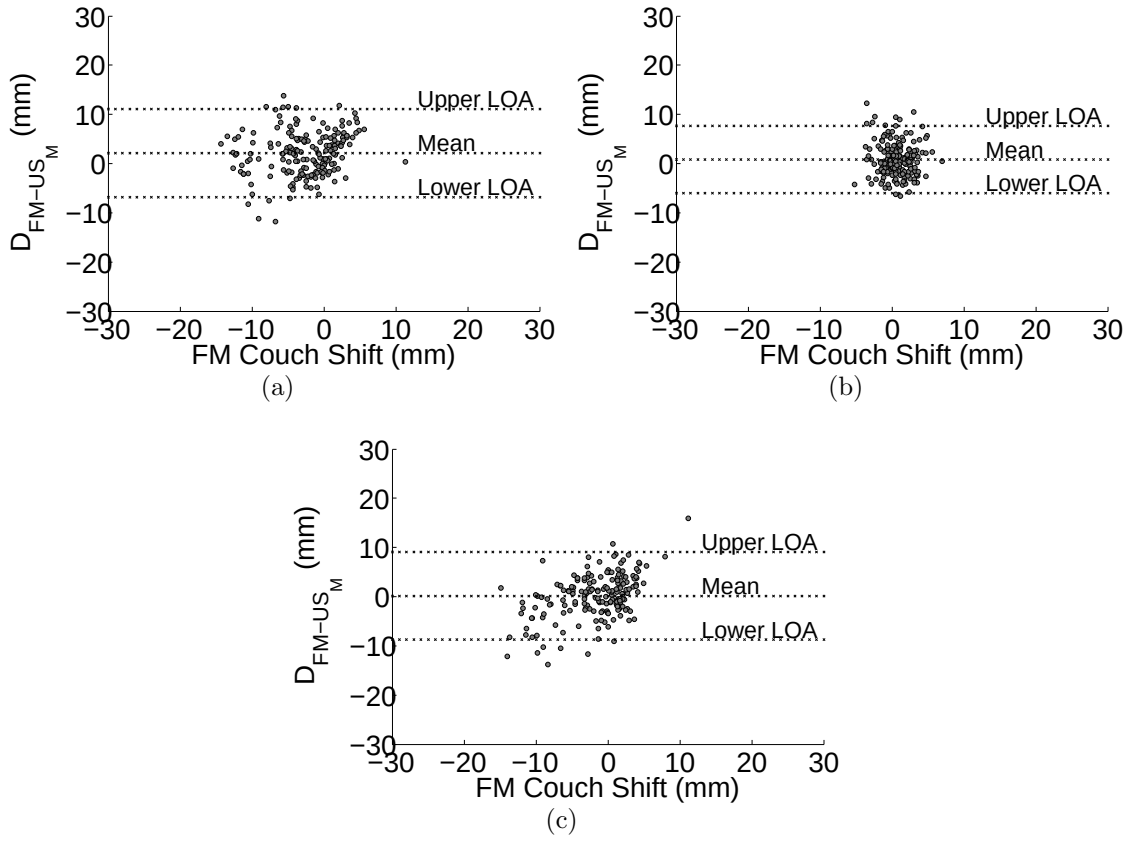

Figure 5.7: Differences between FM and manual segmentation ultrasound couch shift measurements vs. corresponding FM measurements for the a) AP, b) RL, and c) SI directions.

enable use of either technique interchangeably, or to safely replace FMs with US, 95 % of US and FM measured couch shifts should agree to within $\pm 3\ mm$. For both assisted and manual segmentation US, LOA showed 95 % of differences were significantly greater than $\pm 3\ mm$ in all directions (AP, RL, and SI). Restitu measurements agreed best with FM measurements in the RL direction for both segmentation methods. Greater agreement in this direction may be due to reduced prostate organ motion along this orientation. In addition, manual segmentation provided better agreement in all cases and is the recommended mode of use of the Restitu System. However, even use of manual segmentation provided a level of agreement with FMs that was far below the criterion for clinical acceptability: 45.3 %, 64.1 %, and 55.2 % of differences

Table 5.4: Differences between paired FM and manual segmentation ultrasound couch shift measurements, and the corresponding LOA in the AP, RL, and SI directions. Positive values represent couch shifts towards posterior, left, and inferior.

	D_{FM-US_M}		
	AP	RL	SI
Mean (mm)	2.1	0.8	0.2
CI for the Mean (mm)	(1.4, 2.8)	(0.3, 1.3)	(-0.5, 0.8)
Standard Deviation (mm)	4.6	3.5	4.5
Lower LOA (mm)	-6.8	-6.0	-8.7
CI for Lower LOA (mm)	(-8.0, -5.7)	(-6.9, -5.1)	(-9.9, -7.6)
Upper LOA (mm)	11.1	7.7	9.0
CI for Upper LOA (mm)	(9.9, 12.2)	(6.8, 8.5)	(7.9, 10.2)
-1 $\leq D_{FM-US_A} \leq$ 1 (%)	15.5	19.9	16.6
-2 $\leq D_{FM-US_A} \leq$ 2 (%)	29.8	47.0	40.9
-3 $\leq D_{FM-US_A} \leq$ 3 (%)	45.3	64.1	55.2
-5 $\leq D_{FM-US_A} \leq$ 5 (%)	67.4	85.1	78.5
-10 $\leq D_{FM-US_A} \leq$ 10 (%)	94.5	98.9	95.6

fell within ± 3 mm in the AP, RL, and SI directions respectively.

5.3.1 Sources of Error

Several possible factors may contribute to the observed discrepancy between US and FM measured couch shifts. Discrepancy could occur if either localization system was not performing correctly. However, the FM image guidance system underwent rigorous testing at time of commissioning, and regular quality assurance (QA) of the treatment planning system (DRR construction) and EPID ensure the continued accuracy of its performance. The Restitu System has also proved to perform very well during phantom based calibration and repeated QA testing. Weekly and monthly QA results have shown the system to be highly robust and to provide measures of

couch shift reproducible to within $\pm 0.5\ mm$ [43]. Quality assurance performed daily using a simplified procedure and phantom has also shown consistent couch shift measurements, meeting our QA tolerance of $\pm 2\ mm$ daily [44]. In summary, both systems perform very well in QA situations and system performance is not responsible for the observed discrepancy.

Transducer pressure, the pressure exerted on the patient's abdomen by the operator when acquiring an US scan, has been cited as a possible source of error in US derived measures of prostate displacement (or required couch shift) [45–47]. In this study, anatomical structures visible on planning US images were found to coincide with the corresponding anatomy in CT images when the two scans were fused on the Restitu workstation. Thus, evidence of operator applied transducer pressure was not observed for any of the planning US scans. However, the mean US derived daily couch shifts were more anterior and superior (more negative) than those measured using FMs (Tables 5.1 and 5.3). These directions are consistent with the possibility of operator induced transducer pressure displacing the prostate posteriorly and inferiorly during acquisition of treatment US scans.

Lastly, US image quality and US user variability may have contributed to the discrepancy observed between US and FM measurements. These potential sources of error were investigated in depth, and therefore, a separate chapter (chapter 6) has been devoted to their examination.

5.3.2 Comparison to Other Studies

Currently, three US image guidance systems are available for prostate localization during IGRT: the B-mode Acquisition and Targeting (BAT) System (North American Scientific, Chatsworth, CA), SonArray (Varian Medical Systems, Palo Alto, CA), and the Restitu System. The BAT System and SonArray are inter-modality US systems that determine prostate displacements by comparing US images acquired each day of treatment to target and critical structure volumes delineated on CT images used

in treatment planning [48]. In contrast, as discussed in section 4.2, Restitu is an intra-modality US system that compares US images acquired each day of treatment to US images acquired at treatment planning.

Each of the available US prostate localization systems have been investigated previously. The BAT System, being the first available US image guidance device for prostate localization, has been discussed extensively in the literature. Seven groups reported the results of BAT shifts in studies aimed at evaluating the clinical utility of the BAT System [47, 49, 50] and quantifying prostate organ motion [51–54]. Four additional groups investigated the accuracy of the BAT System for prostate localization by comparing BAT shifts to those measured using another prostate localization method. Lattanzi et al. [55] compared couch shifts measured using the BAT System to those measured using daily CT scans. A special immobilization device was used to transfer patients between the CT and treatment rooms. This pilot study revealed significant correlations between BAT and CT shifts for all directions, promoting two follow-up studies [56, 57] where the comparison was repeated, but with patients remaining in the CT simulator room during US localization. Again, a high correlation was found, and it was concluded that US localization using the BAT System is safe and as accurate as CT localization.

The BAT System was found to be less favorable in a study by Serago et al. [58]. This group compared couch shifts measured using the BAT System to shifts measured using stereoscopic kV x-ray images of 3 - 6 implanted FMs (see section 2.2 for a discussion on stereoscopic localization). FM prostate localization was also performed and was assumed to correctly determine the shifts required to realign the prostate into the treatment beam. Differences between couch shifts measured using FM prostate localization and BAT and between FM prostate localization and stereoscopic localization were calculated and compared using descriptive statistics. It was concluded that US prostate localization using the BAT System is less accurate

than localization using stereoscopic imaging.

The accuracy of the BAT System was also assessed in a study by Langen et al. [59], where couch shifts measured using the BAT System were compared to those measured using FM prostate localization. Using a paired t-test, significant systematic differences between BAT and FM couch shift distributions were discovered in the RL ($p < 0.0001$) and SI ($p < 0.0001$) directions. They concluded the performance of the BAT System, as compared to FMs, dependents on the direction in which couch shifts are measured.

McNair et al. [60], in a similar study, compared couch shifts measured using the BAT System to those measured using 2 CT scans of 3 implanted FMs. Differences between BAT and CT measured shifts were calculated and it was concluded that systematic differences are present between the two methods of prostate localization.

Investigations into the accuracy of SonArray have also been reported. Scarbrough et al. [48] compared couch shifts measured using SonArray to couch shifts measured using stereoscopic kV x-ray images of 4 implanted FMs. Differences between couch shifts measured using the two techniques were compared using a paired t-test and it was found that SonArray suggests different couch shifts than stereoscopic localization. In a follow-up study by Fuller et al. [61], the same data was re-analyzed using the LOA to determine the interchangeability of the two methods. It was found that 95 % of the time, SonArray and stereoscopic imaging measurements agree within approximately 15 mm in AP, RL, and SI. They concluded from these results that US localization using SonArray is not equivalent to stereoscopic imaging of FMs, and the two should not be used interchangeably.

In addition to the present study, Tirona et al. [62] and Cury et al. [19] have reported the results of Restitu measured shifts. Cury et al. [19] also compared couch shifts measured using the Restitu System to those measured by the BAT System and biweekly CT scans. Differences between paired couch shift measurements were

analyzed using a Wilcoxon matched-pairs signed-rank test, with statistically significant differences indicated by $p < 0.05$. Comparison of Restitu and BAT couch shifts showed statistically significant differences in the RL ($p < 0.0001$) and SI ($p < 0.0001$) directions, but not in the AP direction ($p = 0.604$). In addition, no statistically significant differences were found between Restitu and CT measured couch shifts in the AP ($p = 0.405$), RL ($p = 0.314$), or SI ($p = 0.727$) directions. It was concluded that couch shifts measured using the Restitu System are consistent with those measured by CT, and more accurate than those measured using the BAT System.

Table 5.5 summarizes means and standard deviations (where available) for couch shift distributions reported in the studies discussed above [19, 47–55, 57, 59, 62]. The results of the present work are included for comparison. When employed sign conventions were available, directional data has been included using a common sign convention: positive couch shifts in posterior, left, and inferior directions. Mean values will reflect any systematic difference in patient position at time of CT simulation compared to time of treatment and variation between studies in both the magnitude and direction of these mean values can be expected. A comparison of standard deviations in US measured couch shifts shows that those determined in this work are consistent with the findings in most other studies. The trend observed here of a lower standard deviation in the RL than in the AP or SI directions is also common.

Table 5.6 summarizes the means and standard deviations for differences (where available) between measurements made using US and a second method of prostate localization (i.e. FMs, CT, a second US system, etc.) that were reported by the studies discussed above [19, 55, 56, 58–61]. The corresponding values determined in this work are included for comparison. For the majority of the studies included in the table, means and standard deviations of differences are comparable to those found in this work. The recent works of McNair et al. [60] and Fuller et al. [61] strongly support the conclusion drawn from this work, that US cannot safely replace FMs for

Table 5.5: Anterior-posterior, RL, and SI mean couch shift measurements and standard deviations (SD), in parenthesis, reported in other US image guidance studies. The corresponding quantities measured in the present study using assisted and manual segmentation ultrasound are also reported. Positive values represent couch shifts towards posterior, left, and inferior.

Authors	US System	AP Mean (SD) (mm)	RL Mean (SD) (mm)	SI Mean (SD) (mm)
Lattanzi et al. [55]	BAT	-0.2 (4.6)	-0.1 (3.4)	0.0 (5.7)
Lattanzi et al. [57]	BAT	3.0 (8.3)	-1.86 (5.7)	2.6 (6.5)
Powell et al. [51]∗	BAT	NA	2.2 (3.9)	5.8 (5.2)
Langen et al. [59]	BAT	0.7 (5.2)	-1.8 (3.9)	2.7 (4.5)
Serago et al. [47]∗	BAT	1.3 (4.7)	0.3(2.5)	1.0 (5.1)
Cury et al. [19]	BAT	-3.8 (7.7)	0.9 (3.7)	1.4 (5.6)
Little et al. [52]∗	BAT	1.4 (6.4)	0.82 (3.2)	1.7 (6.4)
Trichter et al. [53]	BAT	3.2 (5.6)	3.2 (4.6)	3.1 (7.3)
Morr et al. [49]†	BAT	4.7 (2.7)	2.6 (2.1)	4.2 (2.8)
Chandra et al. [50]	BAT	0.51 (4.9)	0.54 (2.8)	-0.71 (4.4)
Fung et al. [54]	BAT	-1.5 (6.4)	0.2 (5.2)	1.4 (5.7)
Scarbrough et al. [48]	SonArray	0.80 (6.33)	-1.92 (5.38)	3.50 (7.11)
Cury et al. [19]	Restitu	-3.9 (7.9)	0.05 (4.2)	-4.6 (7.2)
Tirona et al. [62]	Restitu	6.0 (4.4)	0.4 (2.9)	-2.4 (4.8)
Present Work	Restitu (US_A)	-3.9 (7.3)	-0.2 (4.4)	-2.6 (6.7)
Present Work	Restitu (US_M)	-4.8 (5.9)	-0.1 (4.1)	-1.8 (4.7)

∗ Sign conventions unavailable.
† Couch shift magnitudes.

daily prostate localization. Langen et al. [59] and Serago et al. [58] suggest US may be safe to use but other methods are more favorable.

The works by Lattanzi et al. [55, 56] and Cury et al. [19] show less variation between US and CT than demonstrated here between US and FMs, and both studies conclude that US based prostate localization is functionally equivalent to CT. In addition, Cury et al. concluded that intra-modality US is more accurate than inter-

Table 5.6: Anterior-posterior, RL, and SI means and standard deviations (SD), in parenthesis, reported in the literature for differences between couch shifts measured using US and another image guidance technique. The corresponding quantities measured in the present study using assisted and manual segmentation ultrasound are also reported. Positive values represent couch shifts towards posterior, left, and inferior.

Authors	Comparison	AP Difference Mean (SD) (mm)	RL Difference Mean (SD) (mm)	SI Difference Mean (SD) (mm)
Lattanzi et al. [55]∗	BAT vs. CT	3.0 (1.8)	2.4 (1.8)	4.6 (2.8)
Lattanzi et al. [56]	BAT vs. CT	0.09 (NA)	0.16 (NA)	0.03 (NA)
Langen et al. [59]	BAT vs. FM	-0.2 (3.7)	-1.6 (3.1)	2.7 (3.9)
Serago et al. [58]†	BAT vs. FM	1.4 (4.8)	0.4 (3.3)	1.5 (5.7)
McNair et al. [60]	BAT vs. FM	3.2 (3.2)	2.2 (3.7)	3.3 (3.5)
Fuller et al. [61]	SonArray vs. FM	1.9 (5.7)	-1.2 (4.7)	3.5 (6.7)
Cury et al. [19]	Restitu vs. CT	-0.2 (1.6)	0.2 (1.7)	0.1 (1.4)
Cury et al. [19]	Restitu vs. BAT	0.1 (4.2)	0.9 (3.4)	6.0 (5.1)
Present Work	Restitu (US_A) vs. FM	1.3 (6.6)	0.9 (4.0)	1.3 (5.1)
Present Work	Restitu (US_M) vs. FM	2.1 (4.6)	0.8 (3.5)	0.2 (4.5)

∗ Absolute magnitude difference.
† Sign conventions unavailable.

modality US. The different conclusions drawn from these studies compared to this work may stem from the fact that both of these studies compared US to CT instead of FMs. Moreover, in both studies, CT scans were performed biweekly during the last weeks of treatment and the number of CT determined couch shifts was much less than the number of daily acquired FM shifts analyzed in this study.

Chapter 6

Results and Discussion II: Major Sources of Discrepancy Between Restitu and Fiducial Marker Measurements

This chapter investigates several major sources of discrepancy between couch shifts measured using the Restitu System and FM prostate localization. Comparison of the variability associated with each method is discussed in section 6.1. The effects of US image quality and user variability on the agreement between the two methods are discussed sections 6.2 and 6.3 respectively.

6.1 Variability of Couch Shift Measurements

An F-test was used to assess variance equality between FM and US measured couch shifts following the procedures outlined in section 4.3.3. The null hypothesis that FM and US distributions have equal variance was tested against the alternative hypothesis that US shifts show greater variation using a significance level of 0.05. The resulting p-values are summarized in Table 6.1. Assisted segmentation US measurements had significantly greater variability ($p < 0.001$) compared to FM measurements in all three directions. Manual segmentation US measurements had significantly greater variability in the AP and RL directions ($p < 0.001$), but were not significantly dif-

Table 6.1: Results of an F-test to compare the variability observed in FM couch shift measurements to that observed in assisted and manual segmentation ultrasound measurements in the AP, RL, and SI directions. P-values < 0.001 indicate significant differences in variability.

	US_A vs. FM			US_M vs. FM		
	AP	RL	SI	AP	RL	SI
P value	$p < 0.001$	$p < 0.001$	$p < 0.001$	$p < 0.001$	$p < 0.001$	$p > 0.1$

ferent from FM measurements ($p > 0.1$) in the SI direction.

This trend of significantly greater variability in US measurements suggests there is greater uncertainty associated with the Restitu System and error in US measures is a likely cause of the observed discrepancy with FMs. Potential sources of US uncertainty include US image quality and user variability, and are investigated in detail below.

6.2 Ultrasound Image Quality

6.2.1 Experimental Procedure

To assess the effects of US image quality on the agreement between FM and US measured couch shifts, US images were sorted into high and low image quality groups, and the LOA were recalculated for each group independently. Images were evaluated by one user (HJ) during retrospective data collection of manual segmentation shifts. Image quality was defined based on the visibility of the prostate-bladder interface, prostate-rectal interface, and the prostate itself. If all three structures were visible, the image was considered to be of sufficient quality for accurate prostate localization, and placed in the high image quality group. Absence of any of these key anatomical features indicated the image was not adequate for accurate prostate localization, and was placed in the low image quality group. Figure 6.1a shows an example of a high

quality US image, while Figure 6.1b illustrates a low quality image.

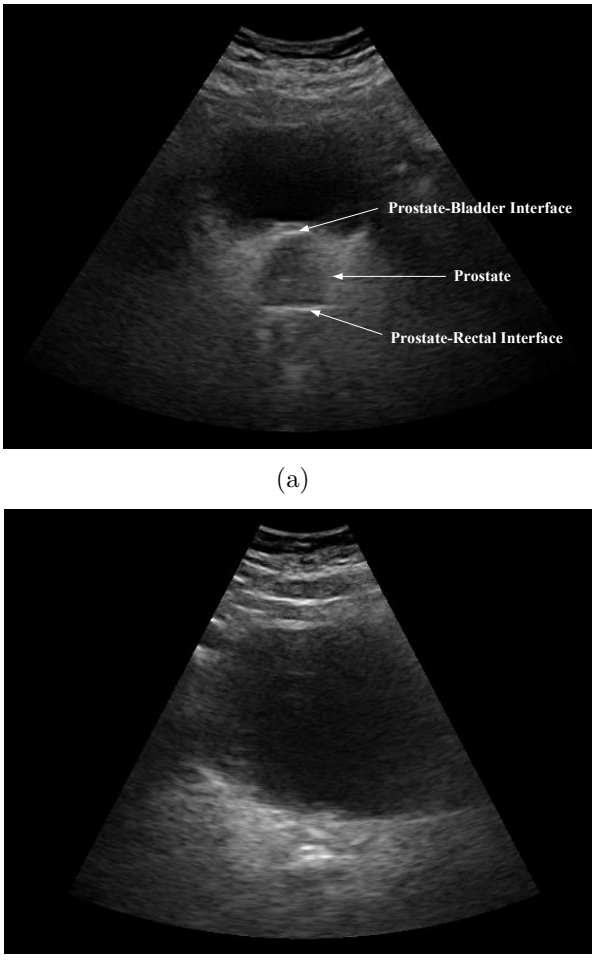

(a)

(b)

Figure 6.1: Examples of US images with a) high and b) low image quality.

6.2.2 Results

For this study, 67 % and 33 % of assisted segmentation US images, and 68 % and 32 % of manual segmentation US images had high and low image quality respectively.

The mean difference between FM and US paired measurements, LOA, and percentage of differences that fell between ± 1, ± 2, ± 3, ± 5 and ± 10 mm for the high and low image quality groups are summarized in Table 6.2 for assisted segmentation US and in Table 6.3 for manual segmentation US. The assumptions underlying the

Table 6.2: Effects of US image quality on the differences between paired FM and assisted segmentation ultrasound couch shift measurements in the AP, RL, and SI directions. Positive values represent couch shifts towards posterior, left, and inferior.

	D_{FM-US_A}					
	AP		RL		SI	
	High	Low	High	Low	High	Low
Mean (mm)	2.1	0.1	1.0	-0.5	1.2	4.0
CI for the Mean (mm)	(1.1, 3.1)	(-1.8, 2.0)	(0.4, 1.6)	(-1.6, 0.7)	(0.3, 2.1)	(2.5, 5.5)
Standard Deviation (mm)	5.6	7.5	3.4	4.5	5.2	5.8
Lower LOA (mm)	-8.9	-14.6	-5.7	-9.3	-8.9	-7.4
CI for Lower LOA (mm)	(-10.7, -7.2)	(-17.9, -11.3)	(-6.8, -4.7)	(-11.2, -7.3)	(-10.5, -7.3)	(-9.9, -4.8)
Upper LOA (mm)	13.2	14.8	7.7	8.3	11.4	15.4
CI for Upper LOA (mm)	(11.4, 14.9)	(11.5, 18.1)	(6.7, 8.8)	(6.3, 10.3)	(9.8, 12.9)	(12.8, 17.9)
$-1 \leq D_{FM-US_A} \leq 1$ (%)	15.3	9.8	27.4	9.8	16.1	11.5
$-2 \leq D_{FM-US_A} \leq 2$ (%)	29.0	13.1	42.7	29.5	27.4	19.7
$-3 \leq D_{FM-US_A} \leq 3$ (%)	40.3	19.7	54.8	44.3	44.4	36.1
$-5 \leq D_{FM-US_A} \leq 5$ (%)	62.9	44.3	82.3	77.0	65.3	50.8
$-10 \leq D_{FM-US_A} \leq 10$ (%)	87.9	83.6	100.0	98.4	91.1	88.5

LOA (approximately normal difference distribution, mean and standard deviation of differences reasonably constant throughout the range of measurements) were verified as in sections 5.2.1 and 5.2.2 using Figures 6.2–6.5 and the central limit theorem. The Spearman rank correlation coefficients in the AP, RL, and SI directions were 0.1, -0.1, and -0.1 for assisted segmentation shifts measured using high quality images, 0.2, -0.2, and 0.3 for assisted segmentation shifts measured using low quality images, 0.1, 0.1, and 0.3 for manual segmentation shifts measured using high quality images and 0.3, -0.3, and 0.5 for manual segmentation shifts measured using low quality images respectively.

Table 6.3: Effects of US image quality on differences between paired FM and manual segmentation ultrasound couch shift measurements in the AP, RL, and SI directions. Positive values represent couch shifts towards posterior, left, and inferior.

	D_{FM-US_M}					
	AP		RL		SI	
	High	Low	High	Low	High	Low
Mean (mm)	1.9	2.6	0.8	1.0	0.1	0.3
CI for the Mean (mm)	(1.1, 2.7)	(1.4, 3.9)	(0.2, 1.3)	(-0.1, 2.1)	(-0.6, 0.8)	(-1.2, 1.8)
Standard Deviation (mm)	4.5	4.7	3.1	4.2	3.9	5.7
Lower LOA (mm)	-7.0	-6.6	-5.3	-7.3	-7.6	-10.8
CI for Lower LOA (mm)	(-8.4, -5.6)	(-8.7, -4.4)	(-6.2, -4.3)	(-9.2, -5.4)	(-8.8, -6.4)	(-13.4, -8.3)
Upper LOA (mm)	10.7	11.8	6.8	9.3	7.7	11.4
CI for Upper LOA (mm)	(9.3, 12.1)	(9.7, 13.9)	(5.9, 7.7)	(7.4, 11.2)	(6.5, 8.9)	(8.8, 14.0)
$-1 \leq D_{FM-US_M} \leq 1$ (%)	15.4	15.5	22.8	13.8	18.7	12.1
$-2 \leq D_{FM-US_M} \leq 2$ (%)	30.9	27.6	54.5	31.0	47.2	27.6
$-3 \leq D_{FM-US_M} \leq 3$ (%)	50.4	34.5	71.5	48.3	57.7	50.0
$-5 \leq D_{FM-US_M} \leq 5$ (%)	71.5	58.6	88.6	77.6	83.7	67.2
$-10 \leq D_{FM-US_M} \leq 10$ (%)	94.3	94.8	99.2	98.3	97.6	91.4

For all directions and segmentation methods, couch shifts determined using high quality US images agree more closely with FM shifts than those measured using low quality US images. This is highlighted in the reduced range of the LOA and greater percentage of measurements between ± 3 mm for the high quality groups compared to the low quality groups. However, the percentage of differences between ± 3 mm for the high image quality groups (40.3 %, 54.8 %, and 44.4 % in AP, RL, and SI respectively for US_A and 50.4 %, 71.5 %, and 57.7 % in AP, RL, and SI respectively for US_M) still fall quite short of the desired 95 %.

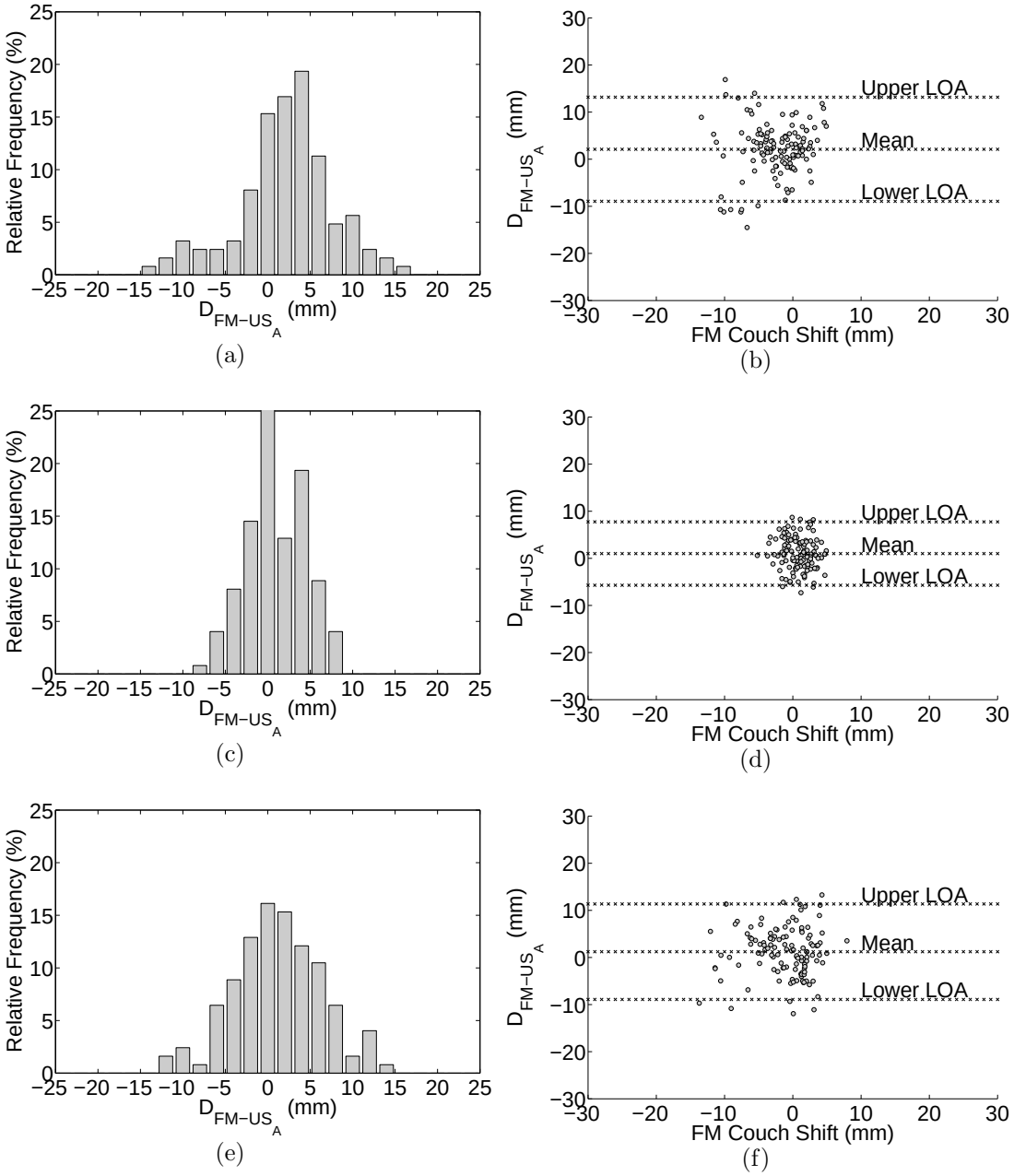

Figure 6.2: Relative frequency histograms and scatter plots used to check the assumptions underlying the LOA for differences associated with *high quality* US images examined using *assisted segmentation* in the AP (a–b), RL (c–d), and SI (e–f) directions.

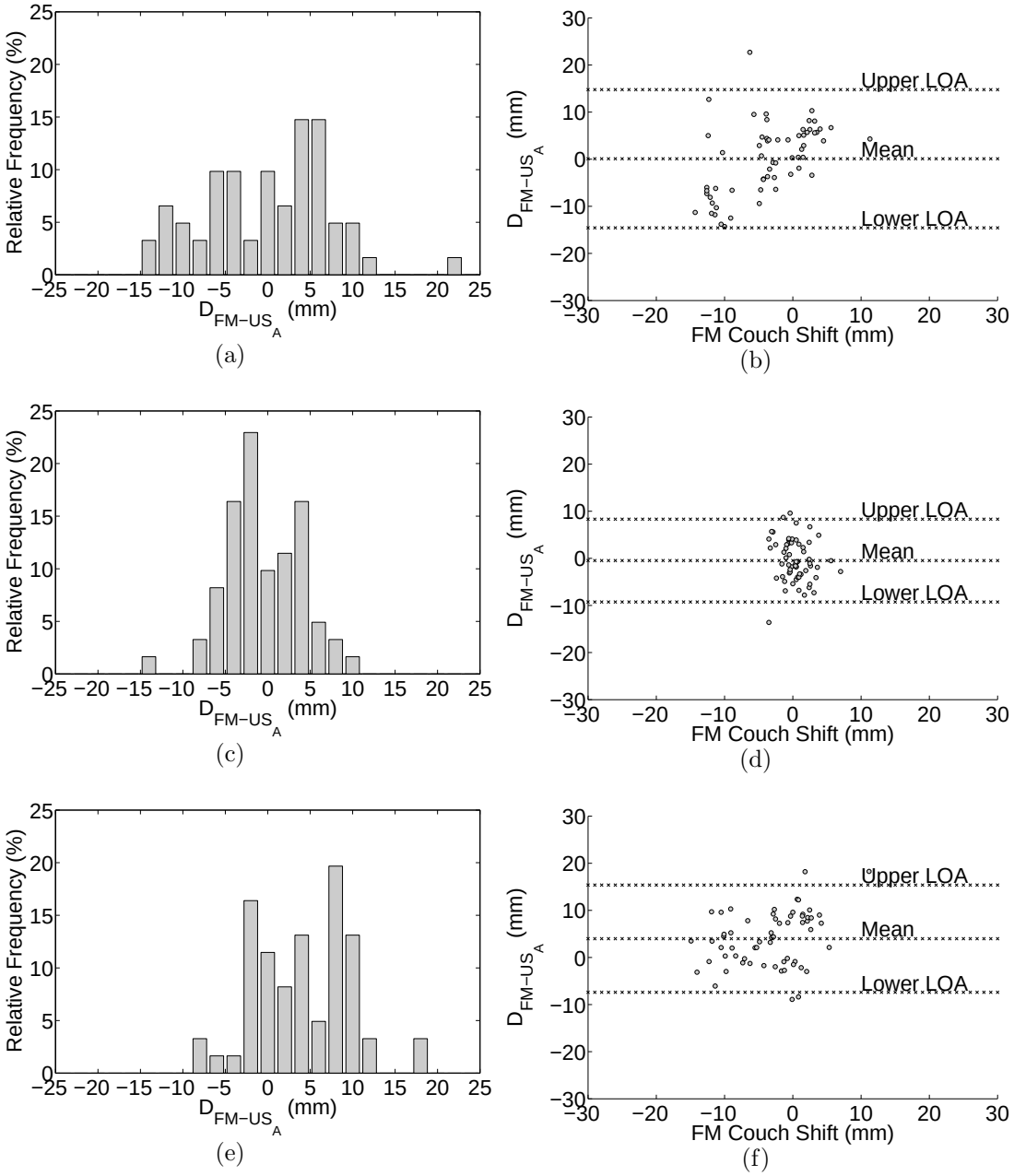

Figure 6.3: Relative frequency histograms and scatter plots used to check the assumptions underlying the LOA for differences associated with *low quality* US images examined using *assisted segmentation* in the AP (a–b), RL (c–d), and SI (e–f) directions.

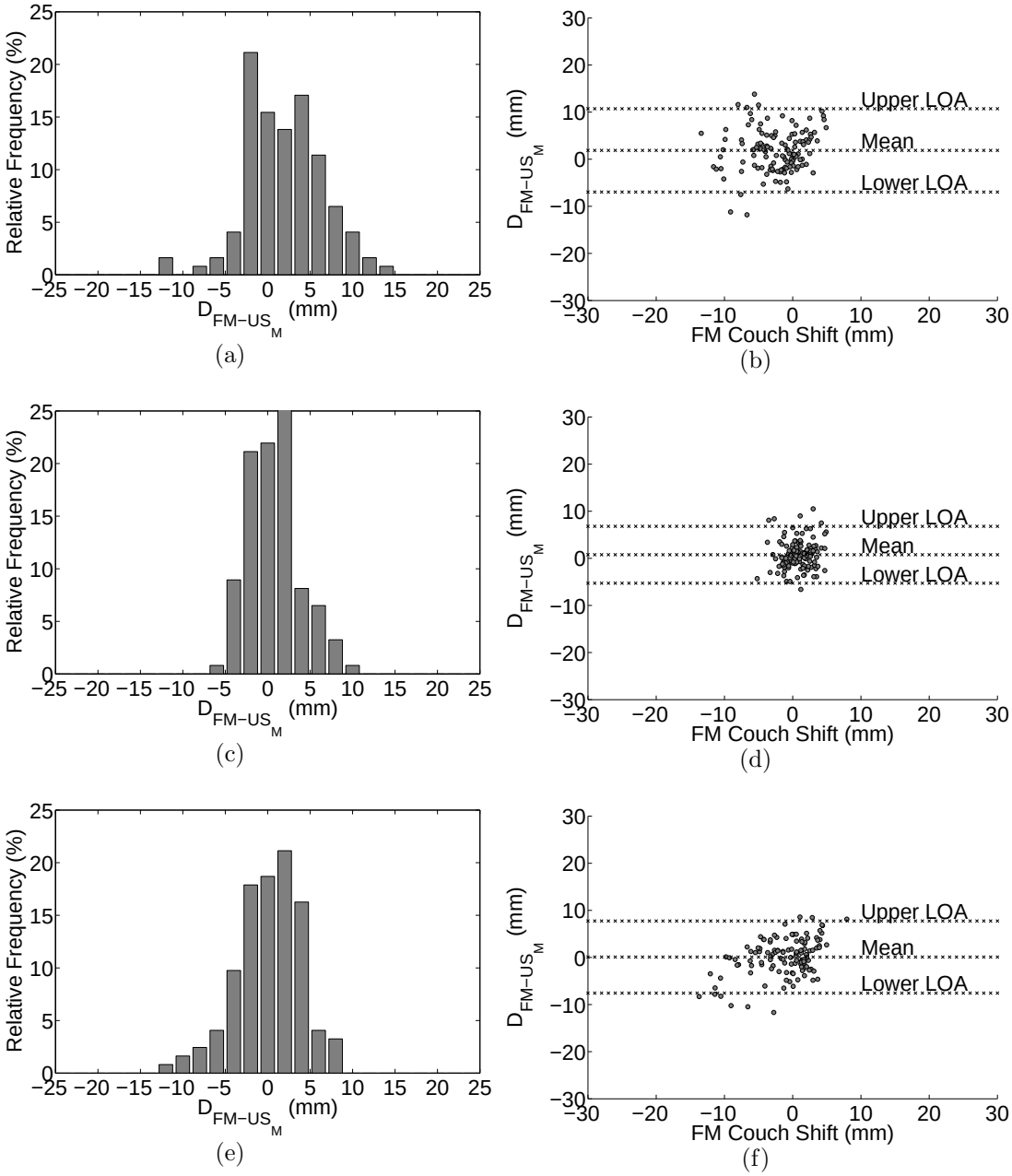

Figure 6.4: Relative frequency histograms and scatter plots used to check the assumptions underlying the LOA for differences associated with *high quality* US images examined using *manual segmentation* in the AP (a–b), RL (c–d), and SI (e–f) directions.

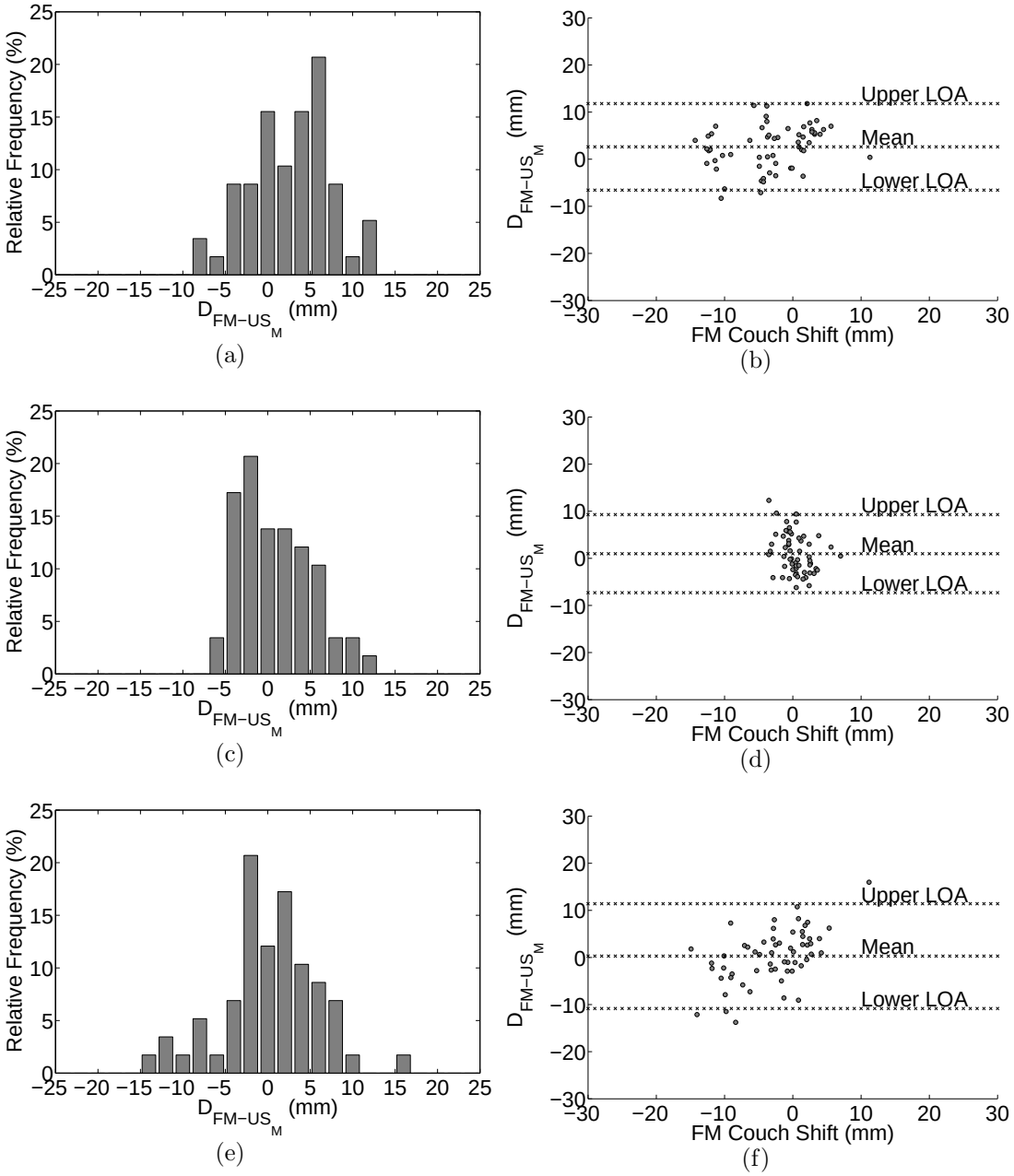

Figure 6.5: Relative frequency histograms and scatter plots used to check the assumptions underlying the LOA for differences associated with *low quality* US images examined using *manual segmentation* in the AP (a–b), RL (c–d), and SI (e–f) directions.

6.2.3 Discussion

Image quality was shown to affect the agreement between Restitu and FM measured couch shifts. Both for assisted and manual segmentation US, restricting the LOA analysis to US images of high quality produced greater agreement with FMs. Furthermore, even with high image quality, manual segmentation provided better agreement with FMs in all directions compared to assisted segmentation. This suggests problems with the assisted segmentation algorithm may also be a source of discrepancy between assisted segmentation US and FM measurements.

Several factors were noted as affecting US image quality, the most consistently consequential being patient bladder filling. Without a full bladder, the overall clarity of prostate US images decreases dramatically. Ultrasound system settings (noise rejection level, brightness, etc.) are also important for optimizing image quality. These are user defined, and inappropriate settings can result in images that are too dark, too bright, too grainy etc. to be correctly interpreted. The clarity of the prostate in US images can also be affected by the anatomical position of the prostate and the patient's abdominal contour. It was observed that both prostate position directly underneath the pubic bone and a large, sloping, abdominal contour make it difficult to position the transducer with the skin contact necessary to acquire high quality images, particularly of the inferior portion of the prostate. Difficulties in transducer handling were also noted to produce image artifacts which can obscure the prostate and produce low quality images.

Based on these findings, it is recommended that every effort be made to achieve high quality US images that are free from image artifacts when using the Restitu System. In addition, couch shifts determined using low quality US images should not be performed.

6.3 Ultrasound User Variability

6.3.1 Experimental Procedure

The effects of US intra- and inter-user variability on the agreement between Restitu and FM measured couch shifts were examined separately. US intra-user variability was quantified by two users: the first user, a radiation therapist, made repeated couch shift measurements using assisted segmentation US, and the second user, a physicist, made replicate measurements using manual segmentation US. In both cases, 5 repeated measurements were made for each of 10 US scans in the AP, RL, and SI directions.

To ensure users were not influenced by any previous measurements made on a particular scan [39], the value of each measurement was hidden from the user. In addition, the identity of the US scan under examination was concealed, and the order in which scans were examined was randomized. Repeated measurements were then used to calculated R_{intra} as outlined in section 4.3.4, and these values were compared to the corresponding LOA to determine if intra-user variability was a significant source of disagreement between US and FM measurements.

Inter-user variability was examined by 8 users: 2 radiation oncologists, 3 physicists, and 3 radiation therapists. Each user measured couch shifts in the AP, RL, and SI directions for 10 US scans, twice, once using assisted segmentation US and once manual segmentation US.

Similar to the intra-user investigation, couch shift values determined by each user were kept secret from the other users to ensure independent measurements. These values were then used to calculate R_{inter} as described in section 4.3.4. Again, these coefficients were compared to the corresponding LOA to determine if inter-user variability was a significant source of discrepancy between the two methods.

	US_A			US_M		
	AP	RL	SI	AP	RL	SI
R_{intra}	±6.3	±5.0	±7.5	±4.0	±5.5	±3.1
R_{inter}	±17.8	±6.1	±8.2	±6.4	±6.5	±8.1
LOA	(-11.7, 14.3)	(-7.0, 8.8)	(-8.8, 11.4)	(-6.8, 11.1)	(-6.0, 7.7)	(-8.7, 9.0)

Table 6.4: Intra- and inter-user 95 % repeatability coefficients and the corresponding LOA for both assisted and manual segmentation US in the AP, RL, and SI directions.

6.3.2 Results

A total of 50 couch shift measurements were collected in each of the AP, RL, and SI directions using both assisted and manual segmentation US for the intra-user variability investigation. Similarly, 80 couch shifts were measured in each direction using each segmentation technique for the inter-user analysis.

Table 6.4 summarizes R_{intra}, R_{inter}, and the corresponding LOA for both assisted and manual segmentation US. The effects of US intra-user variability on the agreement between US and FM measures are direction and segmentation method dependent. Intra-user variability is a significant source of discrepancy in the RL direction for both assisted and manual segmentation US, as R_{intra} are comparable to the LOA. In addition, R_{intra} is comparable to the lower limit of agreement in the SI direction for assisted segmentation US, and in the AP direction for manual segmentation US, indicating intra-user variability has a moderate effect on agreement in these cases. Furthermore, intra-user variability is a weak contributor to the lack of agreement in the AP direction for assisted segmentation US, and in the SI direction for manual segmentation US, as R_{intra} are considerably smaller than the LOA.

Inter-user variability has a stronger impact on the agreement between US and FM measurements than intra-user variability, as R_{inter} fall closer to the LOA than R_{intra}

for all directions and segmentation methods. Nevertheless, the effects of inter-user variability are also dependent on direction and segmentation method.

Inter-user 95 % repeatability coefficients are comparable to the LOA in the AP direction for assisted segmentation US, in the RL direction for both segmentation methods, and in the SI direction for manual segmentation US. This indicates inter-user variability is a significant source of discrepancy between US and FM measurements in these situations. In addition, inter-user variability is a moderate contributor to the discrepancies observed in the SI direction for assisted segmentation US and in the AP direction for manual segmentation US, as R_{inter} is comparable to the lower limit of agreement for these cases.

6.3.3 Discussion

Ultrasound intra-user variability was shown to be a significant contributor to the lack agreement observed between US and FM measured couch shifts in the RL direction for both assisted and manual segmentation US. Inter-user variability was shown to contribute more to the discrepancies observed than intra-user variability, and was a significant source of error in the AP and RL directions for assisted segmentation US, and in the RL and SI directions for manual segmentation US.

A potential source of user variability is the difficulty associated with interpreting US images. For example, FMs and calcifications present in the prostate can reflect incident US waves back to the transducer, causing white lines to appear in the resulting image. These image artifacts can be mistaken for prostate interfaces, and their distinction from true tissue boundaries can be quite subjective.

The directional dependence associated with the US user variability observed, particularly in the RL direction, may be due to certain characteristics of patient anatomy. When measuring couch shifts using the Restitu System, the position of the treatment contour is determined by the prostate-bladder interface and the prostate-rectal interface, both of which appear in the image as distinct horizontal white lines above

and below the prostate (see Figure 6.1a). However, no interfaces exist between the prostate and another structure in the RL dimension, so there are no strong vertical white lines to use as landmarks when positioning the treatment contour.

Significant user variability may have also occurred due to a lack of user expertise. While all users received extensive training from the US system manufacturer prior to the collection of any US couch shift measurements, these users were not US experts. Professional US technologists must receive extensive training over a period of at least one year before being able to apply for certification. It is possible that with further training and experience, measurements made by different users, or by the same user but at a different time, may agree more closely.

Furthermore, it is important to note that the assisted segmentation US couch shift measurements used for comparison with FMs were acquired at the treatment unit, while those collected using manual segmentation, and those used to investigate user variability, were collected at a different location using the Restitu workstation. Radiation therapists must work under strict time constraints at the treatment unit to ensure all treatments scheduled for a particular day are performed. Therefore, assisted segmentation US shifts used for comparison with FMs were collected under time restrictions, while all other measurements were taken with as much time as was needed to do so. As such, the user variability associated with assisted segmentation US may be underestimated, as users were able to collect data with more time and consideration.

Chapter 7

Results and Discussion III: Evaluation of the General Clinical Utility of the Restitu System

Displacement of the prostate from its planned treatment position can be corrected using a number of different techniques (as described in section 2.2). However, no correction method is without its own inherent uncertainty, and the prostate will remain displaced to a certain extent from the planned treatment position, even after a couch shift has been performed. For this reason, a margin, called the PTV margin (discussed in section 2.1.2), is added around the disease to account for uncertainties in the location of the tumor. The PTV is the radiation target. Therefore, smaller PTV margins are ideal as this ensures less healthy tissue is exposed to lethal doses of radiation. For IGRT treatments, the size of the PTV margin is determined by the accuracy of the organ localization technique employed. As such, evaluation of the size of PTV margins offers clinical comparison of the effectiveness of various image guidance techniques.

For prostate IGRT, FM localization is the most reliable correction method for returning the prostate to its planned treatment position [12–18], requiring smaller PTV margins than any other method. However, due to its simplicity, many cancer centers

still use BAM (outlined in section 2.1.3) alone for their prostate cancer treatments. Because BAM only corrects patient set-up errors, large PTV margins must be used to account for prostate organ motion, presenting a greater risk of radiation damage to healthy, normal structures. In contrast, while not as precise as the FM method, US prostate localization accounts for both set-up errors and organ motion, giving it a potential advantage over BAM.

This chapter assesses the general clinical utility of US prostate localization using the Restitu System by comparing its required PTV margins to those necessary for regular use of BAM. Required margins are compared for a variety of typical patient repositioning strategies, or patient protocols. Procedures used for comparison are outlined in section 7.1. Sections 7.2 and 7.3 provide results and discussion on the calculated margins respectively.

7.1 Experimental Procedure

PTV margins for use with the Restitu System or BAM during prostate IGRT were determined based on the accuracy associated with each method. For this analysis, accuracy was defined as the ability of a given image guidance system to return the prostate to the planned treatment position. Accuracy was measured by calculating the displacement of the prostate from the planned treatment position that remained after US or BAM shifts were performed. These displacements, or "residual errors", were then used to calculate PTV margins using a standard margin recipe. Margins were calculated for four clinically relevant patient repositioning protocols, two based on US measurements and two based on BAM measurements.

Patient repositioning protocols are outlined in section 7.1.1, while sections 7.1.2 and 7.1.3 provide details on how residual errors and PTV margins were calculated respectively.

7.1.1 Patient Protocols

Due to the results of chapters 5 and 6, only couch shifts derived from good quality US images, using manual segmentation, and their corresponding FM and BAM shifts were employed for each protocol, as this subset of data represents the best results obtainable with the Restitu System. Procedures for each protocol are summarized in table 7.1. No patients were actually moved using any of these procedures, but shifts were hypothetically performed for analysis purposes.

Table 7.1: Protocols used to perform couch shifts measured using US and BAM.

PROTOCOL	PROCEDURE
BAM_{All}	Every BAM couch shift is performed.
BAM_{NAL}	BAM couch shifts from the first three days of treatment are averaged. Patients are moved by an amount equal to the couch shift average on each subsequent day of treatment if it is $\geq 5\ mm$. If this average is $< 5\ mm$, no moves are performed on subsequent treatment days.
US_{All}	Every US couch shift is performed.
US_{3mm}	US couch shifts $\geq 3\ mm$ are performed. Shifts less than this amount are not performed.

Using the BAM_{All} and US_{All} protocols, every couch shift measured using BAM and the Restitu System was performed regardless of the magnitude of the measured shift. The BAM_{NAL} protocol is a version of the No Action Level (NAL) protocol [63]. Using this technique, BAM couch shifts from the first three days of treatment were averaged for each direction, AP, RL, and SI. If the average shift was $\geq 5\ mm$, a constant couch shift was performed on each subsequent day of treatment by an amount equal to this calculated average. If the average was $< 5\ mm$, no couch shifts were performed. A similar procedure was used for the US_{3mm} protocol. If US measured couch shifts for a given day of treatment were $\geq 3\ mm$, the couch shift was performed. Otherwise, no moves were performed.

7.1.2 Residual Errors

As mentioned above, residual errors provide a measure of the accuracy of a given image guidance system. Figure 7.1 illustrates how residual errors were calculated. The origin of the 3D coordinate system indicates the initial patient set-up position, or equivalently, the position of the prostate before any couch shifts were performed. Fiducial marker couch shifts, (FM_{AP}, FM_{RL}, FM_{SI}), were used to indicate the position of the prostate at time of treatment planning, as these measurements are known to return the prostate to the "planned treatment position" with a high degree of accuracy [12–14]. Ultrasound and BAM couch shift vectors, (US_{AP}, US_{RL}, US_{SI}) (shown here as US shifts for brevity), represent the position of the prostate after a move was made using either technique ("US position"). Using simple vector addition, residual errors for each direction, (RE_{AP}, RE_{RL}, RE_{SI}), were calculated based on couch shift data as shown in Equation 7.1.

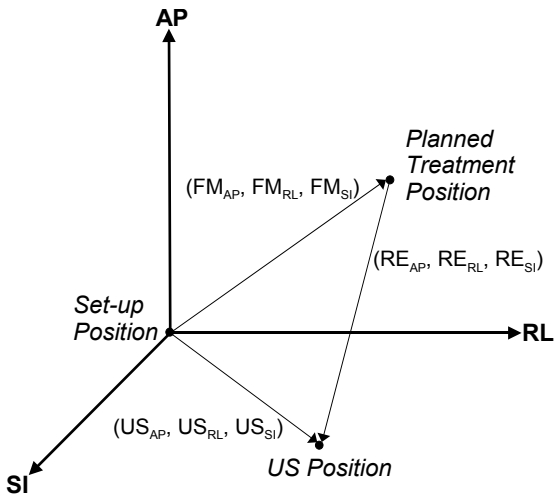

Figure 7.1: Vector diagram illustrating how REs were calculated based on US and FM couch shifts.

$$\begin{aligned} RE_{AP} &= US_{AP} - FM_{AP} \\ RE_{RL} &= US_{RL} - FM_{RL} \\ RE_{SI} &= US_{SI} - FM_{SI} \end{aligned} \tag{7.1}$$

7.1.3 Planning Target Volume Margins

Planning target volume margins were calculated based on the residual errors for each patient. For patient i, the mean residual error, $\overline{RE}_i$, and standard deviation of residual errors, SD_i, were calculated using Equations 4.2 and 4.5 respectively. Equations 7.2 and 7.3 were then used to calculate the standard deviation of patient residual error means, Σ, and the residual mean square (RMS) of patient residual error standard deviations, σ, respectively, where n is the total number of patients.

$$\Sigma = \sqrt{\frac{\sum_{i=1}^{n}(\overline{RE}_i - \frac{\sum_{i=1}^{n}\overline{RE}_i}{n})^2}{n-1}} \tag{7.2}$$

$$\sigma = \sqrt{\frac{\sum_{i=1}^{n} SD_i^2}{n}} \tag{7.3}$$

PTV margins were then calculated for each direction (AP, RL, and SI) using the margin recipe given in Equation 7.4 [64, 65].

$$PTV = 2.5\Sigma + 0.7\sigma \tag{7.4}$$

This recipe guarantees PTV margins will be large enough to ensure at least 95% of the prescribed radiation dose will be delivered to the tumor for 90% of patients treated. It is based on cumulative probability distributions for the radiation dose delivered to the tumor. Each prostate displacement is assumed to consist of two components: a random component associated with errors in treatment delivery (i.e. set-up errors) and a systematic component associated with errors in treatment planning (i.e. incorrect delineation of the prostate on CT slices leads to a constant displacement from the planned treatment position on each day of treatment). Random errors result in blurring of the dose distribution while systematic errors cause the distribution to shift with respect to the radiation target [64, 65].

Table 7.2: Sample data set used to illustrate how PTV margins are calculated using residual errors from 4 patients.

	Residual Errors (mm)			
	Patient 1	Patient 2	Patient 3	Patient 4
Fraction 1	-1	-2	0	1
Fraction 2	2	4	2	2
Fraction 3	3	1	2	4
Fraction 4	1	-3	1	1
Mean	1.3	0.0	1.3	2.0
Standard Deviation	1.7	3.2	1.0	1.4

As an example of how PTV margins were calculated, consider the data shown in Table 7.2. In this hypothetical situation, a PTV margin is calculated for a prostate localization system based on residual errors from 4 patients. The standard deviation of patient mean residual errors is:

$$\Sigma = \sqrt{\frac{(1.3-1.2)^2 + (0.0-1.2)^2 + (1.3-1.2)^2 + (2.0-1.2)^2}{3}} = 0.8\ mm \qquad (7.5)$$

The RMS of patient residual error standard deviations is:

$$\sigma = \sqrt{\frac{(1.7)^2 + (3.2)^2 + (1.0)^2 + (1.4)^2}{4}} = 2.0\ mm \qquad (7.6)$$

The resulting, required PTV margin for use with the prostate localization system is thus:

$$PTV = (2.5 \times 0.8) + (0.7 \times 2.0) = 3.4\ mm \qquad (7.7)$$

Smaller PTV margins ensure less healthy tissue is exposed to lethal doses of radiation.

Therefore, if this hypothetical margin is smaller than that necessary to use BAM, the prostate localization system in question would offer an improvement to prostate cancer treatments where BAM is currently used.

7.2 Results

Residual errors from 6 patients were used for this study. Table 7.3 summarizes the PTV margins required for each US or BAM patient repositioning protocol, described in section 7.1.1, in the AP, RL, and SI directions.

Table 7.3: PTV margins required if US or BAM were used routinely in one of four protocols: BAM_{All}, BAM_{NAL}, US_{All}, or US_{3mm}

	BAM_{All}	BAM_{NAL}	US_{All}	US_{3mm}
AP PTV Margin (mm)	9.9	10.8	14.0	13.8
RL PTV Margin (mm)	1.7	5.1	8.1	7.9
SI PTV Margin (mm)	12.9	15.1	7.8	7.4

In the AP and RL directions, BAM_{All} is the most effective protocol for realigning the prostate back into the planned treatment position. This is highlighted in the reduced size of the BAM_{All} PTV margins (9.9 mm in the AP direction and 1.7 mm in the RL direction) compared to the margins required by the other three protocols. BAM_{NAL} requires the second smallest PTV margins in these directions, making BAM the preferred image guidance technique for these orientations. US_{All} is the least valuable protocol in these directions, requiring considerably larger PTV margins.

In the SI direction, US_{3mm} requires the smallest PTV margin (7.4 mm), making it the most useful protocol for this orientation. US_{All} requires the second smallest PTV margin, making the Restitu System the preferred image guidance tool in the SI

direction. BAM_{NAL} is the least beneficial protocol, requiring the largest PTV margin for this orientation.

7.3 Discussion

By comparing the size of required PTV margins, BAM was shown to be the most useful image guidance technique in the AP and RL directions (PTV margins of 9.9 mm and 1.7 mm in AP and RL directions respectively for BAM_{All}), while the Restitu System was the most valuable tool in the SI direction (PTV margin of 7.4 mm for US_{3mm}).

Couch shifts employed for this analysis were derived from good quality US images only, eliminating the effects of US image quality on the agreement between US and FM measurements, and therefore, on the size of the PTV margins calculated. However, the reduced utility of the Restitu System in the AP and RL directions, as compared to BAM, may be due to the intra-user variability associated with manual segmentation US measurements. Section 6.3.2 showed intra-user variability was a moderate contributor to the lack of agreement associated with US and FM measurements in the AP direction, and a significant contributor in the RL direction. These findings are consistent with the lack of US utility observed in the AP and RL directions for this analysis. In addition, US intra-user variability had the least impact on agreement in the SI direction, which is consistent with the smaller PTV margins calculated for this orientation.

PTV margins for prostate cancer treatments typically range from 5 mm to 15 mm [49, 52, 55, 57, 58, 66–69]. Apart from the BAM_{All} margin in the RL direction (1.7 mm), margins calculated in this work fall approximately within the range of typical values. The RL BAM_{All} margin is smaller than expected due to low residual errors, or equivalently, a high level of agreement between FM and BAM shifts. This is likely due to a lack of prostate motion in this direction, making set-up error the

dominant cause of prostate displacement from the planned treatment position. Since BAM measures patient set-up errors, while FM prostate localization measures set-up errors and organ motion, lack of significant prostate motion would increase the agreement between BAM and FM measurements.

As US prostate localization using the Restitu System requires larger PTV margins in 2 out of 3 directions, it would not be worthwhile to replace BAM with this new device in clinics not using FMs.

Chapter 8

Conclusions

A new 3D US system for prostate IGRT, called the Restitu System, was compared to a standard IGRT technique that employs x-ray images of implanted FMs. The US system was introduced for prostate IGRT to avoid the invasive procedure required by the FM method, which poses a risk of infection, bleeding, and discomfort to patients. By comparing US images obtained at time of treatment planning, to those acquired each day of treatment delivery, couch shifts to realign the prostate into the treatment beam are determined by the US system with no associated risks. The Restitu system offers two methods for defining prostate position on US images: assisted and manual segmentation. Assisted segmentation allows contouring and locating the prostate with minimal user input, while manual segmentation offers the user complete control in placing the prostate contour on the US image.

The main goal of this thesis was to determine if the Restitu System could replace FMs, or be used interchangeably, for prostate IGRT. Couch shifts measured using assisted and manual segmentation US were compared to the corresponding shifts measured using FMs in each direction (AP, RL, SI), and LOA were calculated based on differences between US and FM measures (FM - US shifts). Ninety-five percent limits of agreement indicated that the Restitu system cannot safely replace FMs for daily prostate alignment, using assisted or manual segmentation, within the 3 mm

measure of equivalency. Use of manual prostate segmentation produced greater agreement with FM measured couch shifts than assisted segmentation, and was deemed the preferable mode of use for the US system.

An investigation into the sources of discrepancy between US and FM measured couch shifts followed. An F-test was used to compare the variability of US and FM couch shift distributions, and revealed a trend of increased variability in US recorded shifts compared to FM measures. This result promoted examination of two potential sources of US variability and their effects on agreement: US image quality and US user variability.

The effects of US image quality on the agreement between US and FM couch shift measurements were examined first. Ultrasound images were sorted into "high" and "low" quality groups based on the visibility of key anatomical structures, and the LOA were re-calculated for each group independently. For all directions and segmentation methods, couch shifts determined using high quality US images agreed more closely with FM shifts than those acquired using low quality US images, revealing low US image quality was a contributing factor to the lack of agreement observed. However, LOA for the high image quality groups still fell outside the 3 mm measure of equivalency in all cases, indicating low image quality was not the only source of discrepancy.

The effects of US user variability were examined next. Both intra- and inter-user variability were quantified by having multiple users make repeated couch shift measurements, for several US scans, using both assisted and manual segmentation. Repeatability coefficients were then calculated and compared to the LOA. This comparison revealed intra-user variability is a significant source of disagreement between US and FM measurements in the RL direction for both assisted and manual segmentation. Inter-user variability contributes more to the discrepancies observed than intra-user variability, and is a significant source of error in the AP and RL directions

for assisted segmentation US, and in the RL and SI directions for manual segmentation US.

The second goal of this work was to assess the clinical utility of the Restitu system by comparing it to BAM using PTV margins. Since healthy tissues are exposed to less lethal radiation when smaller PTV margins are employed, the size of a required margin relates the effectiveness of a given repositioning technique. PTV margins required to move patients using protocols based on US derived couch shifts were compared to those required to move patients using protocols based on BAM measured shifts. Only couch shifts derived from high quality US images, using manual segmentation, and their corresponding BAM shifts were used. Based on the PTV margins derived, BAM is the more effective method for measuring couch shifts to reposition patients in the AP and RL directions, but US is more useful in the SI direction. Since US prostate localization requires larger PTV margins in 2 out of 3 directions, the cost and labor associated with integrating a new IGRT system into regular clinical practice outweigh the benefits of replacing BAM with the Restitu System.

Thus, while US prostate localization offers patients a non-invasive procedure during IGRT, improvements to the accuracy and precision of the Restitu System must be made before this new device can be used routinely for prostate localization in clinical practice. System performance may improve by ensuring consistent acquisition of high quality US images and reducing US user variability through standardization of US system variables (noise rejection level, brightness, etc.) and additional operator training. Further user training may also improve system performance by reducing prostate displacements caused by operator applied transducer pressure.

Bibliography

[1] F. M. Khan. The Physics of Radiation Therapy. Lippincott Williams and Wilkins, Pennsylvania, 3rd edition, 2003.

[2] A. B. Wolbarst. Physics of Radiology. Medical Physics Publishing, Wisconsin, 2000.

[3] J. Van Dyk. The Modern Technology of Radiation Oncology. Medical Physics Publishing, Wisconsin, 1999.

[4] J. T. Bushberg, J. A. Seibert, E. M. Leidholdt Jr., and J. M. Boone. The Essential Physics of Medical Imaging. Lippincott Williams and Wilkins, Pennsylvania, 2nd edition, 2002.

[5] Canadian Cancer Society/National Cancer Institute of Canada. Canadian Cancer Statistics. Toronto, Canada, 2007.

[6] Canadian Cancer Society. Prostate Cancer: Understanding Your Diagnosis. 2007.

[7] M. Wallance and L. L. Powel, editors. Prostate Cancer Nursing Assessment, Management, and Care. Springer Series on Geriatric Nursing. Springer Publishing Company, New York, 2002.

[8] R. S. Kirby, A. W. Partin, M. Feneley, and J. K. Parsons, editors. Prostate Cancer Principles and Practice. Taylor and Francis, New York, 2006.

[9] J.M. Crook, Y. Raymond, D. Salhanib, H. Yangb, and B. Eschea. Prostate motion during standard radiotherapy as assessed by fiducial markers. Radiotherapy and Oncology, 37:35–42, 1995.

[10] J. C. Roeske, J. D. Forman, C. F. Mesina, T. He, C. A. Pelizzari, E. Fontenla, S. Vijayakumar, and G. T. Y. Chen. Evaluation of changes in the size and location of the prostate, seminal vesicles, bladder, and rectum during a course of external beam radiation therapy. International Journal Of Radiation Oncology, Biology, Physics, 33:1321–1329, 1995.

[11] M. Van Herk, A. Bruce, A. P. G. Kroes, T. Shouman, A. Touw, and J. V. Lebesque. Quantification of organ motion during conformal radiotherapy of the prostate by three dimensional image registration. International Journal Of Radiation Oncology, Biology, Physics, 33:1311–1320, 1995.

[12] U. A. van der Heide, A. N. T. J. Kotte, H. Dehnad, P. Hofman, J. J. W. Lagenijk, and M. van Vulpen. Analysis of fiducial marker-based position verification in the external beam radiotherapy of patients with prostate cancer. Radiotherapy and Oncology, 82:38–45, 2007.

[13] J. M. Schallenkamp, M. G. Herman, J. J. Kruse, and T. M. Pisansky. Prostate position relative to pelvic bony anatomy based on intraprostatic gold markers and electronic portal imaging. International Journal Of Radiation Oncology, Biology, Physics, 63:800–811, 2005.

[14] P. A. Kupelian, T. R. Willoughby, S. L. Meeks, A. Forbes, T. Wagner, M. Maach, and K. M. Langen. Intraprostatic fiducials for localization of the prostate gland: Monitoring intermarker distances during radiation therapy to test for marker stability. International Journal Of Radiation Oncology, Biology, Physics, 62:1291–1296, 2005.

[15] M. G. Herman, T. M. Pisansky, J. J. Kruse, J. I. Prisciandaro, B. J. Davis, and B. F. King. Technical aspects of daily online positioning of the prostate for three-dimensional conformal radiotherapy using an electronic portal imaging device. International Journal Of Radiation Oncology, Biology, Physics, 57:1131–1140, 2003.

[16] H. Dehnad, A. J. Nederveen, U. A. van der Heide, R. J. A. van Moorselaar, P. Hofman, and J. J. W. Lagendijk. Clinical feasibility study for the use of implanted gold seeds in the prostate as reliable positioning markers during megavoltage irradiation. Radiotherapy and Oncology, 67:295–302, 2003.

[17] J. Pouliot, M. Aubin, K. M. Langen, Y. Liu, B. Pickett, K. Shinohara, and M. Roach III. (Non) - migration of radiopaque markers used for on-line localization of the prostate with an electronic portal imaging device. International Journal Of Radiation Oncology, Biology, Physics, 56:862–866, 2003.

[18] H. Shirato, T. Harada, T. Harabayashi, K. Hida, H. Endo, K. Kitamura, R. Onimaru, K. Yamazaki, N. Kurauchi, T. Shimizu, N. Shinohara, M. Matsushita, H. Dosaka-Akita, and K. Miyasaka. Feasibility of insertion/implantation of 2.0-mm-diameter gold internal fiducial markers for precise setup and real-time tumor tracking in radiotherapy. International Journal Of Radiation Oncology, Biology, Physics, 56:240–247, 2003.

[19] F. L. B. Cury, G. Shenouda, L. Souhami, M. Duclos, S. L. Faria, M. David, F. Verhaegen, R. Corns, and T. Falco. Ultrasound-based image guided radiotherapy for prostate cancercomparison of cross-modality and intramodality methods for daily localization during external beam radiotherapy. International Journal Of Radiation Oncology, Biology, Physics, 66:1562–1567, 2006.

[20] G. E. Hanks, A. L. Hanlon, T. E. Schultheiss, W. H. Pinover, B. Movsas, B. E.

Epstein, and M. A. Hunt. Dose escalation with 3d conformal treatment: Five year outcomes, treatment optimization, and future directions. International Journal Of Radiation Oncology, Biology, Physics, 41:501–510, 1998.

[21] M. J. Zelefsky, S. A. Leibel, P. B. Gaudin, G. J. Kutcher, N. E. Fleshner, E. S. Venkatramen, V. E. Reuter, W. R. Fair, C. C. Ling, and Z. Fuks. Dose escalation with three-dimensional conformal radiation therapy affects the outcome in prostate cancer. International Journal Of Radiation Oncology, Biology, Physics, 41:491–500, 1998.

[22] International Commission on Radiation Units and Measurements (ICRU). Prescribing, recording, and reporting photon beam therapy. Technical report, Maryland, 1993.

[23] P. Metcalfe, T. Kron, and P. Hoban. The Physics of Radiotherapy X-rays from Linear Accelerators. Medical Physics Publishing, Wisconsin, 1997.

[24] K. M. Langen and D. T. L. Jones. Organ motion and its management. International Journal Of Radiation Oncology, Biology, Physics, 50:265–278, 2001.

[25] C. M. Rumack, S. R. Wilson, J. W. Charboneau, and J. M. Johnson, editors. Diagnostic Ultrasound, volume 1. Elsevier Mosby, Missouri, 3rd edition, 2005.

[26] Y Kim and S. C. Horii, editors. Handbook of Medical Imaging, volume 3. SPIE - The International Society of Optical Engineering, Washington, 2000.

[27] D. A. Christensen. Ultrasonic Bioinstrumentation. John Wiley and Sons,, New York,, 1988.

[28] D. B. Downey, A. Fenster, and J. C. Williams. Clinical utility of three-dimensional us. Radiographics, 20:559–571, 2000.

[29] T. R. Nelson and D. H. Pretorius. Three-dimensional ultrasound imaging. Ultrasound in Medicine and Biology, 24:1243–1270, 1998.

[30] A. Fenster, D. B. Downey, and H. N. Cardinal. Three-dimensional ultrasound imaging. Physics in Medicine and Biology, 46:R67–R99, 2001.

[31] M. M. Poggi, D. A. Gant, W. Sewchand, and W. B. Warlick. Marker seed migration in prostate localization. International Journal Of Radiation Oncology, Biology, Physics, 56:12481251, 2003.

[32] Resonant Medical Incorporated. Restitu Platform User Guide. Montreal, 2005.

[33] N. Hu, D. B. Downey, A. Fenster, and H. M. Ladak. Prostate boundary segmentation from 3d ultrasound images. Medical Physics, 30:1648–1659, 2003.

[34] H. M. Ladak, F. Mao, Y. Wang, D. B. Downey, D. A. Steinman, and A. Fenster. Prostate boundary segmentation from 2d ultrasound images. Medical Physics, 27:1777–1788, 2000.

[35] J. L. Devore. Probability and Statistics for Engineering and the Sciences. Duxbury, California, 5th edition, 2000.

[36] M. Bland. An Introduction to Medical Statistics. Oxford University Press, New York, 3rd edition, 2000.

[37] L. Lyons. Statistics for Nuclear and Particle Physicists. Cambridge University Press, New York, 1986.

[38] J. M. Bland and D. G. Altman. Statistical methods for assessing agreement between two methods of clinical measurement. Lancet, 1:307–310, 1986.

[39] J. M. Bland and D. G. Altman. Measuring agreement in method comparison studies. Statistical Methods in Medical Research, 8:135–160, 1999.

[40] J. M. Bland and D. G. Altman. Applying the right statistics: Analyses of measurement studies. Ultrasound in Obstetrics & Gynecology, 22:85–93, 2003.

[41] S. Dowdy, S. Wearden, and D. Chilko. Statistics for Research. John Wiley and Sons, Inc., New Jersey, 3rd edition, 2004.

[42] J. M. Bland. How do I analyse observer variation studies? Unpublished, 2004.

[43] M. Hilts, T. Bull, K. Patterson, V. Small, L. Drever, and E. Berthelet. Reproducibility of prostate misalignments computed by automatic segmentation of abdominal ultrasound images used for image guided radiation therapy. International Federation for Medical and Biological Engineering Proceedings, 14:1712–1715, 2006.

[44] L. Drever and M. Hilts. Daily quality assurance phantom for ultrasound image guided radiation therapy. Journal of Applied Clinical Medical Physics, 8:126–136, 2007.

[45] J. P. McGahan, J. Ryu, and M. Fogata. Ultrasound probe pressure as a source of error in prostate localization for external beam radiotherapy. International Journal Of Radiation Oncology, Biology, Physics, 60:788–793, 2004.

[46] X. Artignan, M. H. P. Smitsmans, J. V. Lebesque, D. A. Jaffray, M. Van Herk, and H. Bartelink. Online ultrasound image guidance for radiotherapy of prostate cancer: Impact of image acquisition on prostate displacement. International Journal Of Radiation Oncology, Biology, Physics, 59:595–601, 2004.

[47] C. F. Serago, S. J. Chungbin, S. J. Buskirk, G. A. Ezzell, A. C. Collie, and S. A. Vora. Initial experience with ultrasound localization for positioning prostate cancer patients for external beam radiotherapy. International Journal Of Radiation Oncology, Biology, Physics, 53:1130–1138, 2002.

[48] T. J. Scarbrough, N. M. Golden, J. Y. Ting, C. D. Fuller, A. Wong, P. A. Kupelian, and C. R. Thomas Jr. Comparison of ultrasound and implanted seed marker prostate localization methods: Implications for imageguided radiotherapy. International Journal Of Radiation Oncology, Biology, Physics, 65:378–387, 2006.

[49] J. Morr, T. Dipetrillo, J-S. Tsai, M. Engler, and D. E. Wazer. Implementation and utility of a daily ultrasound-based localization system with intensity-modulated radiotherapy for prostate cancer. International Journal Of Radiation Oncology, Biology, Physics, 53:1124–1129, 2002.

[50] A. Chandra, L. Dong, E. Huang, D. A. Kuban, L. ONeill, I. Rosen, and A. Pollack. Experience of ultrasound-based daily prostate localization. International Journal Of Radiation Oncology, Biology, Physics, 56:436–447, 2003.

[51] T.M. Powell, F. Van den Heuvel, M. Kahn, and J.D. Forman. Independent prostate motion as measured by daily BAT ultrasound and electronic portal imaging [abstract]. International Journal Of Radiation Oncology, Biology, Physics (Suppl. 1), 51:215, 2001.

[52] D. J. Little, L. Dong, L. B. Levy, A. Chandra, and D. A. Kuban. Use of portal images and bat ultrasonography to measure setup error and organ motion for prostate IMRT: Implications for treatment margins. International Journal Of Radiation Oncology, Biology, Physics, 56:1218–1224, 2003.

[53] F. Trichter and R. D. Ennis. Prostate localization using transabdominal ultrasound imaging. International Journal Of Radiation Oncology, Biology, Physics, 56:1225–1233, 2003.

[54] A. Y. C. Fung, K. M. Ayyangar, D. Djajaputra, R. M. Nehru, and C. A. Enke.

Ultrasound-based guidance of intensity-modulated radiation therapy. Medical Dosimetry, 31:20–29, 2006.

[55] J. Lattanzi, S. Mcneeley, W. Pinover, E. Horwitz, I. Das, T. E. Schultheiss, and G. E. Hanks. A comparison of daily ct localization to a daily ultrasound-based system in prostate cancer. International Journal Of Radiation Oncology, Biology, Physics, 43:719–725, 1999.

[56] J. Lattanzi, S. Mcneeley, A. Hanlon, T. E. Schultheiss, and G. E. Hanks. Ultrasound-based stereotactic guidance of precision conformal external beam radiation therapy in clinically localized prostate cancer. Adult Urology, 55:73–78, 2000.

[57] J. Lattanzi, S. McNeeley, S. Donnelly, E. Palacio, A. Hanlon, T. E. Schultheiss, and G. E. Hanks. Ultrasound-based stereotactic guidance in prostate cancerquantification of organ motion and set-up errors in external beam radiation therapy. Computer Aided Surgery, 5:289–295, 2000.

[58] C. F. Serago, S. J. Buskirk, T. C. Igel, A. A. Gale, N. E. Serago, and J. D. Earle. Comparison of daily megavoltage electronic portal imaging or kilovoltage imaging with marker seeds to ultrasound imaging or skin marks for prostate localization and treatment positioning in patients with prostate cancer. International Journal Of Radiation Oncology, Biology, Physics, 65:1585–1592, 2006.

[59] K. M. Langen, J. Pouliot, C. Anezinos, M. Aubin, A. R. Gottschalk, I-C. Hsu, D. Lowther, Y-M. Liu, K. Shinohara, L. J. Verhey, V. Weinberg, and M. Roach III. Evaluation of ultrasound-based prostate localization for image-guided radiotherapy. International Journal Of Radiation Oncology, Biology, Physics, 57:635–644, 2003.

[60] H. A. Mcnair, S. A. Mangar, J. Coffey, B. Shoulders, V. N. Hansen, A. Norman,

J. Staffurth, S. A. Sohaib, A. P. Warrington, and D. P. Dearnaley. A comparison of CT- and ultrasound-based imaging to localize the prostate for external beam radiotherapy. International Journal Of Radiation Oncology, Biology, Physics, 65:678–687, 2006.

[61] C. D. Fuller1, C. R. Thomas Jr., S. Schwartz, N. Golden, J. Ting, A. Wong, D. Erdogmus, and T. J. Scarbrough. Method comparison of ultrasound and kilovoltage x-ray fiducial marker imaging for prostate radiotherapy targeting. Physics In Medicine and Biology, 51:4981–4993, 2006.

[62] R. Tirona, G. Morton, M. Pearse, K. Sixel, and P. O'Brien. Interfraction motion measured using 3D ultrasound and gold seed localization. Radiotherapy and Oncology, 80:S48, 2006.

[63] H. C. J. De Boer and B. J. M. Heijmen. A protocol for the reduction of systematic patient setup errors with minimal portal imaging workload. International Journal Of Radiation Oncology, Biology, Physics, 50:1350–1365, 2001.

[64] M. Van Herk, P. Remeijer, C. Rasch, and J. V. Lebesque. The probability of correct target dosage: dose-population histograms for deriving treatment margins in radiotherapy. International Journal Of Radiation Oncology, Biology, Physics, 47:1121–1135, 2000.

[65] M. Van Herk. Errors and margins in radiotherapy. Seminars in Radiation Oncology, 14:52–64, 2004.

[66] M. Ghilezan, D. Yan, J. Liang, D. Jaffray, J. Wong, and A. Martinez. Online image-guided intensity-modulated radiotherapy for prostate cancer: how much improvement can we expect? a theoretical assessment of clinical benefits and potential dose escalation by improving precision and accuracy of radiation delivery.

International Journal Of Radiation Oncology, Biology, Physics, 60:1602–1610, 2004.

[67] H. Alasti, M. P. Petric, C. N. Catton, and P. R. Warde. Portal imaging for evaluation of daily on-line setup errors and off-line organ motion during conformal irradiation of carcinoma of the prostate. International Journal Of Radiation Oncology, Biology, Physics, 49:869–884, 2001.

[68] A. Tinger, J. M. Michalski, A. Cheng, D. A. Low, R. Zhu, W. R. Bosch, J. A. Purdy, and C. A. Perez. A critical evaluation of the planning target volume for 3-d conformal radiotherapy of prostate cancer. International Journal Of Radiation Oncology, Biology, Physics, 42:213–221, 1998.

[69] F. Van den Heuvel, T. Powell, E. Seppi, P. Littrupp, M. Khan, Y. Wang, and J. D. Forman. Independent verification of ultrasound based image-guided radiation treatment, using electronic portal imaging and implanted gold markers. Medical Physics, 30:2878–2887, 2003.